INVESTIGATION OF REACTION BONDING OF A LITHIUM SOLID ELECTROLYTE AND ITS APPLICATION TO LITHIUM-ALUMINUM ALLOYS

By JIAN WU B.Eng

A thesis

Submitted to the School of Graduate Studies

in Partial Fulfillment of the Requirements

for the Degree

Master of Science

McMaster University

April 2002

MASTER OF SCIENCE (2002) McMaster University

(Materials Science and Engineering) Hamilton, Ontario

TITLE: Investigation of Reaction Bonding of a Lithium Solid Electrolyte and Its Application to Lithium-Aluminum Alloys

AUTHOR: Jian Wu, B. Eng. (Northeastern University, China)
Senior Engineer (Shenzhen Polytechnic, China)

SUPERVISOR: Professor Anthony Petric

NUMBER OF PAGES: xx, 117

ABSTRACT

The goals of this study were to unravel the mechanism of the liquid phase joining reaction between the $LiYO_2$ electrolyte and the Y_2O_3-MgO lid used in the fabrication of an EMF cell and second, to investigate the Li-Al binary alloy system by the EMF method.

The joining occurs between the electrolyte tube and the inert lid when they are rapidly heated to 1325°C. It was found that the tube and the lid were joined by reaction bonding in which Li_2CO_3 served a key role as the bonding agent and a sintering additive. When sufficient liquid phase fraction is present, the melt at the base of the tube reacts with the Y_2O_3 lid and forms a solid $LiYO_2$ joint. This triggers a rapid densification process that propagates upward to the top of the tube. XRD, DTA and SEM were used to analyze the properties of $LiYO_2$ and the microstructure of the tube and the joint.

The cell fabricated in this way worked steadily for several months in contact with liquid lithium or lithium alloy. The thermodynamic properties of Li-Al alloys, including the liquid phase, the α-solution region, and the $\alpha + \beta$ two-phase region were investigated in the temperature range of 370 to 750°C. The liquidus curve could be directly obtained from the EMF versus temperature plot.

The solid-liquid phase boundary was consistent with data from the literature. The ΔG, ΔS and ΔH of the molten alloys up to 30% Li were derived from the measurements.

The cell elaborated in this study can be used not only for phase diagram analysis, but also as a sensor for Li in molten alloys or possibly in high temperature batteries.

ACKNOWLEDGMENTS

I wish to acknowledge particularly the supervision and positive guidance and support by Dr. Anthony Petric. I am grateful for the opportunity of this education.

I would also like to thank Luis Yamarte from whose previous work I benefited, as well as Taras Kolodiazhnyi and Georgios Tsintzilonis for their advice and help.

The technical assistance of Guanglei Liu, Jim Garrett, Connie Barry, Chris Butcher, Martin Van Oosten, Ed McCaffery is gratefully acknowledged.

I would like to thank my friends, Da Xu, Joshua Deng, Honglu Yu and Don Braggs, who helped not only my study but also with other things in life.

Finally, I thank my family for encouraging me along the way.

CONTENT

LIST OF TABLES

LIST OF FIGURES

Chapter 1. INTRODUCTION

Aluminum-lithium alloys have been developed as structural materials for applications in the aerospace and transportation. They are lighter and stiffer than conventional aluminium alloys. In order to define the processing conditions for these alloys and subsequent treatments to obtain specific engineering properties, a knowledge of the phase diagram and thermodynamic properties of these alloys is essential.

Thermodynamic data of Li-Al alloys are still incomplete. Although phase equilibria of the Li-Al binary were studied by many investigators as summarized in the review by Chen et al. [Che89], the data reported in the literature is not in agreement. In view of the intrinsic experimental difficulties in working with these alloys, such as vaporization and oxidation of Li, and interaction of either Li or Al with the container materials, it is not surprising that these discrepancies exist in the literature.

An attractive feature of the Al-Li alloy system is the large solid solubility of Li in Al (~14 at. %) at 600°C. Alloys can be heat treated in this range to homogenize the α (Al_3Li) phase, then quenched to form the metastable α' phase as coherent precipitates. The α' precipitates are the major strengthening mechanism of Al-Li alloys [Flo87].

The disadvantage of lithium as an alloying agent is its high reactivity, not only with oxygen, but also with nitrogen, carbon dioxide and water. Thus another objective of this study is to obtain precise data on the chemical potentials of lithium in aluminum alloys which are needed to predict long term environmental effects.

In industry, the addition of lithium to molten aluminum is done by means of Li master alloys because of the high reactivity of lithium. Knowledge of the chemical properties of the master alloys would allow their utilisation in the most efficient manner. Such information would also be useful in optimizing the recovery of Li during recycling of Al- Li scrap.

Studies of lithium or other reactive metals are prone to error for three major reasons. First, they tend to oxidize rapidly, resulting in a change from the original composition. Second, they tend to evaporate quickly, again causing a drift from the expected composition. Third, it is very difficult to find compatible materials for the experimental apparatus which are stable against liquid lithium.

The objective of this thesis is two-fold: first to investigate the mechanism of joining the $LiYO_2$ electrolyte tube to the lid composed of Y_2O_3-12%MgO, and second, to measure the thermodynamic properties of Li-Al system.

An examination of the literature [Chapter 2] shows there have been several methods used to measure the Li-Al system. The methods employed include resistivity and microhardness measurements [Cos62], X-ray and quantitative optical metallography [Lev63], electrochemical [Wen80], transmission electron microscopy [Wen80], low-angle X-ray scattering [Cer77], differential thermal analysis (DTA), metallography, chemical analysis [Che89], and differential scanning calorimetry [Wil89]. Often one of the thermodynamic properties is measured independently, for example, enthalpy by calorimetry, or phase boundaries by differential thermal analysis.

Only the electrochemical method (the emf technique) can be used to determine all the thermodynamic properties which are necessarily interdependent. All measurements are taken at equilibrium so that there is no need for compensation of long reaction times or undercooling effects which may present problems in calorimetry or DTA. Phase diagram invariant temperatures are determined with great precision (±1°C), limited only by the accuracy of the thermocouple and purity of the alloy. Thus one can obtain a consistent set of thermodynamic data for the complete binary system.

In chapter 2, previous research on Li ionic conductors, the technique for evaluating thermodynamic properties, selection of insulating materials and earlier research in this lab are reviewed.

Chapter 3 provides details of the experimental method, which includes fabrication of the measurement apparatus, the emf measurement technique and the data acquisition system.

Chapter 4 reports and discusses the results of both the ceramic study and thermodynamic properties of Li-Al binary alloys. The mechanism of joining and sintering the $LiYO_2$ tube and the role of Li_2CO_3 in joining and sintering are described in detail.

Chapter 2. LITERATURE REVIEW

2.1. Thermodynamic Properties of Lithium Aluminum Alloys

The earliest phase diagram of the lithium-aluminum system was published by Muller in 1926 [Mul26]. Although phase equilibria of the Al-Li binary were studied by many investigators [Yat74, Smi76, Ell81, Mca82, Kha88, Che89], there is still disagreement in the literature. The most important argument focused on so-called metastable α' (or δ') phase for the following reasons: (i) this phase forms coherent precipitates and is responsible for the significant strengthening of Al-Li alloys [Flo87], (ii) it is difficult to determine clear and consistent data for this phase boundary.

2.1.1. The Phase Diagram of Li-Al

The following boundaries and invariant points of the Li-Al phase diagram have been established with reasonable certainty (Figure 2-1):

the aluminum-rich eutectic temperature, 600±5°C;

the $\beta+L \rightarrow \gamma$ peritectic, 520±5°C, 60 at.% Li;

the $L \rightarrow \delta$ + bcc eutectic, 177±3°C, 97.8 at.% Li;

the $\alpha/(\alpha+\beta)$ and $(\alpha+\beta)/\beta$ boundaries from 400°C to 600°C.

Other features of the diagram are qualitatively correct, but significant questions remain in the $\alpha+\beta$ region. These include the occurrence of the metastable α' phase in the

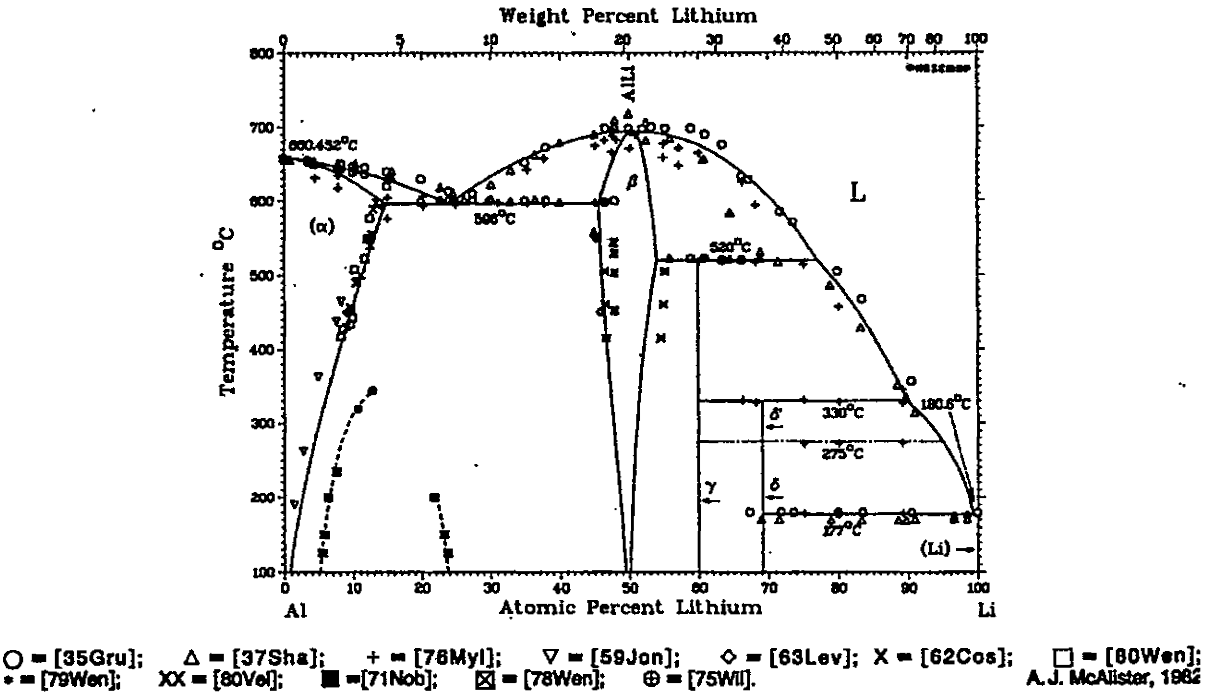

Figure 2-1. The Li-Al phase diagram with the data points from the literature [Mca82]

equilibrium (α+β) field and the α-Al + β-AlLi eutectic composition which is reported to vary from 23.4 to 30.8 at.% Li [Wil89].

2.1.2. Solid Solubilities

Many studies, both experimental and theoretical, have been carried out at low temperatures (<300°C) to determine the regime over which the metastable Al_3Li phase exists. Two determinations of the solvus, by Costas and Marshall (resistivity and microhardness) [Cos62] and Levine and Rappeport (X-ray and quantitative optical metallography) [Lev63], gave high Li saturation concentrations below 400°C. Above 400°C, these data, and those of Wen and Huggins et al. (electrochemical) [Wen80], are in quite good agreement.

The β phase extends from about 45 at.% Li at 600°C to about 55 at.% Li at 500°C. The γ phase was reported by Wen [Wen79] to extend from 60.3 to 61.7 at.% Li at 433°C. That it is the γ and not the δ (or δ') phase which melts peritectically at 520°C is confirmed both by the thermal arrest measurements of Myles et al. [Myl76] and the electrochemical measurements of Wen et al. [Wen79] at 423°C over the composition range 10 to 70 at.% Li. In the latter work, the γ phase was observed; the δ phase was not.

2.1.3. Liquidus and Solidus

Liquidus and solidus measurements were carried out by thermal analysis [Mul26, Gru35, Sha37 and Myl76]. The reaction temperatures are in reasonable agreement as mentioned in section 2.1.1. The β phase melts congruently near 700±5°C, and 50 at.% Li. Myles et al. [Myl76] reported the γ+L→ δ' peritectic occurs at 335°C and δ→δ' transformation at 275°C. Shamray et al. [Sha37] reported liquidus and solidus studies at Li concentrations in excess of 90 at.%, and their data suggest that the L→ δ + bcc eutectic point falls at 97 at.% Li.

There are two main areas of disagreement. Although all the above studies are in essential agreement on the L→ α+β eutectic temperature, there is inconsistency with regard to the Li concentration at the eutectic point, and the α and the β termini of the eutectic line. Moreover, the α solidus and α solvus lines have not been unambiguously defined [Mca82].

For example, the α+L boundary data of Myles [Myl76] lie well below these of Grube [Gru35] and Shamray [Sha37]. The emf measurements of this thesis will help to clarify these uncertainties.

2.1.4. Measured Activities in Al-Li Alloys

Liquid: the Knudsen method was used by Hicter et al. [Hic71] at 684°C and 714°C, and the electrochemical method by Yatsenko and Saltykova [Yat74] at 750°C. These data are in good agreement and indicate subregular behavior in the liquid [Che89].

α-phase: The electrochemical method was applied by Wen et al. [Wen80] to measure activities in the solid at 0 to 9.1 at.% Li at 423°C, and from 0.7 to 5.7 at.% Li at 300°C to 600°C. As in the liquid, subregular behavior was observed (Figure 2-2).

β-phase: Electrochemical measurements were made by Yao et al. [Yao71] and Wen et al. [Wen79]; hydrogen titration measurements were made by Veleckies [Vel80]. Wen et al. are the only investigators to determine Li activities as a function of composition within the homogeneity range of this phase. These results are shown in Figure 2-2.

γ-phase: A small range of solubility was observed by Wen et al. [Wen79], 60.1 to 61.7 at.% Li, with approximately linear variation of the Li activity in this range.

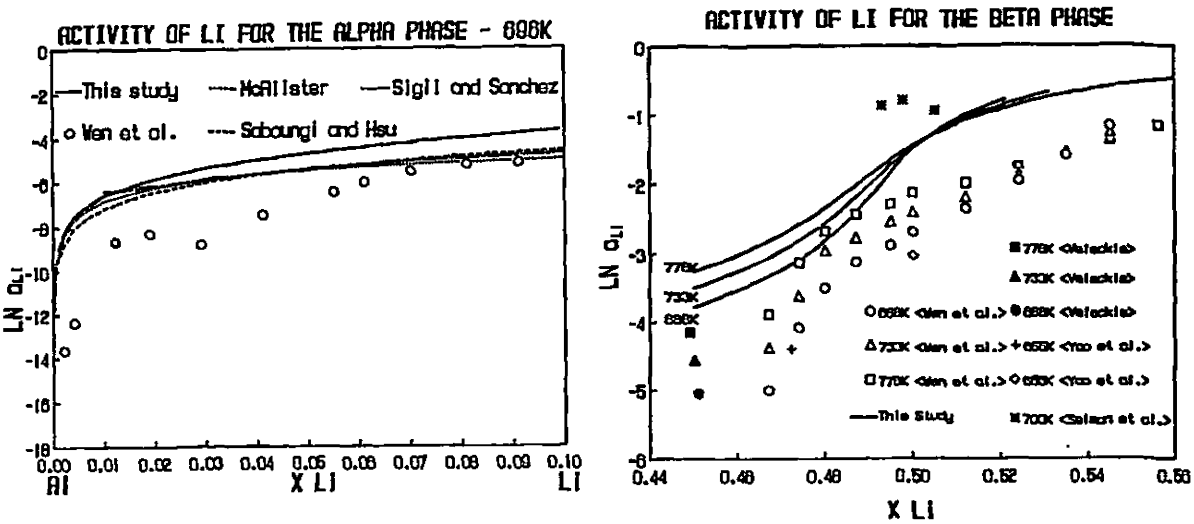

Figure 2-2. Comparison of activity of Li in Al for α (left) and β (right) phase in the literature [Che89]

2.2. Techniques for Evaluating Thermodynamic Properties

2.2.1. Calorimetry

The first of the thermodynamic functions to be determined experimentally for a large number of substances was the heat of formation [Kub67]. This is usually determined by the calorimetric method, which is quite simple in principle. The reaction to be investigated is carried out in an apparatus of known heat capacity, the calorimeter, so that the heat capacity is measured by the change in temperature during reaction.

In calorimetry, if measurements and chemical analyses are carried out meticulously, the final result can be given with an estimated error, which can be relied upon. The quantities obtained directly from equilibrium measurements are the enthalpies from which heat capacity can be calculated only when the temperature coefficients of the free energies are known, the advantage being that they then provide not only the heat but also the entropy of reaction. The reliability of heat and entropy values obtained in this way is, however, usually overestimated. Relatively small errors in the free energies may result in large errors in the temperature coefficients. Equilibria involving solids are particularly difficult to measure accurately.

2.2.2. EMF Technique

The EMF technique is ideal for the measurement of not only thermodynamic properties but also the phase diagram. Whenever a phase boundary is crossed (either by varying T at constant X or varying X at constant T), whether solid-solid, solid-liquid or liquid-liquid, there is a discontinuity in the slope of the EMF versus temperature or EMF versus composition. Thus by taking numerous measurements in the vicinity of a phase boundary; one obtains a locus of invariant points, which give a relation between EMF and temperature. If the activity-composition relationship is known, a typical phase diagram of temperature versus composition can be constructed. The advantage of the EMF method is that all points are obtained at complete chemical and thermal equilibrium and are free from kinetic effects such as are found in thermal analysis measurements. The EMF measurement requires a reversible cell to be set up and high temperature EMF measurements depend upon the availability of a suitable electrolyte. If an electrolyte is selective to one ionic species and "opaque" to all others, the chemical potential of that species can be measured and related and to other thermochemical properties. In order to obtain a stable potential, an electrolyte must have a minimum conductivity of about 10^{-6} S/cm [Sch72]. As a rule, the ionic transport number must be greater than 0.99 if the electrolyte is to be practical for EMF measurements.

A galvanic cell for measuring the activity of Li in solution can be written schematically as:

$$pure\ \ Li, a_{Li}(1)\,|\,Li\ \ solid\ \ electrolyte\,|\,Li\ \ alloy, a_{Li}(2) \qquad \textbf{Cell 1}$$

The EMF is related to the activities by:

$$E = -\frac{RT}{F}\ln\frac{a_{Li}(2)}{a_{Li}(1)} \qquad \textbf{Eq. 2-1}$$

Since the activity of pure Li is equal to 1, or a known reference material is used to fix the activity on one side of the equation, the activity on the other side can be calculated from the measured emf of the cell. The results can be used to determine the Gibbs energies of mixing of solutions and the Gibbs energies of formation of compounds.

If the activity-composition relationship has been established for a solution, a solid electrolyte probe can be used to monitor directly the composition of a system. That is what we call a sensor.

2.2.3. Thermodynamic Properties

The thermodynamic properties can be readily derived from EMF measurements. The chemical and electrical potential are related by:

$$\mu_i - \mu_i^o = FE \qquad \textbf{Eq. 2-2}$$

where μ_i^o and μ_i are the chemical potentials of the pure and working electrodes respectively, The partial Gibbs energy in terms of the activity or activity coefficient of the first component is given by:

$$-FE = \Delta G_1 = RT\ln a_1 = RT\ln\gamma_1 + RT\ln X_1 \qquad \textbf{Eq. 2-3}$$

where R=8.314 J/mol-K, T is in Kelvin and X_1 is the atom fraction of component 1. One can see that the partial Gibbs energy, the activity and activity coefficient follow directly from the measured EMF. To obtain the properties of the second component in a two component system, one uses the Gibbs-Duhem or Duhem-Margules equation:

$$X_1 d\ln\gamma_1 + X_2 d\ln\gamma_2 = 0 \qquad \textbf{Eq.2-4}$$

By rearranging the terms and integrating, we arrive at the value of the second component:

$$\ln\gamma_2 = -\frac{X_1}{X_2}\int_0^{x_1} d\ln\gamma_1 \qquad \textbf{Eq. 2-5}$$

The integral Gibbs energy is calculated by :

$$\Delta G = RT(X_1\ln a_1 + X_2\ln a_2) \qquad \textbf{Eq. 2-6}$$

or

$$\Delta G = X_1\Delta G_1 + X_2\Delta G_2 \qquad \textbf{Eq. 2-7}$$

The partial excess Gibbs energy is defined as :

$$G_1^E = RT\ln\gamma_1 \qquad \textbf{Eq. 2-8}$$

and the integral quantity is derived as above.

The partial entropy and enthalpy can both be obtained from the temperature dependence of the EMF:

$$\Delta S_1 = -\frac{\partial \Delta G_1}{\partial T} = F\frac{\partial E}{\partial T} \qquad \textbf{Eq. 2-9}$$

$$\Delta H_1 = \frac{\partial(\Delta G_1 / T)}{\partial(1/T)} = -F\frac{\partial(E/T)}{\partial(1/T)} \qquad \textbf{Eq. 2-10}$$

In practice, only ΔS is derived from the temperature dependence and ΔH is obtained from the Gibbs-Hemholtz equation:

$$\Delta G_i = \Delta H_i - T\Delta S_i \qquad \textbf{Eq. 2-11}$$

To measure temperature dependence, EMF readings are taken at various temperatures and fixed composition. The points are fitted to a polynomial equation which, when differentiated with respect to T, yields the partial entropy. The Gibbs-Duhem equation can again be used to obtain the partial entropy of the second component. The preferred method is to substitute S_1^E for $\ln \gamma_1$ in Eq. 2-11, where S_1^E is the partial excess entropy defined as :

$$S_1^E = \Delta S_1 + R\ln X_1 \qquad \textbf{Eq. 2-12}$$

The integral properties can be obtained from Eq. 2-4. With sufficiently accurate data, the partial heat capacity can be derived as the second derivative of the temperature dependence:

$$C_{P(1)}^E = -T\frac{\partial^2 \Delta G_1}{\partial T^2} = -FT\frac{\partial^2 E}{\partial T^2} \qquad \textbf{Eq. 2-13}$$

The integral values can be calculated with Eq. 2-4 and Eq. 2-6. The heat capacity is designated as an excess quantity because, unlike ΔG, ΔH and ΔS which are assumed to be 0 for the pure components, C_p has a non-zero value at the end points. It must be realized that considerable allowance should be made for error in calculating the C_p^E since it is obtained from second derivative of the Gibbs energy.

2.3. Principles of Ionic Conduction

Interest in solid electrolytes for use in solid state batteries has been intense during the last thirty years [Tak66, Wes89, Iry89, and Ada96]. Lithium-based systems are particularly attractive due to their high energy densities and high open circuit potentials. There has been much work published on the characterization of lithium ion conducting materials at lower temperatures (up to 300°C). However, little research has focused on their behavior in the 400~600°C range, which is important for high temperature batteries designed for military applications [Att90, Hen94, Rit96].

2.3.1. Mechanisms of Ionic Conductivity and Application of Solid State Electrolytes

Generally speaking, solid state electrolytes, which conduct electricity by the motion of ions and exhibit negligible electronic transport, include crystalline and amorphous inorganic solids as well as ionically conducting polymers. Two broad classes of conduction mechanism, vacancy and interstitial migration, may be distinguished.

In vacancy migration, a number of sites that would be occupied in the ideal, defect-free structure are in fact, empty perhaps due to either Schottky defects (a cation and anion vacancy pair) or the presence of charged impurities. An ion adjacent to a vacancy may be able to hop into it leaving its own site vacant. This process is regarded as vacancy migration, although it is the ions that hop.

Interstitial sites are defined as those that would usually be empty in an ideal structure. Occasionally in real structures, ions may be displaced from their lattice sites into interstitial sites (Frenkel defect formation). Once this happens, the ions in interstitial sites can often hop into adjacent interstitial sites. These hops may be one stage of a long range conduction process.

This notion of occasional ion hops, apparently at random, forms the basis of random walk theory which is widely used to provide a semi-quantitative analysis or description of ionic conductivity. There is very little evidence in most solid electrolytes that the ions are instead able to move around without thermal activation in a true liquid-like motion. Nor is there much evidence of a free-ion state in which a particular ion can be activated to a state in which it is completely free to move, i.e. there appears to be no ionic equivalent of free or nearly free electron motion. A simple yet valuable starting point for treating ionic conductivity, σ_i, is as the product of the concentration, c_i, of mobile species (interstitial ions or vacancies), their charge, q and their mobility, u_i:

$$\sigma_i = c_i q u_i \qquad \textbf{Eq. 2-14}$$

This same equation is, of course, also used to rationalize the general electronic behavior of metals, semiconductors and insulators.

An important practical way of increasing the value of c_i is by means of doping with aliovalent (or heterovalent) ions. This involves partial replacement of ions of one type by ions of different formal charge. In order to retain charge balance, either interstitial ions or vacancies must be generated at the same time. If the interstitials or vacancies are able to migrate, dramatic increases in conductivity can result.

2.3.2. Immobile Ion Sublattice and Doping Effect

The solid electrolyte provides an essentially rigid framework with channels along which one of the ionic species of the solid can migrate. Whereas all ionic solids conduct, only those with very specific structural features are capable of exhibiting conductivity with potential commercial applications.

In crystalline electrolytes, conduction pathways for the mobile ions permeate the 'immobile ion sublattice' in one, two or three dimensions. For example, Na^+ ions in β-alumina can migrate only in two dimensions (Figure 2-3). The sites containing the mobile ions are not fully occupied and are connected, via open windows or bottlenecks, to adjacent sites that are also partially occupied or empty. In crystalline electrolytes, the sites for the mobile ions are clearly defined by the structure of the immobile sublattice (unlike melts, for instance, where there is no fixed set of sites). Ionic conduction occurs, therefore, by means of a series of definite hops between adjacent sites in the conduction pathway. Most of the time, the 'mobile' ions are located in a particular site, where they undergo thermal vibrations within the site. Occasionally, they escape from their site and hop into an adjacent site where they may then reside for a considerable time before either moving on further or hopping back into their original site.

With aliovalent doping of cations, there are four fundamental ionic mechanisms for achieving charge balance. (There are also electronic compensation mechanisms leading to electron/hole creation and possibly to electronic conduction; these are not considered here.) These four ionic mechanisms are shown in Table 2-1, together with an example of each. Doping with a higher valent cation necessitates the creation of either cation vacancies (1) or anion interstitials (2), whereas doping with lower valent cations leads to the creation of either interstitial cations (3) or anion vacancies (4).

In the examples and formulae shown, the number of vacancies or interstitials increases with x. Usually in a particular material, there is a practical limit as to how many vacancies/ interstitials can be introduced while still retaining a homogeneous solid solution phase. In many cases, this limit is small, <<1% but in others it may be large, 10-20%, giving rise to massive defect concentrations. Occasionally, it is possible to vary the composition to such an extent that it is possible either to fill completely a set of interstitial sites or to empty completely a particular set of lattice sites.

When this happens, random walk theory predicts that at the half-stage, when the

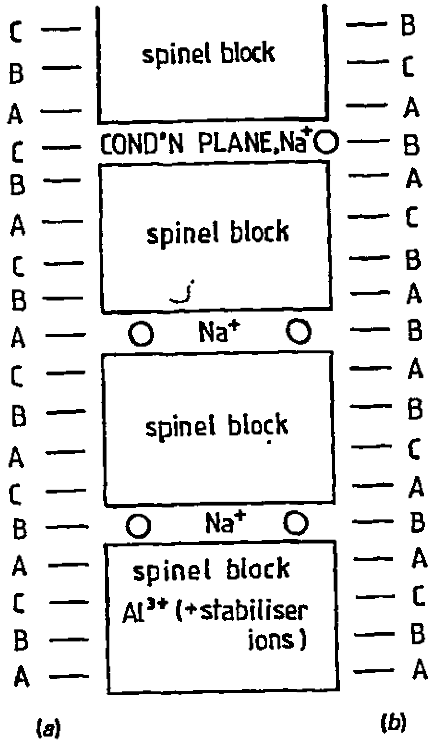

Figure 2-3. Schematic structure of a) β" and b) β alumina showing two dimensional ion migration paths

concentrations of filled and empty sites are equal, the ionic conductivity should pass through a maximum because the product of the concentration of mobile species, C_i, and sites to which they may migrate $(1-C_i)$ is at a maximum.

2.3.3. The Activation Energy for Conduction

The activation energy for conduction, ΔH_m, which is regarded as a series of potential wells and barriers, is the major factor controlling the ionic mobility, u. The Arhennius expression for conductivity is

$$\sigma = Ae^{-\Delta H_m / RT} \qquad \text{Eq. 2-15}$$

Table 2-1. Solid solution formation by doping with aliovalent ions [Bru95]

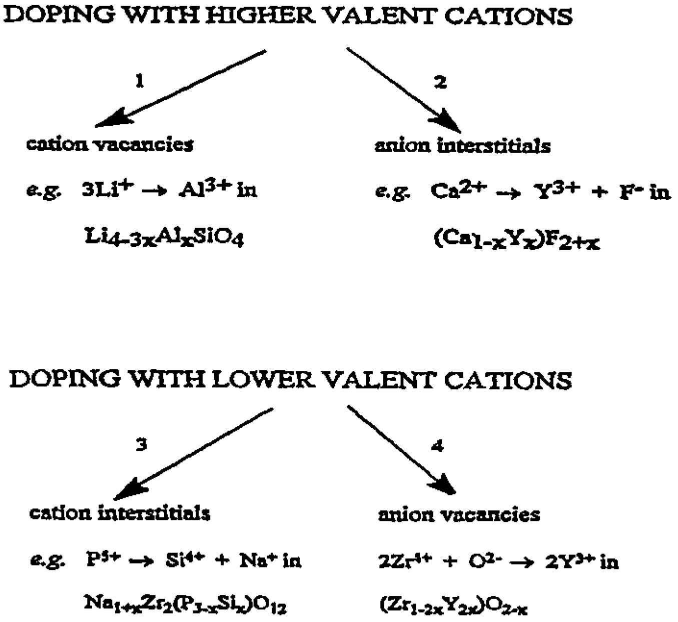

The activation energy represents the ease of ion hopping, shown in Figure 2-4. It is related directly to the crystal structure and in particular, to the openness of the conduction pathways. Most ionic solids have densely packed crystal structure with narrow bottlenecks and without obvious well-defined conduction pathways. Consequently, the activation energies for ion hopping are large, usually 1 eV or greater and conductivity values are low. In solid electrolytes, open conduction pathways exist and activation energies are much lower, as low as 0.03 eV in AgI, and 0.15 eV in β-alumina for example.

All solid state ionic conduction proceeds by means of hops between well-defined lattice sites. Ions spend most of their time on specific sites where their only movement is that of small oscillations at lattice vibrational frequencies (10^{12}-10^{13} Hz). Occasionally, ions can hop into adjacent sites. The ions hop quickly, on a time-scale approaching but somewhat longer than that of a single lattice vibration. This is because the hop distance, typically 0.1 ~ 0.2 nm, is an order of magnitude greater than the atomic displacement during a lattice vibration.

Activation energy is a complex parameter that includes not only a physical barrier, in which an ion has to squeeze through a narrow bottleneck, but also a longer range electrostatic barrier between the mobile ions. This arises whenever an ion hops out of a regular

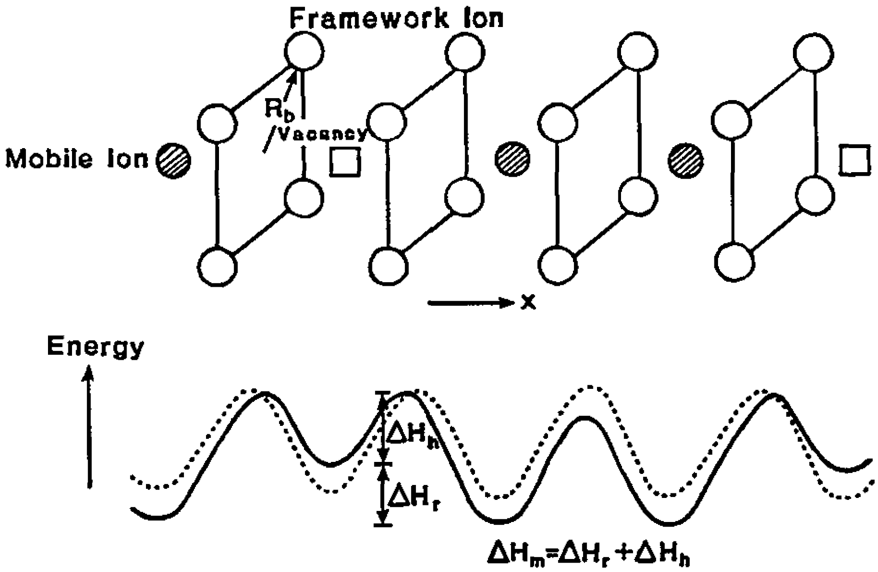

Figure 2-4. Thermal energy needed for an ion jump,

lattice site. Hopping generates local departures from electroneutrality, which may also be viewed as the creation of dipoles. Such departures from local electroneutrality act as a drag on further ion hops. Local electroneutrality can be restored, however, by means of a redistribution in the positions of the surrounding ions. After this process is complete, the ion under consideration is able to move again.

In materials with a high carrier concentration, mobile ions are inevitably quite close together, separated by at most a few Angstroms. Consequently, ions cannot hop in isolation but are influenced by the distribution of mobile ions in their vicinity.

2.3.4. Application of Solid Electrolytes

Major utilization to date has involved the employment of oxide ion conductors at elevated temperatures to measure oxygen partial pressures in molten steel, automobile exhaust, and sodium ion conductors (notably materials of the sodium beta alumina family) as solid electrolytes in elevated temperature battery systems. A variety of silver ion conductors are being used in several room temperature electrical devices, such as timers and coulometers; a fluoride ion conductor is the active element in a commercially available selective ion electrode for use in analytical chemistry. There are, of course, many other possible applications for solid electrolytes if materials with proper characteristics can be found or developed. A number of these are listed in Table 2-2.

Table 2-2. Examples of applications of solid electrochemical techniques [Bru95]

Static EMF measurements

Free energy of formation of binary and ternary compounds

Free energy changes accompanying various cell reactions

Thermodynamics of binary phases

Determination of limits of stoichiometry of compounds

Effective mass of electrons or holes in semiconductors

Solubility of gases in liquids

Time-dependent EMF measurements

Phase boundary migration kinetics

Supersaturation required for nucleation within and upon solids and liquids

Combinations of EMF and current measurements

Diffusion in liquid and solid metals and mixed conductors

Transport of both ionic and electronic species across phase boundaries

Kinetics of condensation and vaporization processes

Oxidation and reduction reactions on solid surfaces

Thermodynamics of gaseous species

Studies of the mechanism of catalysis

Ionic and electronic partial conductivities in mixed conductors

Structure of electrode-electrolyte interfaces

Technological applications

Batteries

Fuel cells

Catalysts

Electro-chromic display elements

Variable resistors

Thermoelectric devices

Memory elements

Solute valence control in semiconductors and ionic solids

Purification of liquid and gases

Measurement and control of liquid and gas compositions

2.4. A Classification of Li Solid Electrolytes

The specifications for high temperature Li electrolyte materials are quite stringent. The solid electrolyte must, for example, have good ionic conductivity at the operating temperature (ideally 0.1 S/cm at 400°C in applications requiring mass transfer). Electronic conductivity must be negligible at all temperatures to avoid internal short circuits. The solid electrolyte must be stable in contact with the electrodes, typically a molten Li or Li alloy. For practical reasons, materials should be relatively low cost, easy to fabricate on an industrial scale and environmentally benign. Figure 2-5 shows the variation in conductivity with temperature for some well-known lithium ion conducting solid electrolytes.

2.4.1 Li_4SiO_4 and Related Phases

Stoichiometric Li_4SiO_4 has a relatively modest lithium ion conductivity of 5×10^{-4} S/cm at 300°C [Wes73, Hod76, Jac85]. The conductivity is improved for solid solutions between Li_4SiO_4 and either Li_4GeO_4 or Li_4TiO_4 [Wes73, Hod76, Jac85] to a maximum of around 2×10^{-1} S/cm at 300°C for the composition $Li_4(Si_{0.6}Ti_{0.4})O_4$ [Wes73]. A more significant enhancement occurs on partially substituting Si^{4+} by an aliovalent species such as P^{5+} to form the solid solution series $Li_{4-x}Si_{1-x}P_xO_4$, thereby creating lithium vacancies [Hu76, Hug77, Sha77]. Maximum conductivity of 1×10^{-4} S/cm is observed for $x = 0.4$ at 100°C. The activation energy for conduction, E_a, is smaller, 0.56 eV [Hug77] than that of Li_4SiO_4, 0.87 eV [Wes73, Hod76, Jac85]. Similar effects have been observed by partially substituting Si with either As or V [Kho82, Kho84] and conductivities of more than 0.1 S/cm at 400°C were obtained. Phase diagram studies of these three systems [Kho82, Kho84, Kho81], have shown that in each, there are two ranges of solid solution. At the Li_4SiO_4 -rich end, compositions have the monoclinic-type Li_4SO_4 structure, but at some intermediate value of x there is a change to orthorhombic γ_{II}-Li_3PO_4 type structure. Although there are two families of structures in these systems, the conductivity appears to be controlled mainly by the number of mobile Li^+ ions rather than the specific structure adopted.

Li_4SiO_4 can also be partially substituted with both trivalent and divalent cations. Di-

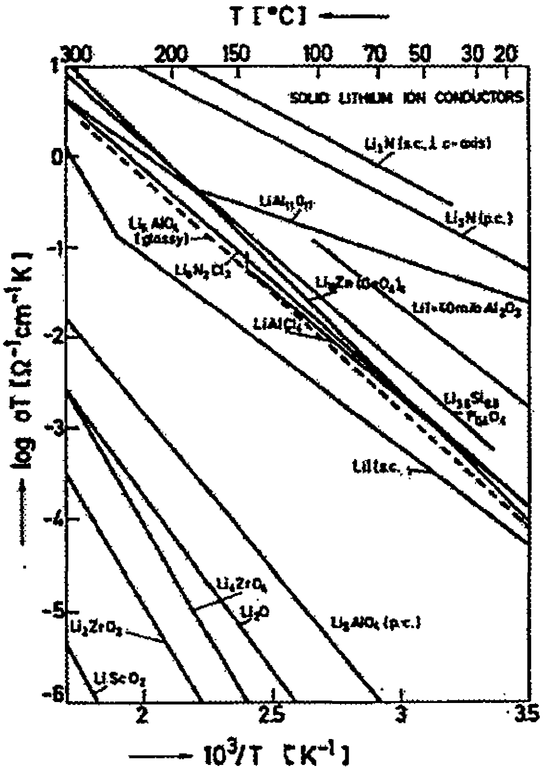

Figure 2-5. Some well known Li ion conductors

valent cations include Zn, Mg, Co and Ni [Wes70, Wak88, Sai90]. For the solid solution, $Li_{4-2x}Mg_xSiO_4$, the single phase region extends to x = 0.5, with a maximum conductivity of 2.3×10^{-5} S/cm at 200°C rising to 1.5×10^{-2} S/cm at 400°C [Wak88], which is about one order of magnitude less than required for thermal battery applications. However, these materials are relatively easy to prepare, are stable in air, have an electronic conductivity which is about three orders of magnitude less than the ionic conductivity and maintain their ionic conductivity over a long period of time [Wak88].

Trivalent cations such as B, Al, Ga, Cr, Fe and In [Sai90, Sai91, Jac83, Qui89, Cha96, Mas95, Neu96] can partially substitute into Li_4SiO_4 giving rise to either Li interstitial or Li vacancy-based solid solutions of general formulae: $Li_{4+x}M_xSi_{1-x}O_4$ ($Si^{4+} \Rightarrow Li^+ + M^{3+}$)

and $Li_{4-3y}M_ySiO_4$ ($3Li^+ \Rightarrow M^{3+}$), respectively. Interstitial solid solutions are favoured by B, Cr and Fe; In forms only vacancy based solid solutions; Al and Ga form both. In general, conductivity decreases as the size of M^{3+} increases, for a given amount of substitution [Sai90, Cha96]. Boron-substituted materials are an exception, however, and have lower conductivities than expected due to rapid sample ageing in air, producing Li_2CO_3 impurities [Mas95].

The interstitial solid solutions $Li_{4+x}M_xSi_{1-x}O_4$ between Li_4SiO_4 and the antifluorite-related phase, Li_5AlO_4 have potential applications in high voltage lithium cells [Neu96]. Of particular interest is the composition Li_9SiAlO_8 ($x = 0.5$) which has the Li_4SiO_4 -type framework. Room temperature conductivity of Li_9SiAlO_8 is about four orders of magnitude higher than either end-member but is still quite poor at 2.3×10^{-7} S/cm. Measurements were made only up to 100°C [Neu96] and higher temperature data are, therefore, required. Li_9SiAlO_8 is stable versus Li/Li^+ up to 6.5 V, making it suitable for studying high voltage cathode materials and is inert against $LiMn_2O_4$ to 500°C [Neu96]. It is stable against Li only to around 100°C [Neu96].

2.4.2. Li_5MO_4 and Related Phases

The anti-fluorite phases, Li_5MO_4, (M = Al, Ga, Fe) and solid solutions of the type $Li_{5+x}M_{1-x}M'_xO_4$ (M'= Zn, Mg) have also been studied as solid electrolytes [Hug77, Esa87]. Li_5MO_4 has a low-temperature α and high-temperature β polymorph, and both forms have cation vacancies relative to the ideal anti-fluorite A_2O stoichiometry. The β polymorph has significantly higher conductivity, 0.3 S/cm at 450°C for the Al analogue [Hug77], which is comparable with that of molten salts. Conductivities below 400°C are quite low and these materials have limited practical applications in low temperature batteries due to their narrow operating temperature range. Conductivity at lower temperatures improves on substitution of some M^{3+} for $Li^+ + Zn^{2+}$. Maximum values reported are 1.5×10^{-3} S/cm for $Li_{5.9}Al_{0.1}Zn_{0.9}O_4$ and 7.0×10^{-3} S/cm for $Li_{5.5}Fe_{0.5}Zn_{0.5}O_4$ at 300°C [Esa87].

2.4.3. LISICONS

In contrast to Li_4SiO_4, any attempted aliovalent doping of either Li_4GeO_4 [Vol69] or Li_4TiO_4 [Dub72, Dub73] leads predominantly to be γ_{II}-Li_3PO_4 type phase, the co-called LISICON. The first material to be given the name LISICON, which stands for lithium super ionic conductor, was $Li_{14}Zn(GeO_4)_4$ which is a member of the solid solution, $Li_{2+2x}Zn_{1-x}GeO_4$ [Hon78, Bru80]. This series contains interstitial lithium ions and extends over the range $-0.36 < x < +0.87$ but its extent is very temperature dependent. $Li_{14}Zn(GeO_4)_4$, has very high conductivity at high temperatures, 0.125 S/cm at 300°C, but only 1×10^{-7} S/cm at room temperature [Bru82]. Replacement of Zn by Mg causes a decrease in conductivity [Hon78].

LISICONS tend to show marked reduction in ionic conductivity with time at low temperatures. This is explained by trapping of the mobile lithium ions by the immobile sub-lattice at lower temperatures via the formation of defect complexes [Bru84]. Re-annealing samples causes the conductivity to rise to its original value. This could be seen as an attractive feature for thermal battery applications where long storage times at low temperatures (when conductivity should be negligible) followed by a relatively high operational temperature (when ionic conductivity should be high) are envisaged.

Another important group of γ_{II}-Li_3PO_4 type solid solutions [Hu76, Hug77, Sha77, Kho82, Kho84, Kho81, Kuw80, Qua83, Rod85, Sum95, Dis95, Yam96], referred to above, form between Li_4XO_4 and Li_3ZO_4 (X= Si, Ge, Ti and Z = P, As, V, Cr) and have general formula $Li_{3+x}Z_{1-x}X_xO_4$. The conductivities of intermediate compositions are much higher than those of the end-members. These materials have comparatively good conductivity at room temperature, are thermodynamically stable and relatively insensitive to atmospheric attack but on prolonged standing (several months) some systems containing Ge or Ti do show ageing effects [Rod85]. The highest room temperature conductivity is 4×10^{-5} S/cm for $Li_{3.6}Ge_{0.6}V_{0.4}O_4$ [Kuw80] and this material, in conjunction with LiI additive, has already been used in a high temperature thermal battery by the U.S. Army [Bef95]. The silicate analogue, $Li_{3.6}Si_{0.4}V_{0.6}O_4$, has very recently been used in rechargeable thin film cells [Yam96] and is stable in contact with lithium, even above 180°C when lithium is molten. It also has the advantage over $Li_{3.6}Ge_{0.6}V_{0.4}O_4$ of being less expensive to produce and having a slightly lower conductivity at lower temperatures (about 1×10^{-5} S/cm at 25°C).

No examples have been found of solid solutions in the systems Li_4XO_4 (X= Si, Ge, Ti)-$LiTO_2$ (T = Al, Ga) and it was thought that trivalent ions did not readily enter the LISICON structure. However, high conductivity solid solutions have been found more recently in systems which have $Li_{2.5}T_{0.5}XO_4$ (T = Al, Ga; X = Si, Ge) as the second end-member [Qui89, Gar90, Smi91, Smi91A, Iva88, Lee91, Lee93, Rob92, Rob94, Rob93]. These solid solutions have the general formula, $Li_{4-3x}T_xXO_4$, the substitution mechanism being $3Li^+ = T^{3+}$.

In the two silicate systems [Qui89,Qui89A, Gar90, Smi91, Smi91A], the conductivity rises to a maximum for compositions around x = 0.2-0.3 and decreases to nearly zero for x = 0.5 ($Li_{2.5}T_{0.5}SiO_4$). There is some evidence that the conductivity may rise again for $0.5 < x < 0.6$ [Qui89]. The highest conductivity is obtained in the Al-containing system [Gar90], 3×10^{-5} S/cm at 100°C, which is nearly an order of magnitude higher than for the Ga system. These are the first phases to have a structure based on γ-$LiAlO_2$, and to exhibit high conductivity [Smi91,Smi91A].

The two germanate systems [Iva88, Lee91, Lee93, Rob92, Rob94, Rob93], yield highly conducting γ-solid solutions with the LISICON structure; the Arrhenius plots in both are markedly nonlinear [Lee91, Lee93, Rob92, Rob94]. Indeed, in the Al system, compositions with low x, ~0.1 to 0.25, have zero activation energy for conduction at temperatures above 700°C, indicating a liquid-like disorder of the mobile lithium ions [Lee91, Lee93,]. The conductivity of samples in both systems meet the requirements for thermal battery applications, e.g., 0.5 S/cm at 560°C for x = 0.2 in the Ga system [Rob92]; however, the materials are susceptible to atmospheric attack and ageing effects due to ordering of the lithium ions [Rob93]. Elements such as Ga and Ge are expensive.

2.4.4. NASICONS and Related Phases

The term NASICON, which stands for Na^+ super ionic conductor, was given to the solid solution phase $Na_{1+x}Zr_2Si_xP_{3-x}O_{12}$, x =2.0, discovered by Hong and Goodenough in 1976 [Hon76, Goo76]. The end-member $NaZr_2(PO_4)_3$ has very low ionic conductivity, but it can be increased substantially on aliovalent doping, rising to 0.2 S/cm at 300°C for x = 2.0, higher than that of sodium β-alumina.

The lithium-containing analogues, $LiM_2PO_4)_3$ with M^{4+}=Zr [Tay77], Ti [Rob93], Ge [Aon93] and Hf [Ala84] also have NASICON-type structures. These consist of corner-sharing MO_6 and PO_4 polyhedra which form a rigid $[M_2(PO_4)_3]^-$ framework and the lithium ions move through tunnels in a three-dimensional pathway [Hag68]. There are two different lithium ion sites in the structure, labelled I and II. In stoichiometric $LiM_2(PO_4)_3$, the type I sites are full and the II sites are empty.

The substitution mechanisms are $Li^+ + M^{4+} \Leftarrow\Rightarrow A^{5+}$ to form Li vacancies and $M^{4+} \Leftarrow\Rightarrow Li^+ + M^{3+}$ to form lithium interstitials. The metal ions include M^{4+} = Zr, Hf, Ti and A^{5+}= Nb^{5+}, Ta^{5+} . The maximum conductivities observed are for $Li_{0.1}Zr_{0.1}Ta_{0.9}(PO_4)_3$, i.e., x=0.9, where σ =6 × 10^{-6} S/cm at 25°C, rising to 2 × 10^{-3} S/cm at 200°C [Cho89]. It is extremely difficult to obtain good ceramics with these materials and so the total conductivity is one or two decades less than this value, due to the presence of grain boundary resistances.

The reason for the high conductivities in these materials is still a point of contention in the literature. Some authors believe that stoichiometric $LiTi_2(PO_4)_3$ has a high Li^+ ion conductivity, and that Ti^{4+} is not replaced by M^{3+} but instead, a glassy second phase forms at the grain boundaries which reduces the grain boundary resistance and increases the densification of the ceramic [Aon93]. As evidence for this, the porosity of undoped $LiTi_2(PO_4)_3$ was around 34.0% compared with only 4.1% for $Li_{1.3}A_{0.3}Ti_{1.7}(PO_4)_3$. Similar results were obtained by adding a low-melting flux such as Li_2O, Li_3PO_4, Li_2CO_3 or Li_3BO_3 to $LiTi_2(PO_4)_3$ to increase the sinterability of the ceramic [Aon93]. However, phase diagram studies of the ternary system $Li_2O-TiO_2-P_2O_5$ show no evidence of such a solid solution.

The Ge and Hf analogues have only slightly lower conductivities, up to $(1\sim2) \times 10^{-4}$ S/cm at 25°C [Aon93], and are stable against lithium but are significantly more costly to produce.

2.4.5. Lithium Rare Earth Titanate Perovskites

Perovskites (general formula ABO_3) and related structures are extremely important solid state materials and have uses in a variety of applications such as high T_c superconductors, cathodes in solid oxide fuel cells, giant magnetoresistors and ferroelectrics. Oxide ion conductivity is well known in some nonstoichiometric perovskites but it was not until 10 years ago that high lithium-ion conductivity was demonstrated in $Li_{0.5-3x}La_{0.5+x}TiO_3$ [Ina93]. The bulk ionic conductivity is as high as 1×10^{-3} S/cm at room temperature, but the total conductivity is significantly less, 2×10^{-5} S/cm, due to grain boundary resistances [Ina93]. The electronic conductivity is estimated to be less than 1×10^{-8} S/cm at room temperature [Ina93]. The activation energy for conduction is very low, 0.34 eV, and hence bulk ionic conductivity rises to only about 0.2 S/cm at 440°C . The other rare earth analogues show substantially reduced ionic conductivities, e.g., the Pr analogue (x=0.08) has a maximum value of 4 × 10^{-5} S/cm at 25°C [Mor96]. This appears to be due to the lanthanide contraction causing a reduction in the size of the percolation pathways in the crystal lattice [Kaw94]. Conversely, substitution of 5 mol % Sr for (Li, La) at the A-site causes a small increase in the bulk conductivity to 1 × 10^{-3} S/cm at room temperature, due to lattice expansion [Ina94].

Despite the exceptionally high bulk lithium ion conductivity of these perovskites, they suffer from several serious problems. The electronic conductivity increases dramatically in contact with Li metal as Ti^{4+} is reduced to Ti^{3+} and some Li^+ is intercalated into the lattice [Ina93]. On the other hand, it is extremely difficult to obtain dense ceramics free of grain boundary resistances without substantial Li_2O loss, due to the high sintering temperatures (1300°C) required [Bro96].

2.4.6. Li_2SO_4 and Related Phases

Lunden and co-workers studied these materials extensively for the last 30 years. Li_2SO_4 has two polymorphs, a low temperature monoclinic β phase with low conductivity, and a high temperature α (fcc) phase with conductivity of 1 S/cm at 575°C, increasing to 3 S/cm at 800°C [Hee77]. Li_2SO_4 melts at 860°C [Hee77].

Studies of the systems Li_2SO_4-M_2SO_4 (M=Na, K, Ag) have shown the existence of the phases $LiMSO_4$ which are body centred cubic (bcc) and have high ionic conductivities at slightly lower temperatures [Tdr96]; $LiNaSO_4$ [Sta72], has high conductivity between 518°C and 615°C, e.g., 0.93 S/cm at 550°C [Lun86]. The phase diagram [Sta72] has a eutectoid at 465°C with an fcc phase above a composition of 77.5 mol % Li_2SO_4: 22.5 mol % Na_2SO_4. Conductivity is anisotropic and is highest parallel to the c-axis [Pim88]. Values rise from 0.04 S/cm at 440°C to 0.3 S/cm at 500°C [Pim88].

Attempts have been made to substitute Li with a divalent ion thereby creating lithium vacancies; the phase diagrams Li_2SO_4-LiM'SO_4, have been reported, where M'= Be, Mg, Ca, Sr, Ba, Zn, Cd and Mn [Lun94]. The Zn-containing system has a non-cubic solid solution between 17 and 43 mol % $ZnSO_4$ but the compositional range is very temperature dependant [Lun83]. The parent stoichiometry may be $Li_4Zn(SO_4)_3$ and the conductivity is 1 S/cm at 550°C; however, it has a limited thermal stability range which is also compositionally dependant [Lun83].

The systems Li_2SO_4-Li_3AO_4 (A= P^{5+}, V^{5+}) show limited solubility of the pentavalent ion in the α-Li_2SO_4 structure and there is an initial decrease in conductivity on partial substitution of S by A. Surprisingly, the conductivity rises sharply again in both systems for intermediate compositions which are two-phase mixtures; this is attributed to an interfacial conduction mechanism, which is now thought to be common in composite ionic conductors [Tou90]. Maximum conductivities are still less than that of the Li_2SO_4.

2.4.7. Li_3N and Related Phases

Single crystals of lithium nitride, Li_3N, with a layered crystal structure, have very high ionic conductivity 0.1 S/cm at room temperature, perpendicular to the c-axis, but about two orders of magnitude less parallel to the c-axis. The highest conductivity reported in polycrystalline Li_3N is 4×10^{-4} S/cm at 25°C [Rea79]. Unfortunately, the use of Li_3N in practical applications is very limited due to its low theoretical decomposition potential of 0.445 V [Alp77]. The crystal structure comprises alternating layers of Li_2N and Li perpendicular to the c-axis [Rab76]. Attempts have been made to dope Li_3N and create new phases with higher decomposition voltages, e.g. Li_3AlN_2, has a cubic anti-fluorite type structure and a decomposition potential of 0.85 V at 104°C [Sch86]. The conductivity is, however, only 5×10^{-8} S/cm at room temperature. LiMgN has the anti-fluorite structure but its conductivity is even lower [Sch86]. Li_8SiN_4 has not yet been fully characterized and the structure is unknown at present but its conductivity is higher, 5×10^{-4} S/cm at 125°C, possibly due to a higher number of interstitial lithium ions [Yam87]. Other systems such as Li_3N-LiI have also been studied [Oba81].

Li_3N is not quite stoichiometric; there are 1~2 at.% Li vacancies associated with H impurities and these appear to be essential to the high ionic conductivity of lithium nitride [Lap83]. On adding LiOH to a Li_3N-LiI (1:2) mixture, conductivity is enhanced significantly [Oba81A] up to a maximum of 0.95×10^{-3} S/cm at 25°C for Li_3N-LiI-LiOH (1:2:0.77). The decomposition voltage is around 1.6 V [Oba81A]. These materials are, however, very hygroscopic.

2.4.8. Lithium Metal Halides

Lithium metal halides have been investigated as solid electrolytes for more than 15 years. Most interest has centred on phases, Li_2MCl_4, where M = Mg, Mn, Ti, Cd, Cr, Co, Fe and Zn [Kan89]. With the exception of M= Zn, these materials are inverse spinels with half the lithium ions occupying tetrahedral sites and half sharing octahedral sites with the M^{3+} ions [Kan88]. Li_2ZnCl_4 is a normal spinel with most lithiums occupying octahedral sites [Kan89]. Almost all of these chlorides exhibit phase transformations in the range 300-500°C [Kan88]. Cubic spinels such as Li_2MnCl_4, Li_2MgCl_4, and Li_2CdCl_4 transform to a defect NaCl-type structure where half of the lithiums occupy 16c sites, and the 16d sites retain the same distribution as in the spinel [Kan88]. Other phases such as the Cr, Fe and Co analogues are distorted spinels at low temperatures due to cation ordering and transform to cubic spinels at higher temperatures [Kan88]. Highest conductivities are obtained for the cubic spinels. Li_2MnCl_4 and Li_2MgCl_4 have an ionic conductivity of 0.14 S/cm at 400°C; Li_2CdCl_4 has a slightly higher value 0.3 S/cm at 400°C rising to 1.0 S/cm at 500°C . The ordered spinels have values that are two to three orders of magnitude less [Kan88]. The normal spinel, Li_2ZnCl_4 has a poorer conductivity, 2×10^{-4} S/cm at 280°C [Kan89]. The lower conductivity in these materials is believed to be associated with the more restricted conduction pathways for the octahedrally coordinated lithiums.

Attempts at substituting Na or Cu for Li caused reductions in the conductivity due to the mixed alkali effect [Lut91]. The iodide systems LiI-MI_2 (M= Mn, Cd, Pb) demonstrate fast ion conductivity, up to 0.1 S/cm at 300°C for Li_2CdI_4, and Li_2PbI_4 [Lut93].

2.4.9. Lithium Carbonate

Pure Li_2CO_3 is a lithium ion conductor whose structure is monoclinic (C12/c1). The lattice parameters are a=8.359Å, b=4.974Å, c=6.194Å and β=114.8° [JCPDS22-1141].

The conduction along the (002) plane is much larger than that perpendicular to (002). The conductivity of Li_2CO_3 is similar in magnitude to that of Li_4SiO_4, Li_5AlO_4 and Li_2SO_4. The conduction in Li_2CO_3 is essentially by interstitial lithium ions.

In the lithium carbonate crystal, large plenary CO_3^{2-} ions compose the (002) planes and small lithium ions occupy sites between the oxygens of the neighboring CO_3^{2-} ions. Therefore, Frenkel defects in lithium sites may be easier to form than Schottky-type or anion-cation interstitial defects. Lithium ion conduction takes place essentially along the (002) plane [Miz92].

2.4.10. Lithium Oxide

Li_2O has an antifluorite-cubic structure, where oxygen ions are in an fcc sublattice and lithium ions in a simple cubic sublattice. The structure is the inverse of the cubic fluorite structure such as that of CaF_2 or stabilized zirconia. The values of the self-diffusion coefficients of the oxygen ion in the cubic fluorite structure oxides are large, about 10^{-4} cm^2/s at just below the melting point in the solid state which is nearly the same as that in the liquid state. The lithium ion displays the same behavior as the oxygen ion in the cubic fluorite structure.

A report [Ohn83] showed the conductivity of Li_2O depends largely on the humidity in the environment. The activation energies of the conductivity changed from 0.4 eV in dry conditions to 0.7 eV in wet conditions. The marked change in conductivity of Li_2O in a wet environment was explained by the melting and decomposition of LiOH formed in the sample.

2.4.11. Other Lithium-Ion Conducting Solids

One of the earliest materials to be studied as an ionic conductor was sodium β-alumina, which has a 2-D layered structure [Whi71]. The lithium analogue, $Li_2O.11Al_2O_3$, has lower conductivity but it is still very high, 3×10^{-3} S/cm at room temperature for single crystals [Far85]. Li β-alumina can easily be prepared by ion exchange in molten LiCl salt and is stable in air. However, it is a metastable phase that does not appear on the Li_2O-Al_2O_3 phase diagram, and would therefore decompose during high temperature presintering [Pet88].

Several other families of phases have been investigated and are listed briefly below. Ionic conductivities are generally less than the materials discussed until now. The ramsdellite phase $Li_2MgSn_3O_8$, has a fairly low conductivity, even at elevated temperatures e.g., 1.2×10^{-8} S/cm at 300°C [Lew85]. Creating lithium interstitials by partial substitution of 2 Li^+ in place of Mg^{2+} improves the conductivity by several orders of magnitude, e.g., 5×10^{-4} S/cm for $Li_{2.6}Mg_{0.7}Sn_3O_8$ [Gri86], but it is still too low for practical applications.

The system $LiYO_2$-Li_2ZrO_3 shows solid solution formation [Zou93] with a maximum conductivity of 1.2×10^{-2} S/cm at 500°C for undoped $LiYO_2$. The zircon-like phase YPO_4 is an insulator, but substitution of $Y^{3+} \rightarrow 3Li^+$ yields a lithium ion conductor with $\sigma_{600°C}=3.7 \times 10^{-2}$ S/cm for $Y_{0.8}Li_{0.6}PO_4$ [Esa89]. Interestingly, Ca doping of YPO_4 creates a Ca^{2+} ion conductor [Esa89].

Lithium rare earth silicates '$LiLnSiO_4$' with an apatite-related structure show modest conductivity, up to 2×10^{-4} S/cm at 400°C for the Sm analogue, but have not been prepared as single-phase [Sat96]. The conductivity enhancement is believed to be due to a composite-type effect which is to lower grain boundary resistances.

2.4.12. Composite Materials

Composite materials comprise an intimate mixture of lithium-ion conducting solid electrolyte and insulating ceramic powder [Wag89]. The first such system to be studied was LiI-Al_2O_3 and conductivity was enhanced significantly with respect to LiI [Lia73]. The enhancement is ascribed to an increase in interfacial transport by one to two orders of magnitude. Al_2O_3 particle size has a large influence on the conductivity of the host matrix [Nag93]. Several detailed models have been proposed to explain these phenomena [Nag93].

Other composite systems studied include $Li_{16-2x}Zn_x(GeO_4)_4$, (LISICON)-ZrO_2 [Ayg89];

Li_3PO_4-Al_2O_3 [Nag94]; Li_2SO_4-Al_2O_3 [Uva94]; $LiNO_3$-Al_2O_3 [Uva96]; and Li_nX-Al_2O_3 ($X=F^-$, Cl^-, Br^-, CO^{2-}_3) [Uva92]. Either mechanical mixing or thermal decomposition of salts is used to obtain the samples.

2.5. Practical Aspects of Li Solid Electrolytes

2.5.1. Selection of Li Solid Electrolytes

To date it appears no solid Li ion conductor mentioned before in this chapter has found widescale commercial application. Most Li ion conductors are thermodynamically unstable against Li. Thermodynamic stability against Li is a necessary condition in devices used to measure the absolute potential of lithium alloy systems.

Solid electrolytes, which are to be used in high temperature applications should possess high ionic conductivity at operating temperature, and negligible electronic conductivity at all temperatures. They should be stable in contact with the electrodes and be relatively simple and inexpensive to prepare on a large scale. These simple considerations lead to the following general criteria for the quality of a solid-electrolyte material to be used in an electrochemical cell.

Electrochemical cells are of two types: power cells and sensors. In an ideal power cell, the ionic current through the electrolyte inside the cell matches an electronic current through an external load. The solid electrolyte is in the form of a membrane of thickness L and area A that separates electronically the two electrodes of the cell. Any internal electronic current across the electrolyte reduces the power output. The internal resistance to the ionic current is

$$R_i = L / \sigma_i A$$ **Eq. 2-16**

where σ_i is the ionic conductivity of the electrolyte, R_i is the resistance to ion transport, L is the thickness and A is the area. For a current I through the cell, the voltage IR_i represents a potential drop that is to be minimized. Even in potentiometric sensors, the resistance R_i must be maintained below a certain level to obtain satisfactory sensitivity and speed of response, and any electronic contribution to the internal cell current must be factored into cell calibration. Hence, the following requirements must be met:

i) To minimize R_i and obtain a mechanically strong membrane of small L and large A, optimization of cell design may require the fabrication of membranes of complex shape.

ii) Unless an exceptionally small L/A ratio is feasible, a satisfactory R_i generally requires a $\sigma_i > 10^{-2}$ S/cm at operating temperatures. In general, the conductivity is a tensor, but for polycrystalline electrolytes a scalar σ_i is used. However, for tunnel or layered structures having ionic conductivity in one or two dimensions only, it is necessary to appreciate that $\sigma_{//} \neq \sigma_{\perp}$, so the scalar σ_i measured may be considerably reduced from the ionic conductivity in the optimum direction within an individual grain.

iii) A transport number t_i near unity:

$$t_i = \sigma_i / \sigma \cong 1, \qquad where \qquad \sigma = \sum{}_j \sigma_j + \sigma_e$$ **Eq. 2-17**

where σ_e is the electronic conductivity. In general there is only one mobile ion in a solid electrolyte so that $\sum_j \sigma_j = \sigma_i$. Because any electron mobility is much greater than the ionic mobility ($u_e >> u_i$), only a relatively small number of electronic carriers can degrade t_i to an unacceptable level.

iv) A low resistance to ion transfer across the electrode/electrolyte interfaces.

v) Chemical stability in the working environment requires that the electrolyte is neither reduced by the reductant at the negative electrode nor oxidized by the oxidant at the positive electrode. Thermodynamic stability is only achieved by placing the bottom of the electrolyte conduction band above the highest occupied molecular orbital (HOMO) of the reductant and the top of the electrolyte valence band below the lowest unoccupied molecular orbital (LUMO) of the oxidant, as illustrated in Figure 2-6.

vi) the mobile ion of the electrolyte must be the working ion of the cell.

vii) Cost of material and fabrication is always a consideration.

Hellstrom and Van Gool [Hel80] described the criteria for the thermodynamic stability of compounds composed of Li_2O and another metal oxide (M_xO). The literature for the Li_2O-M_xO systems in which ternary phases are stable against Li is reviewed. The binary phase M_xO is thermodynamically stable against Li if the Gibbs energy is positive for the reaction

$$2Li + M_xO = Li_2O + xM \qquad \text{Eq. 2-18}$$

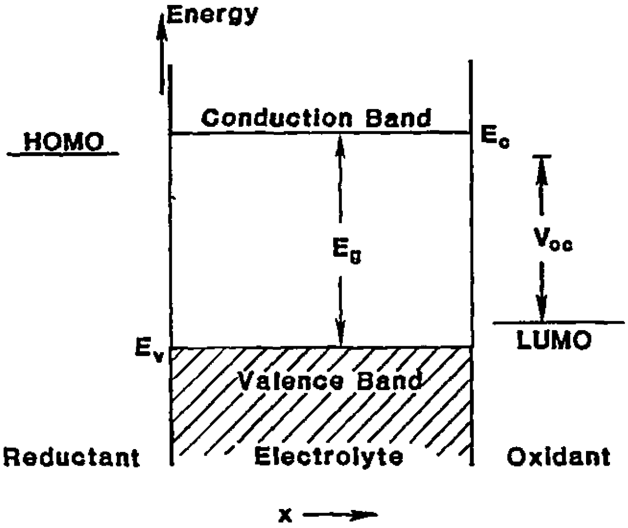

Figure 2-6. Placement of reactant energies relative to the edges of the electrolyte conduction and valence bands in a thermodynamically stable electrochemical cell at flat-band potential

The relative stability of the various binary oxides is easy to compare using a plot of the Gibbs energy of formation of the binary oxides, normalized in this article to the consumption of half a mole of molecular oxygen, as a function of temperature. Those phases whose Gibbs energy of formation more negative than that of Li_2O are stable against Li, and are shown in Figure. 2-7.

A ternary phase Li_aM_bO, where a and b are respectively the number of Li and M ions per O, is stable against Li if for the reaction,

$$Li_\alpha M\ \ O+(2-\alpha)Li=Li_2O+\beta M \qquad \textbf{Eq. 2-19}$$

the Gibbs energy is positive. Here it is assumed that no Li_xM phases form in the Li-M system.

The stability was estimated where no data were available [Hel80]. The most stable oxides are formed from metals in group IIA, IIIB, (including the rare earths) and IVB of the Periodic Table. As a rule, the electrolyte should be 250 kJ/mol more stable than the oxide of the sample metal.

2.5.2. Lithium Yttrate ($LiYO_2$)

$LiYO_2$ was selected as the electrolyte for our system since it is stable against Li [Yam00]. However, it has been observed that $LiYO_2$ is not thermodynamically stable in air at or near room temperature, decomposing into Y_2O_3 and other lithium compounds [Eic81]. On the other hand, decomposition can be prevented by exclusion of moisture and CO_2.

Lithium yttrate is monoclinic with a slightly distorted NaCl structure that consists of mixed cation layers between layers of close-packed O^{-2} [Zha93]. The cell parameters are $a = 6.12$Å, $b = 6.19$Å, $c = 6.21$Å and $\beta = 118.8°$ [Ste71] (Figure 2-8). Although Hoppe [Hop59] initially reported that $LiYO_2$ had a tetragonal structure, later work by Gondrand [Wai67] and Hoppe [Ste71] showed that even low levels of impurity could stabilize the higher order structure. The structure of the pure crystal is monoclinic up to at least 1100°C, as are most compounds of the type $LiREO_2$ (RE signifies rare earth), and all belong to the same space group ($P2_1/c$). The conductivity of $LiYO_2$ was reported to be 3×10^{-3} S/cm at 400°C in the monoclinic form whereas the tetragonal form had a conductivity 1–2 orders of magnitude lower [Zou93].

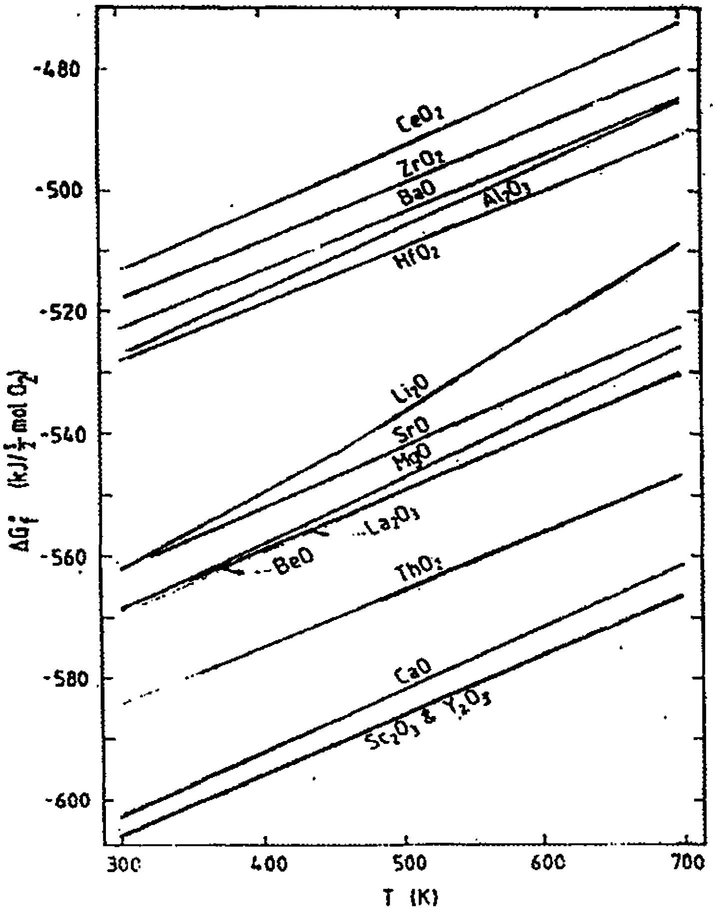

Figure 2-7. Gibbs energy of formation of binary oxides, normalized to the consumption of one half mole of molecular oxygen, as a function of temperature. Binary phases shown below Li_2O are thermodynamically stable against Li.

Faucher et al. [Fau98] found that there are wide corridors made of two parallel and adjacent Li-O rows along the [100] direction. Similar rows occur in the perpendicular [010] direction. It is not understood why these corridors are so wide (the mean vertical Li-O distance is 3.06Å. However, they can explain the hydration process since hydrogen diffuses along the wide corridors. Similarly, Li ion conductivity could be facilitated by diffusion of Li through these corridors.

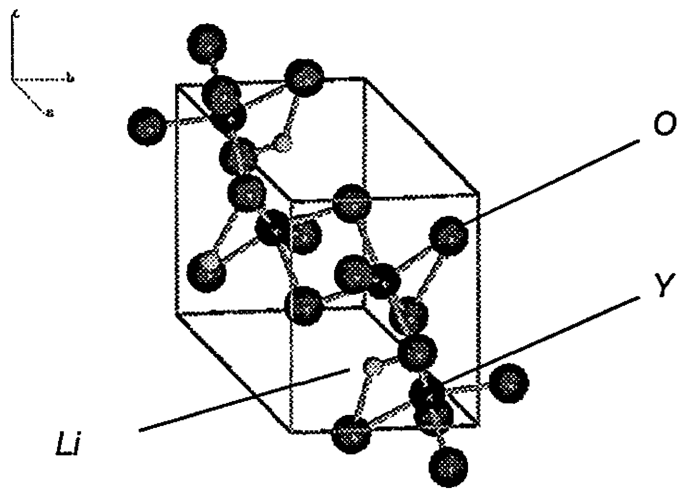

Figure 2-8. Crystal structure of $LiYO_2$

$LiYO_2$ is the only phase in the binary Li_2O and Y_2O_3. The $LiYO_2$-Y_2O_3 phase diagram [Bon78] shows the melting point of lithium yttrate at approximately 1880°C and a eutectic transformation at 1830±2°C (Figure 2-9).

Pure $LiYO_2$ shows conductivity at high temperature comparable to lithium β-alumina. At 500°C, the conductivity of $LiYO_2$ is 1.2×10^{-2} S/cm [Zou93]. In this case, conduction is probably by Li vacancies which could be introduced by evaporation at high temperature and substitution by yttrium according to $Y^{3+}\rightarrow Y_{Li}'' + 2\,\square_{Li}'$. The monoclinic structure, as was mentioned, has wide corridors that could facilitate mobility of lithium ions [Fau98] and explain the high ionic conductivity of $LiYO_2$.

Although Hellstrom and Van Gool [Hel80] found that $LiYO_2$ may partly decompose when exposed to air even at room temperature, it is stable against pure Li. The problem of

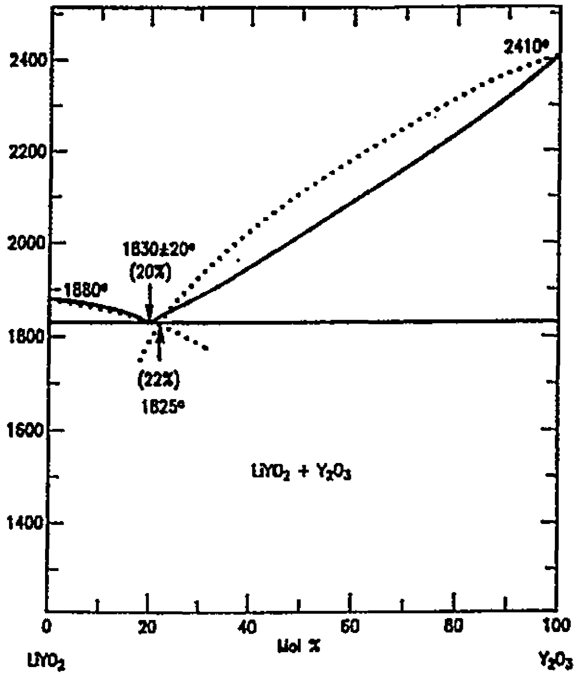

Figure 2-9. Phase diagram of $LiYO_2$-Y_2O_3[Bon78]

hydrolysis or decomposition can be avoided by working in an environment that excludes CO_2 and moisture. The only report of fabrication of a $LiYO_2$ cell was by Yamarte [Yam00]. The thermodynamic properties of lithium yttrate are not known.

2.5.3. Selection of Cell Materials Compatible with Liquid Lithium

The cell must be impervious to gas leakage (hermetically sealed) but maintain sufficient ionic conductivity to allow coulometric titration of lithium. The lid material must be an electrical insulator, non-reactive with lithium, and strong enough to support the load of mechanical clamping needed to close the cell. Furthermore, the thermal expansion coefficient must match that of $LiYO_2$.

The requirement of high electrical resistance excludes carbides and borides. Accordingly, the candidate ceramics selected for initial testing were limited to highly stable oxides along with one nitride. Based on their comparisons of the free energy of formation of Li_2O with candidate single-cation oxides, only BeO, Y_2O_3 and MgO are predicted to be compatible with a pure liquid lithium environment at 400°C [Lau92]. (Although UO_2 and ThO_2 also have more negative free energies than Li_2O, they were not considered here for obvious reason). In addition there are at least three families of mixed metal oxides incorporating lithium whose free energy of formation (per gram atom of oxygen) is more negative than or approximates that of Li_2O. The free energies of three such oxides, containing aluminum, zirconium, and titanium, respectively, are shown in Figure 2-10.

Li_2ZrO_3 and Li_5AlO_4 appear particularly promising based on free energy comparisons with Li_2O, however, both suffer the disadvantage of being hygroscopic. In the case of nitride ceramics, Singh's analysis [Sin76] showed Si_3N_4, BN, and AlN to be potentially compatible with lithium, based on the criterion that they had free energies of formation more negative than Li_3N.

Another concern in selecting candidate oxides is related to the uniquely small size of the Li^+ ion, which allows it to find accommodation between crystallographic planes or other interstices in many crystalline substances. This phenomenon, called intercalation, causes a

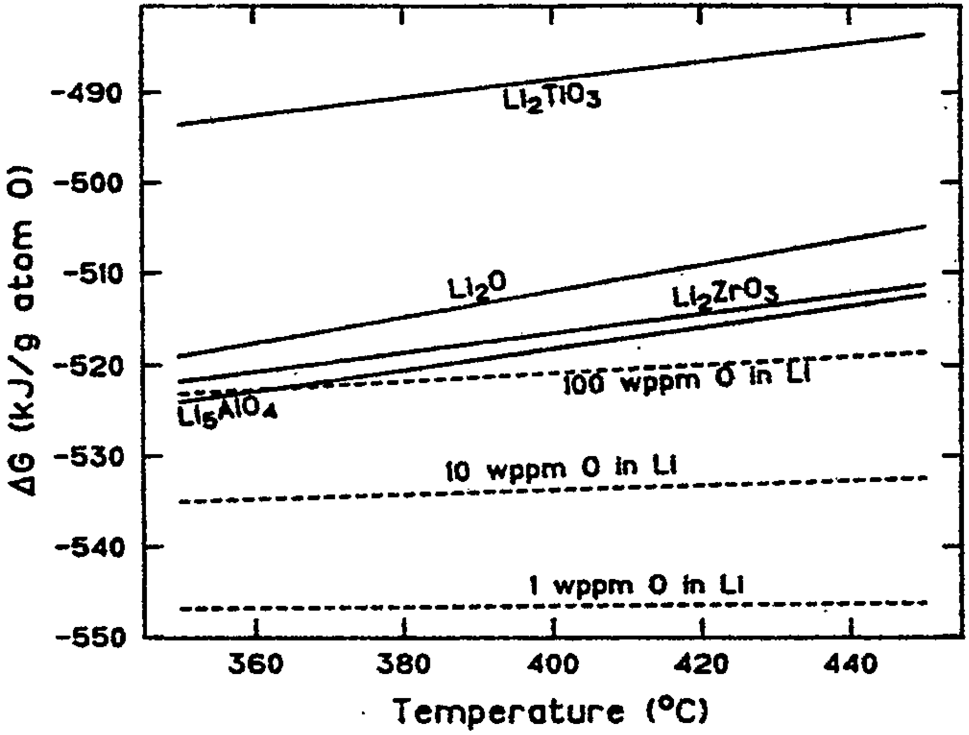

Figure 2-10. The standard free energies of formation of Li-metal-oxide compared with Li_2O vs. temperature.

significant change in the specific volume of the affected compound and can also radically decrease the electrical resistivity of the compound. For example, lithium intercalation compounds are being developed as electrodes in lithium batteries.

A third problem relates to ceramic manufacturing and involves additives. On the one hand, minor constituents added to enhance sinterability and, on the other, the extent of interconnected porosity following sintering with the additive adversely affects the compatibility of many oxide ceramics with lithium, and connected porosity backfilled with lithium will reduce the electrical resistance of even the most chemically compatible compounds.

From these thermochemical considerations as well as reviews of previous test results for ceramics exposed to liquid lithium, ceramics based on MgO, BeO, Y_2O_3, and AlN were the primary candidate materials identified for compatibility with lithium. Y_2O_3 was selected as the material for the cell lid by Yamarte in a previous study [Yam00] and MgO was added as a sintering aid.

2.5.4. Choice of the Lid Material

The thermal expansion coefficients of Y_2O_3 and MgO are reported as 9.3×10^{-6} and 13.5×10^{-6}/K respectively [Sam82], compared to our measured value for $LiYO_2$ of 11.8×10^{-6}/K. Yamarte found that neither of the two simple oxides were suitable for the lid [Yam00]. Poor bonding was obtained between MgO lids and the $LiYO_2$ tubes, possibly due to the thermal expansion mismatch. The Y_2O_3 lids sintered at 1600°C were brittle and broke under pressure during tightening of the cell holder. The same problem occurred with $LiYO_2$ or $LiAlO_2$. Yamarte also tried Al_2O_3 and YAG which had high strength but reacted with molten lithium. After testing MgO as a sintering aid for Y_2O_3 in amounts of 5 to 15 wt%, he found that the strength improved with MgO addition up to 12.5 wt% which was consequently selected as the lid composition.

2.6. Fabrication of the Solid State Electrochemical Cell

The prerequisite to a successful experiment with the EMF technique is to build a practical cell. A slip casting procedure which was outlined by Rivier and Pelton [Riv78] was used to manufacture green tubes in the laboratory. Subsequent steps include sintering, joining, testing and assembly of a galvanic cell. For the $LiYO_2$ tube the most difficult process was sintering and joining.

A common characteristic of sintering is a reduction in surface area with concomitant compact strengthening. This occurs through the formation of interparticle bonds brought about by atomic motion at the sintering temperature. Generally sintering can be categorized into two major types, solid state sintering and liquid phase sintering.

Solid state sintering of single component materials is the best understood form of sintering. Even for this case, there are several steps through which the powder progresses as it is heated. Amorphous materials sinter by viscous flow and crystalline materials sinter by diffusion, so the paths along which material moves, and the relationship between the rate of transport and the driving force, are quite different, depending on the microstructure [Ger85].

Liquid state sintering also greatly depends on the microstructure of materials, and in the usual case, the liquid wets the solid. Consequently, the wetting liquid acts on the solid particles to eliminate porosity and reduce interfacial energy.

2.6.1. Liquid Phase Sintering

The classic liquid phase sintering system densifies in three overlapping stages [Ger85]. Initially, the mixed powders are heated to a temperature where a liquid forms. With liquid formation there is rapid initial densification due to the capillary force exerted by the wetting liquid on the solid particles, The elimination of porosity occurs as the system minimizes its surface energy. During rearrangement, the compact responds as a viscous solid to the capillary action. The elimination of porosity increases the compact viscosity and as a consequence the densification rate continuously decreases. The amount of densification attained by rearrangement is dependent on the amount of liquid, particle size, and solubility of the solid in the liquid. Usually finer particles give better rearrangement. Full density (zero porosity) is possible by rearrangement if enough liquid is formed.

As densification by rearrangement slows, solubility and diffusivity effects become dominant. This second stage of classic liquid phase sintering is termed solution-reprecipitation. A general attribute of solution-reprecipitation processes is microstructural coarsening. The coarsening is due to a distribution in grain sizes. The solubility of a grain in its surrounding liquid varies inversely with the grain size; small grains have a higher solubility than coarse grains. The difference in solubilities establishes a concentration gradient in the liquid. Material is transported from the small grains to the large grains by diffusion. The process is termed coarsening or Ostwald ripening. The net result is a progressive growth of the larger grains, giving fewer grains with a wider spacing. Solution-reprecipitation not only contributes to grain coarsening, but also to densification.

The grain shape can be altered by diffusion to allow tighter packing of the grains. This process of grain shape accommodation leads to pore elimination.

The last stage of classic liquid phase sintering is referred to as solid state controlled sintering. Densification is slow in this stage because of the existence of a solid skeleton. Processes dominant in the final stage are also active throughout the entire liquid phase sintering cycle; however, because of the slow nature, solid state sintering is not of significance until late in the sintering cycle. The rigidity of the solid skeleton inhibits further rearrangement, although microstructural coarsening continues by diffusion. The residual pores will enlarge if they contain an entrapped gas, giving compact swelling. During pore growth the pressure in the pores decreases. Besides these pore changes, the grain contacts allow solid state sintering. The diffusion events leading to contact growth between solid grains can be by solution-reprecipitation, coalescence of grains, or solid state diffusion. In general, properties of most liquid phase sintering materials are degraded by prolonged final stage sintering. Hence short sintering times are typically preferred in practice.

These three stages of classic (persistent) liquid phase sintering are summarized in Figure 2-11 in terms of the key microstructural changes.

2.6.2. Transient Liquid Phase Sintering

An interesting variant to traditional liquid phase sintering involves a transient liquid which solidifies by diffusional homogenization during sintering [Ger85]. The transient liquid

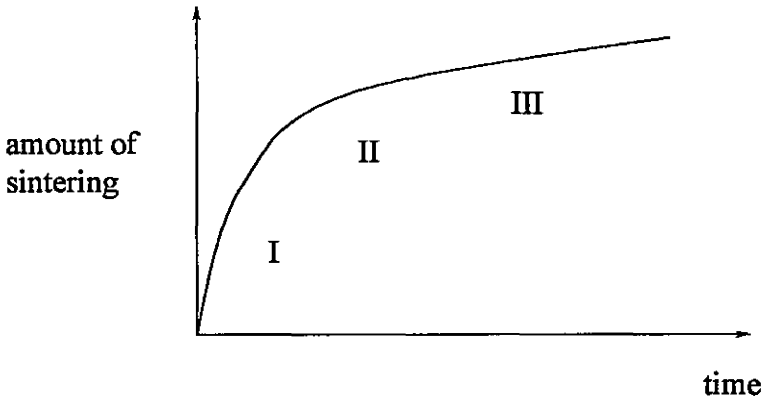

I. Rearrangement- melt flow and penetration
repacking, rapid densification or swelling, particle sliding.
II Solution-Reprecipition-diffusion control densification
shape accommodation, grain growth, neck formation.
III Solid State-rigid structure
neck growth, grain growth, coalescence, pore coarsening.

Figure 2-11. Three stages of classic liquid phase sintering [Ger85]

forms between mixed ingredients during heating to the sintering temperature. Figure 2-12 presents the phase diagrams of two sample systems which could be processed using a transient liquid. The solid does not change crystal structure due to alloying with the liquid.

For the first case shown in Figure 2-12, the liquid forms from eutectic reaction between the mixed constituents. Alternatively for the second case the liquid forms from the mixture of A (additive) and B (base) when the additive melts. Unlike persistent liquid phase sintering, the liquid has a high solubility in the solid and disappears with sintering time. However, because the liquid content depends on several processing parameters, transient liquid phase sintering is highly sensitive to processing conditions.

The requirements for transient liquid phase sintering include mutual inter-solubility between the components with the final composition existing within a single phase region. Furthermore, the liquid must wet the solid and give a high diffusion rate for the solid. Under these conditions rapid sintering is anticipated when the liquid forms. Generally, the observed steps are as follows [Hod76, Ger85, Lap83]:

1) swelling by interdiffusion prior to melt formation (Kirkendall porosity),
2) melt formation,
3) spreading of the melt and generation of pores at additive particle sites,
4) melt penetration along solid-solid contacts,

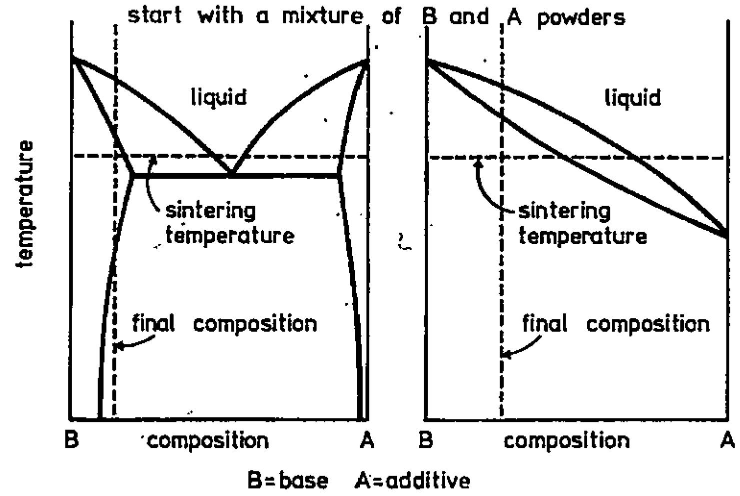

Figure 2-12. Two kinds of phase equilibria which could be used for transient liquid sintering

5) rearrangement of the solid grains,

6) solution-reprecipitation induced densification,

7) diffusional homogenization,

8) loss of melt, and

9) formation of a rigid solid structure.

The actual steps depend on several process variables, including particle size, amount of additive, heating rate, and maximum temperature. Swelling is common during heating because of the required solubility of additive in the base, especially if intermediate compounds form between the constituents [Ger85]. The densification associated with transient liquid phase sintering depends on the amount of liquid formed and the length of time the liquid exists. Too much liquid can generate large pores due to spreading and penetration of the melt away from the additive particle sites. Typically, the liquid lasts for only a few minutes, thus pore refilling does not occur and large pores result. However, if the liquid persists, then densification will follow.

Heating rate is important to transient liquid phase sintering. During heating, diffusional homogenization leads to pore formation by a Kirkendall effect. The amount of swelling increases with the amount of interdiffusion; thus, more swelling is seen with slower heating rates. Furthermore, diffusional homogenization reduces the amount of liquid formed at the eutectic temperature and the degree of sintering. After reaching the sintering temperature, the amount of liquid and the length of time the liquid exists determine the net shrinkage. The amount of liquid depends on the degree of homogenization and the initial additive concentration.

Often the swelling reaction is most intense just prior to the liquid formation temperature. The amount of swelling during heating depends on the heating rate and additive content, which control the degree of interdiffusion.

The amount of densification after liquid formation depends on how much liquid was formed and the length of time the liquid persists. In turn the heating rate, additive content, and particle size are dominant with respect to densification [Puk84, Pau84, Kis82]. Generally faster heating rates allow use of smaller particle sizes and lower additive contents, and give superior sintered properties.

As expected with a complex processing technique, there are several potential problem areas. Pore formation during heating is a major difficulty. These pores can become stabilized and remain during the balance of the sintering cycle. In some cases, the swelling process associated with the-high additive solubility in the base can generate stresses and crack the compact. Overall, transient liquid phase sintering is more sensitive to process variables than other forms of sintering. Consequently, optimal sintering requires balance between the processing parameters. Only in a few studies have these interrelations been developed and processing optimized. Successful applications of transient liquid phase sintering depend on striking such balances for optimal sintered properties.

A novel combination of transient liquid phase sintering and infiltration processes has been described by Langford and Cunningham [Ger85] as diffusional solidification. In this case, packed powders are heated prior to infiltration with a liquid. The overall alloy composition is selected to be in a single phase solid region of the phase diagram at the infiltration temperature. Thus, the liquid is rich in solute compared to the solid. After infiltration, the solute diffuses into the solid to homogenize the system and causes the liquid to solidify. One advantage of this approach is that it avoids the gross porosity observed in some cases of transient liquid phase sintering.

2.6.3. Reactive Sintering

In 1982 Coble developed the model for "reactive sintering" [Cob81]. The model described chemical reactions that occur between solids and solids, solids and liquids, or solids and gases, for which several simple geometric diffusion fields have been analyzed; for these the shape/configuration/geometry is presumed to be unchanged as the reaction proceeds.

For some reacting systems the initial geometry is not maintained. The changes in porosity and pore shape alter the permeation behavior, thereby altering the kinetics. The area of interest here is where these two fields overlap. The principal problem is to understand what governs or affects the microstructure changes that take place during reactive sintering that are not predicted by the sintering models or by combinations of the sintering and reaction models jointly.

The chemical driving force for the reaction can be much larger than the driving force from normal sintering processes [Cob81]. Reactive sintering is similar to transient liquid phase sintering. It is characterized by a large heat liberation due to a reaction between the constituent powders [Cob82]. Rapid sintering results from the formation of a liquid (possibly due to reactive self-heating from an exothermic reaction) between the constituent powders. Figure 2-13 illustrates one type of phase diagram anticipated for reactive sintering. In this case the process starts with pure components A and B to form the compound AB. By appropriate temperature and composition selection, a liquid is formed during the reaction.

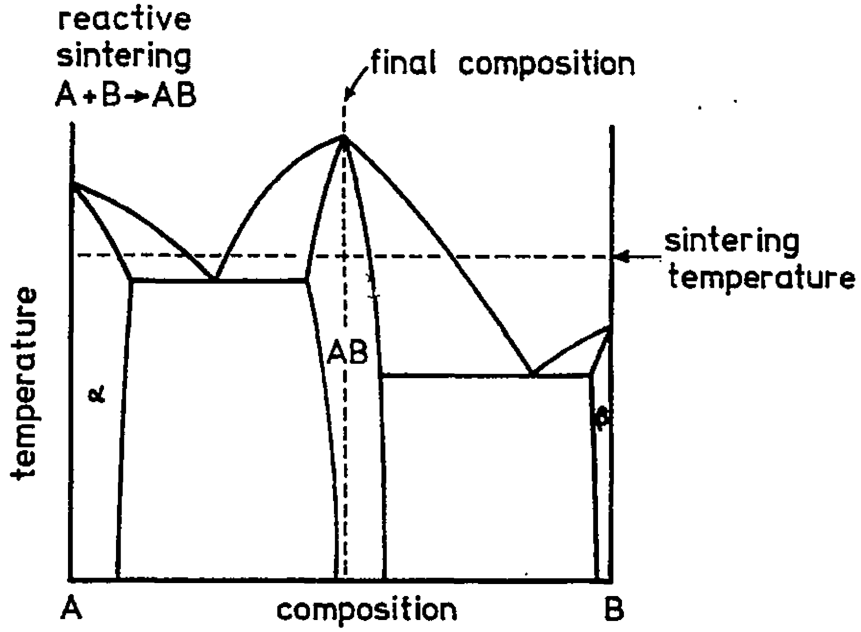

Figure 2-13. Phase diagram showing potential for reaction sintering

An example of reactive sintering is found in the synthesis of compounds like titanium carbide or titanium nitride from the constituent powders. In the study by Quinn and Kohlstedt [Qui89], substoichiometric TiC was reacted with Ti powder to form TiC. A eutectic liquid formed during the sintering treatment which consumed the excess titanium. During the reaction, grain growth and densification were observed due to rapid diffusion rates in the liquid.

However, in spite of helpful chemical reactions, pore formation is common in reactive sintering systems. Densification is rapid once the liquid forms and control of the liquid duration depends on control of the temperature, particle, size, and green density.

Chapter 3. EXPERIMENTAL METHOD

3. 1. Fabrication of the EMF Cell

3.1.1. $LiYO_2$ Prepared by High Temperature Solid State Reaction

$LiYO_2$ was synthesized by solid state reaction of $LiNO_3$ (Caledon Laboratories Ltd.) or Li_2CO_3 (BDH Laboratory Supplies) and Y_2O_3 (Pacific Industrial Development Corp.). $LiYO_2$ is the only compound in the binary Li_2O - Y_2O_3 system and was formed according to the reactions below.

$$2LiNO_3 + Y_2O_3 \xrightarrow{900^\circ C} 2LiYO_2 + N_2O_5 \qquad \textbf{Eq. 3-1}$$

or

$$Li_2CO_3 + Y_2O_3 \xrightarrow{1250^\circ C} 2LiYO_2 + CO_2 \qquad \textbf{Eq. 3-2}$$

The starting chemicals were weighed and mixed in an alumina mortar. The reactants were pressed into pellets and calcined in an alumina crucible. The temperature was raised to 725°C, held for several hours, followed by heating to the reaction temperature (1250°C), which was held for 15 h (Figure 3-1). The final product was analyzed by XRD to assure phase-pure $LiYO_2$.

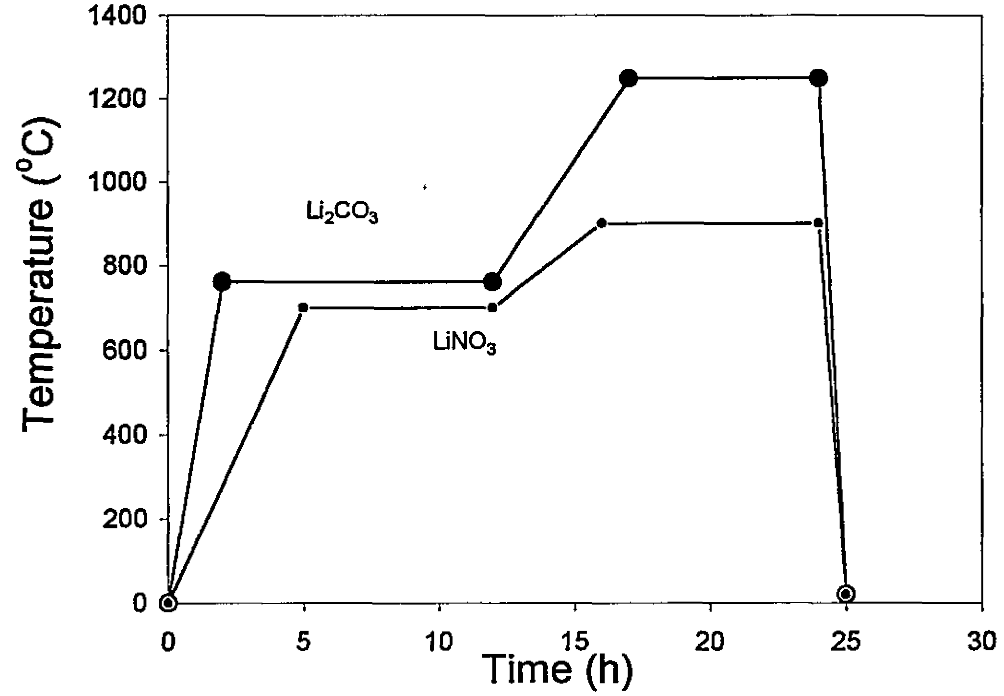

Figure 3-1. Solid state processing of $LiYO_2$ powder

3.1.2. Tube Fabrication

A slip casting technique developed by Rivier and Pelton [Riv78] was adopted for making electrolyte tubes in the present work.

$LiYO_2$ powder was ground and then vibromilled with alumina balls in a nalgene bottle for 48 h. Particle size was reduced to less than 5 µm to obtain a stable suspension and to minimize the porosity of the finished product.

Grinding for a longer period did not appreciably decrease the mean diameter but also would cause problems of contamination. 100 mL absolute ethanol was used to form a suspension with 72 g $LiYO_2$ powder.

The $LiYO_2$ suspension was cast in powder molds made by compacting dried α-alumina powder in a beaker around a test tube mandrel. The mold was filled with slurry and held for approximately 1 min to deposit the desired wall thickness before the excess suspension was poured out.

The casting was allowed to dry for 24 h, then removed from the mold by scraping and brushing away the powder. The unsintered tubes were 60% of theoretical density and 1

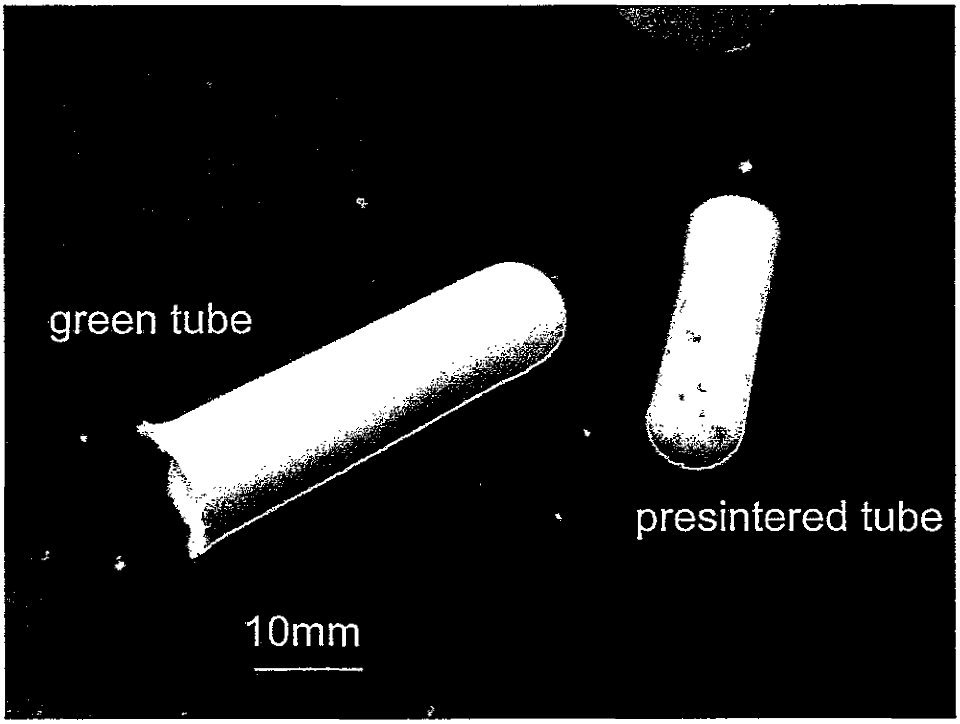

Figure 3-2. $LiYO_2$ tube made by slip casting

cm in diameter with a wall thickness of 1 mm. The green tubes (Figure 3-2) were presintered in an alumina crucible buried in coarse $LiYO_2$ powder to minimize lithium losses at 1250°C for a half hour.

The density after pre-sintering was measured by the Archimedes method in ethanol to be about 80% of theoretical, that is, about 3 g/cm^3 on average.

The presintered tubes were cut with a diamond blade to 3 cm in length. Kerosene was used as a lubricating medium.

Lids were fabricated by isostatically pressing and sintering disks of 25 mm diameter.

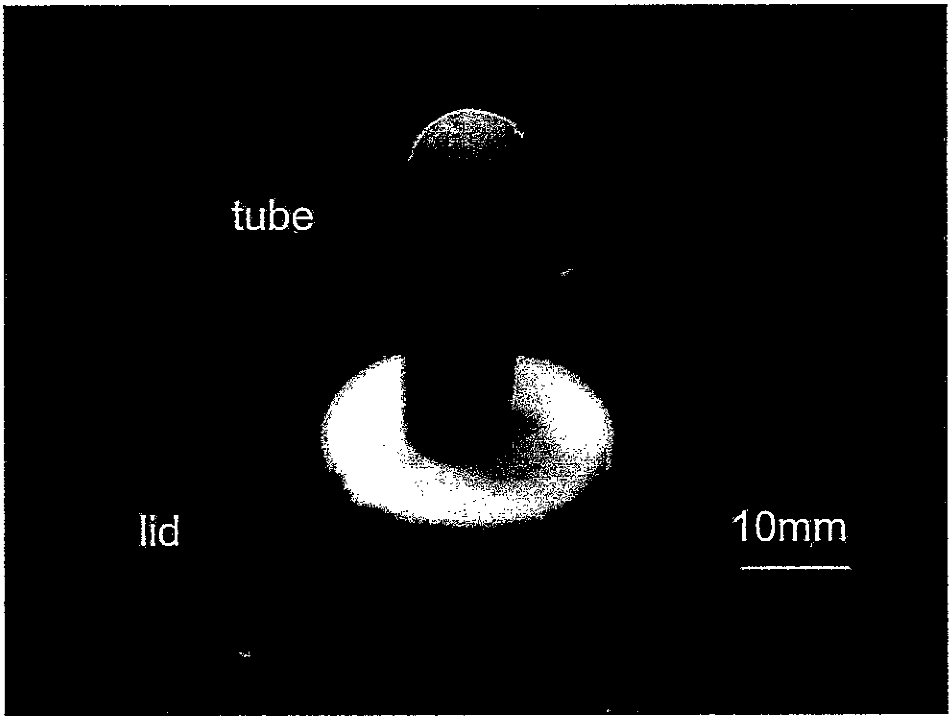

Figure 3-3. The tube and lid prepared for joining

A tapered bore was machined in the centre of the lid that allowed loading the electrode and then mechanically sealing the cell with a Ta cone. Green lids were sintered at 1690°C. Sintered lids can be used many times [Yam00].

The tube was set on the lid as shown in Figure 3-3 and loaded into a SiC furnace preheated to 1300°C. The lid/tube couple could be viewed during the bonding process through a view port in the door. When the gap between the tube and lid, observed as a dark line, closed completely the furnace was shut off. This indicated that joining had occurred and was accompanied by a sintering process from the joint to the top of tube.

The density of sintered tubes was about 98% of theoretical density which is 3.51g/ cm^3. After joining the tubes were leak tested by a Veeco helium leak detector and those that held at least 10^{-4} mbar vacuum were selected for cells.

3. 2. EMF Measurement

All the measurements were carried out in an inert atmosphere (argon) glove box. The composition of the Li-Al alloy was varied with high precision by coulometric titration. Composition changes of less than 1 ppm can be achieved by use of a galvanostat/coulometer. There is no need to reopen the cell until the experiment is complete.

EMF measurements were taken between working and reference half-cells that were electrically connected by means of a molten metal bath. The half-cells were constructed by adding electrode materials to the tube-lid assembly via the bore.

The emf data were then used to derive the phase diagram and the various thermodynamic properties of the liquid and solid phases.

3.2.1. Filling and Assembling

High purity metals were used at the electrodes and precautions were taken to remove surface oxides when necessary. Li (99.99%) metal strapping, Al (99.99%) in 2 mm dia wire or Sn granules (99.95%) were loaded into the cells as electrodes. The cell was closed with a Ta cone tapered to fit the countersink in the lid (Figure 3-4). A Ta wire lead completed the circuit. The Ta cone was clamped to the lid by a cell holder machined from a Zr-2.5% Nb alloy supplied by Atomic Energy of Canada Ltd.

Figure 3-5 shows the schematic of the EMF apparatus. The main components were the $LiYO_2$ tube which served as the electrolyte, a Y_2O_3 lid which served as the insulating electrical feed-through and, a stainless steel cap and inert wire lead. The apparatus operated with three electrodes – a counter electrode (CE), a reference electrode (RE) and a working electrode (WE). The CE served two purposes: 1) it was a source of Li metal to be titrated into the cell, and 2) it provided the electrical contact between working and reference electrodes. The CE consisted of Sn and a few percent Li. Bulk tin rods of commercial purity were used for the molten Li-Sn bath. The minimum measuring temperature was limited by the melting temperature of the CE which was 230°C.

The cells were loaded and operated inside an Ar glovebox. The concentration cell

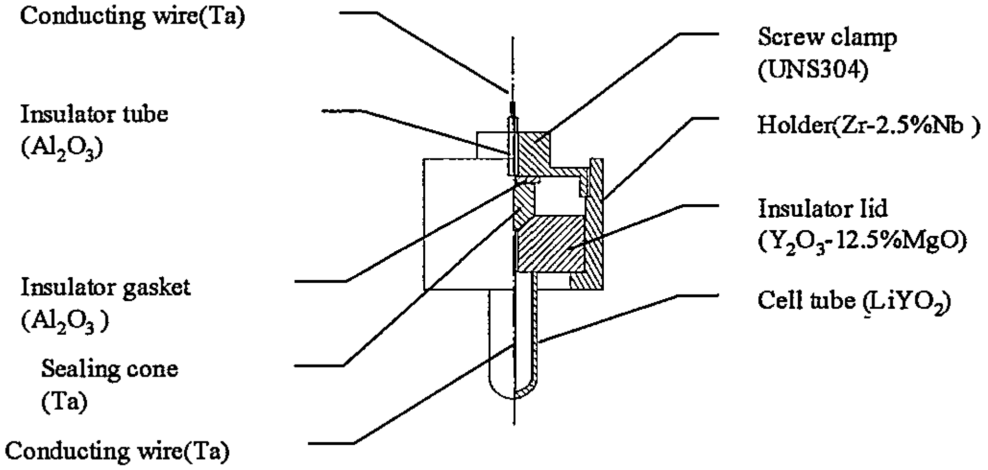

Figure 3-4. Final cell assembly with a Ta cone tapered to fit the countersink in the lid. A Ta lead completed the circuit. The Ta cone was clamped to the lid by a cell holder to provide a hermetic seal.

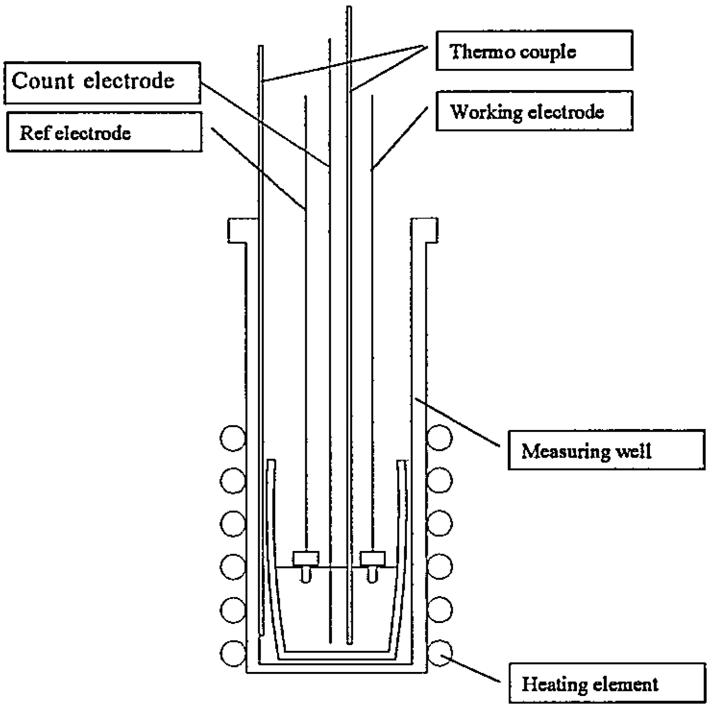

Figure 3-5. Schematic of measurement apparatus

with a $LiYO_2$ electrolyte can be represented schematically by:

(WE) **Li (alloy) | $LiYO_2$ | Li (pure)** (RE) **Cell 1**

or,

(WE) **Li (alloy 1) | $LiYO_2$ | Li (alloy 2)** (RE) **Cell 2**

The composition of the Li alloy in the working electrode could be varied by coulometric titration. Li-Sn alloy was used as the reference electrode due to its low melting point and low vapor pressure.

At the beginning of the experimental operation, the Li-Sn reference electrode was calibrated against pure Li. The reason is that pure Li is more volatile and a pure Li electrode is more prone to failure. The reference electrode is recalibrated at the end of the measurement to check for drift.

The RE was a cell containing, as mentioned above, Sn and a small fraction of the Li. All EMF readings could then be reported with respect to the pure Li. The WE contained the base metal component of the Li-Al system to be tested.

The glovebox atmosphere was controlled by an MBraun 150B-G-1 inert gas system which is designed as a compact lab workstation (Figure 3-6). The residual oxygen does not exceed 1 ppm, and is monitored by a oxygen analyzer. The atmosphere is continually recirculated through a molecular sieve and copper catalyst to remove H_2O and O_2. To prevent the filter capacity from being totally exhausted, the gas purifier was regenerated periodically with forming gas (7% hydrogen balance nitrogen or argon). Ultra high purity grade argon

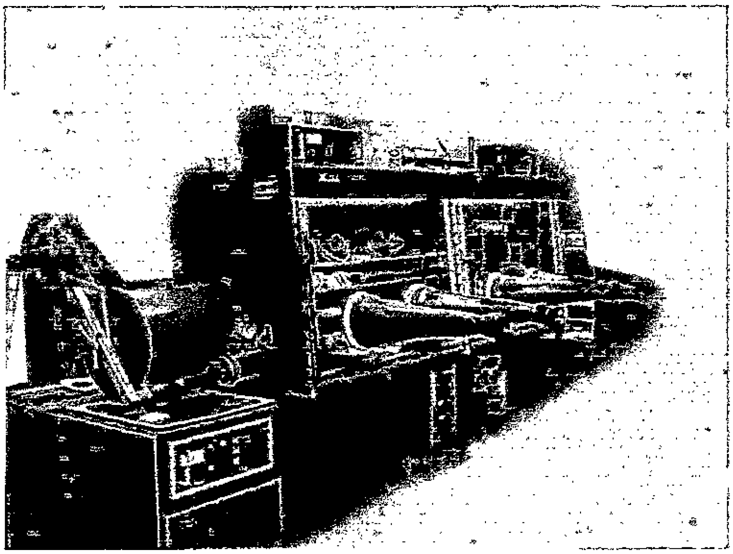

Figure 3-6. MBraun 150B-G-1 inert gas glove box

was used to supply the inert atmosphere.

3.2.2. Coulometric Titration

Li metal was added to the WE by coulometric titration. By applying a small potential (100-500 mV), Li ions were transported across the $LiYO_2$ membrane from the CE into the WE and since the transport number is essentially unity, one Faraday of charge (96484.6 Coulombs) was necessary to transfer one mole of Li metal. The circuit allowed current to be passed between the CE and WE, whereas in the open circuit position, the EMF between RE and WE was monitored on a digital voltmeter. The voltmeter was calibrated against a standard output voltage cell. The circuit had an internal resistance of 10^{14} Ω. Readings of RE versus WE and thermocouple EMF were continuously recorded on an ABB GOERZ SE430 chart recorder and simultaneously the analog signal was converted to a digital signal and recorded by a computer. The EMF versus temperature plot could be viewed on the screen directly. Thus both temperature and chemical potential could be tracked with considerable precision to ensure equilibrium. EMF data were checked for reproducibility by reversing the direction of titration or by thermal cycling.

The experiments were done with following sequence:

First, Li was titrated into the WE to a pre-set composition.

Next, the temperature was cycled several times at fixed composition to measure dE/dT.

Then the WE was titrated to another composition, and the measurements repeated.

3.2.3. Reading Data by Multimeter

EMF data were monitored by a HP34401A digital multimeter which is a high performance instrument capable of measuring resistance, DC and AC voltage and current, as well as frequency. In addition, it can be remotely programmed using the SCPI (Standard Commands for Programmable Instruments) language and read by computer via a General Purpose Interface Board port.

EMF is measured in volts by using a voltage amplifier and an analog-to-digital converter as schematically shown in Figure 3-7. A microprocessor further manipulates the data before displaying the results.

An ideal voltmeter has an infinite input resistance so that it will not draw any current from the circuit under testing. However, in reality, there is always a finite input resistance R_i, as shown in Figure 3-7. As a result, one has a voltage divider that will cause the voltage V_m one sees at the input of the voltmeter to be slightly different from the actual voltage V_S one wants to measure. The HP34401A has a relatively large input resistance of at least 10 MΩ (depending on the selected voltage range) so that the error will be small as long as $R_s << R_i$.

3.2.4. Data Transfer to Computer and Data Processing

The data acquired were transferred to a computer by the GPIB (General Purpose Interface Bus), also known as IEEE-488 or HPIB. It is defined completely in the IEEE standard 488.1-1987.

A computer program was redesigned from original software to record the data and to plot the graph of EMF versus temperature. The data recorded can then be processed by EXCEL or ORIGIN word processing software.

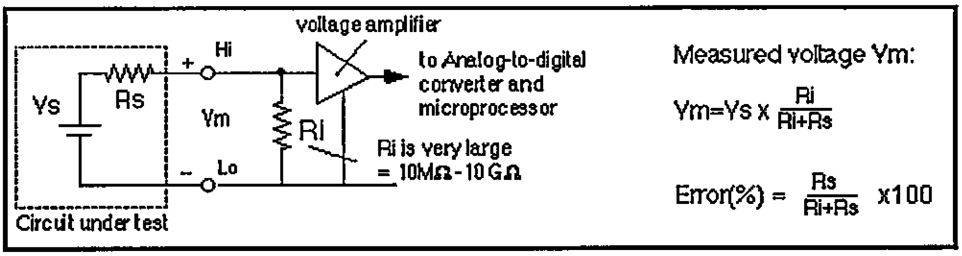

Figure 3-7. Schematic of the DMM as a DC voltage meter.

Chapter 4. RESULTS AND DISCUSSION

This thesis resulted in two major achievements. First, the mechanism of joining the $LiYO_2$ tube to the Y_2O_3-12.5% MgO lid was studied. The role of Li_2CO_3 in the sintering of $LiYO_2$ was revealed. Secondly, the thermodynamic properties of the Li-rich portion of Li-Al phase diagram, including the liquid phase, the α-solution region and the $\alpha+\beta$ two-phase region were investigated in the temperature range 370 to 790°C. The liquidus curve was determined from points on the EMF versus temperature plot.

4.1. Fabrication of Cells

$LiYO_2$ was used as the electrolyte in this study. Earlier work in this lab had tested sealants such as $LiYO_2$, Li_2SiO_3, LiF and Li_2CO_3 to join fully sintered lids and tubes [Yam00]. This approach met with persistent failure either because of incomplete sealing of the joint or because of an unexplained phenomenon of spontaneous cracking of the tube tip upon removing the cell from the furnace after joining.

4.1.1. Sintering and Joining Processing

The sintering process in this study was separated into two steps: presintering and final sintering with joining.

Figure 4-1 shows the microstructure of the green tube in which the particle sizes of

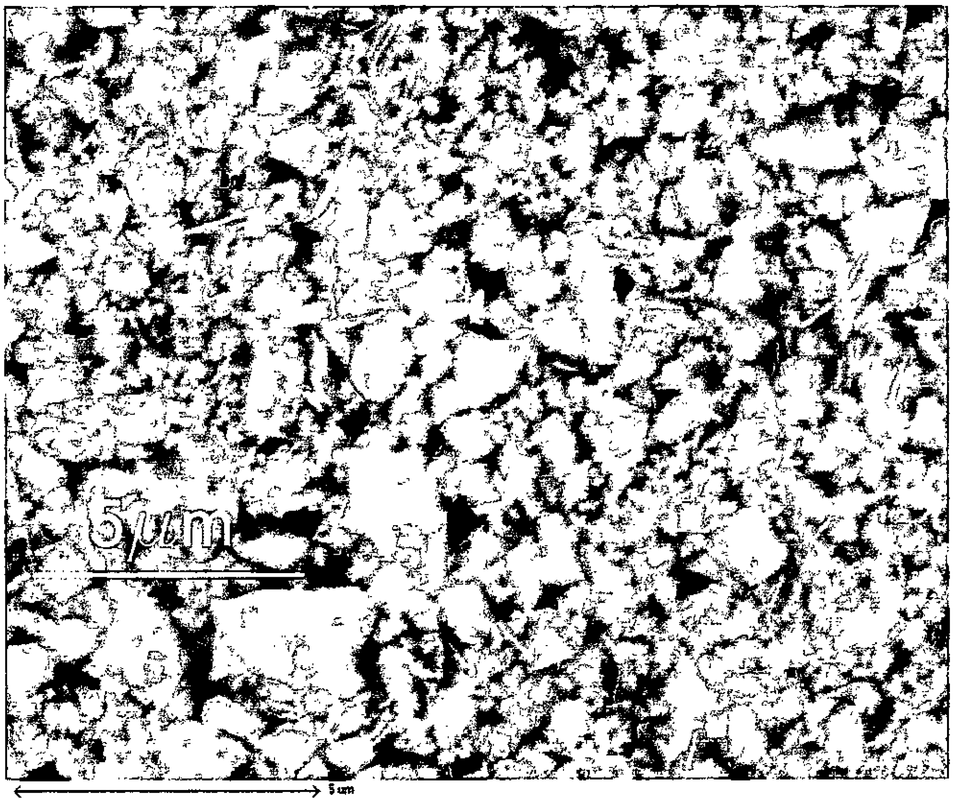

Figure 4-1. SEM image of the surface of a green tube shows the microstructure of $LiYO_2$

$LiYO_2$ crystal range from 1 to 6 μm. Green tubes were very fragile and for further processing, they were presintered at 1250°C. The microstructure of the presintered tube (Figure 4-2) showed evidence of liquid phase sintering. $LiYO_2$ grains were wetted by the liquid phase which was believed to be a Li_2CO_3 melt. A rearrangement of particles, but little densification occurred and pores developed at this time.

The presintered tube was cut to length, placed on the lid and set in the furnace for joining and final sintering. (The detailed process was described in chapter 3).

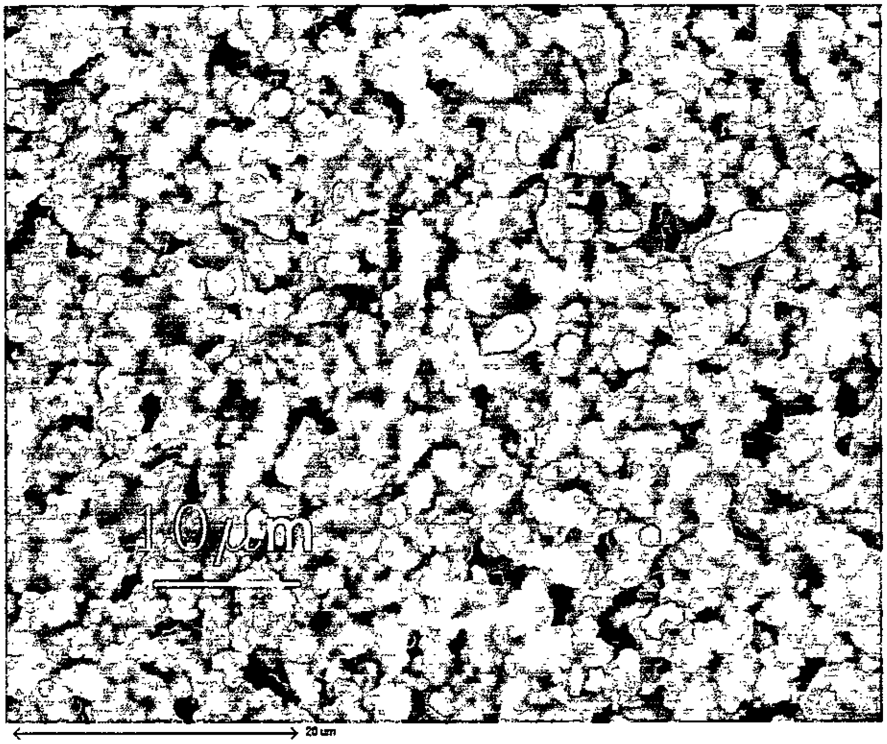

Figure 4-2. SEM image of the surface of the presintered tube shows wetting of the solid by the liquid phase but little densification.

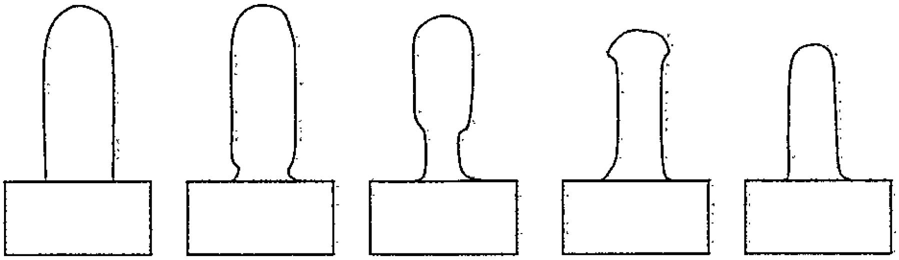

Figure 4-3. Shrinkage started at the bottom of the tube and propagated to the top when temperature reached 1325°C.

Figure 4-4. Microstructure of a fracture section of the $LiYO_2$ sintered tube showing high density

The furnace temperature was approximately 1325°C when joining occurred. No visible shrinkage of the tube occurred below 1200°C. Near 1325°C, shrinkage easily visible to the eye started at the bottom of the tube and propagated as a wave to the top in a span of 30 - 60 s (Figure 4-3). This procedure effectively densified the tube and joined it to the lid. The final microstructure of the tube showed full densification (Figure 4-4).

Infiltration was observed in the joint. Figure 4-5 shows the liquid spread away from the tube and penetrated the grain boundary of the Y_2O_3 lid, which led to the joining. The joint was normally found to be impervious by helium leak testing.

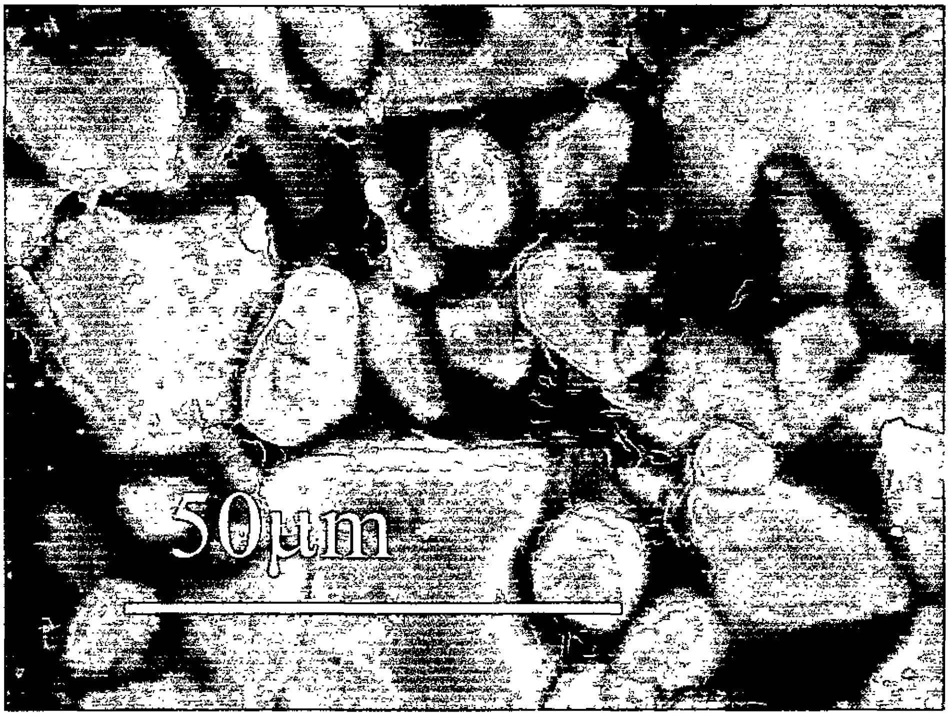

Figure 4-5. SEM image shows the infiltration on the surface of the Y_2O_3 lid near the joint

4.1.2. The Role of Li_2CO_3 in Joining and Sintering

The function of Li_2CO_3 in the sintering process was tested as follows. Tubes fabricated with different amounts of Li_2CO_3 from 0 to 10 wt.% were sintered and joined to the lids. The tube containing 3 wt.% Li_2CO_3 yielded a good seal and full densification under the process conditions described earlier. A larger amount of Li_2CO_3 resulted in cracking of the cell upon cooling, and less Li_2CO_3 did not yield a good seal.

$LiYO_2$ tubes with no Li_2CO_3 additive could not be used to make a cell. No significant strength was observed in the joint, although some reaction was evident. Densification oc-

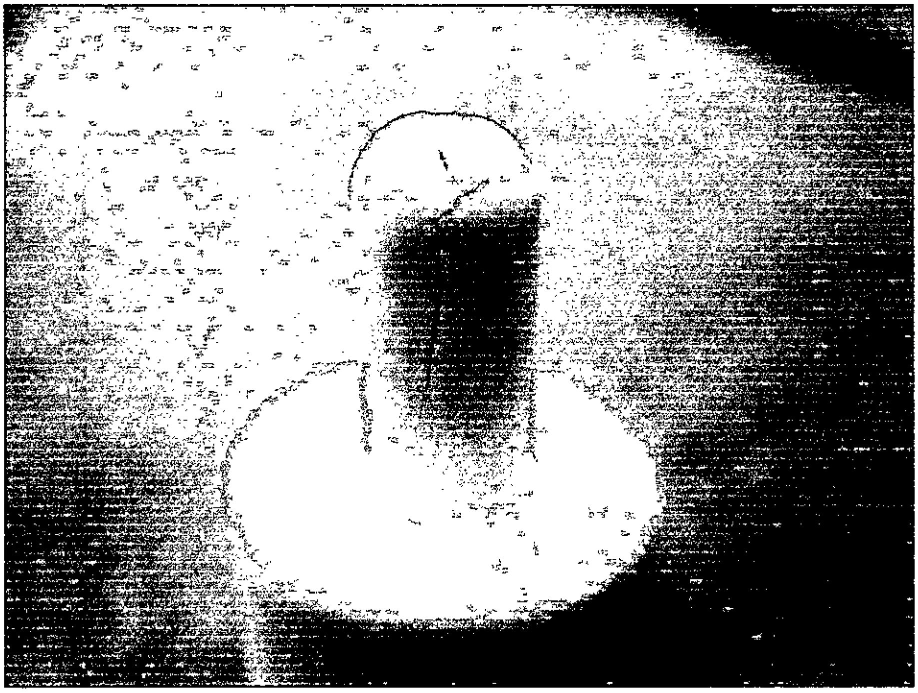

Figure 4-6. The sintered tube with no Li_2CO_3 additive spontaneously cracked within minutes when cooled and exposed to air

curred only when the tube was heated above 1500°C, and showed only incomplete solid phase sintering behavior. The tube spontaneously cracked within minutes of being exposed to air after cooling (Figure 4-6).

The presence of Li_2CO_3 is not detrimental for our application. Li_2CO_3 is known to have good electrolytic properties. Pure Li_2CO_3 melts at 723°C and decomposes at 1310°C. The mechanism of joining and sintering will be discussed in detail in section 4.1.3.

The optimum procedure was to add Li_2CO_3 to the $LiYO_2$ powder before slip casting. The furnace temperature and heating time were critical. Overheating resulted in collapse of

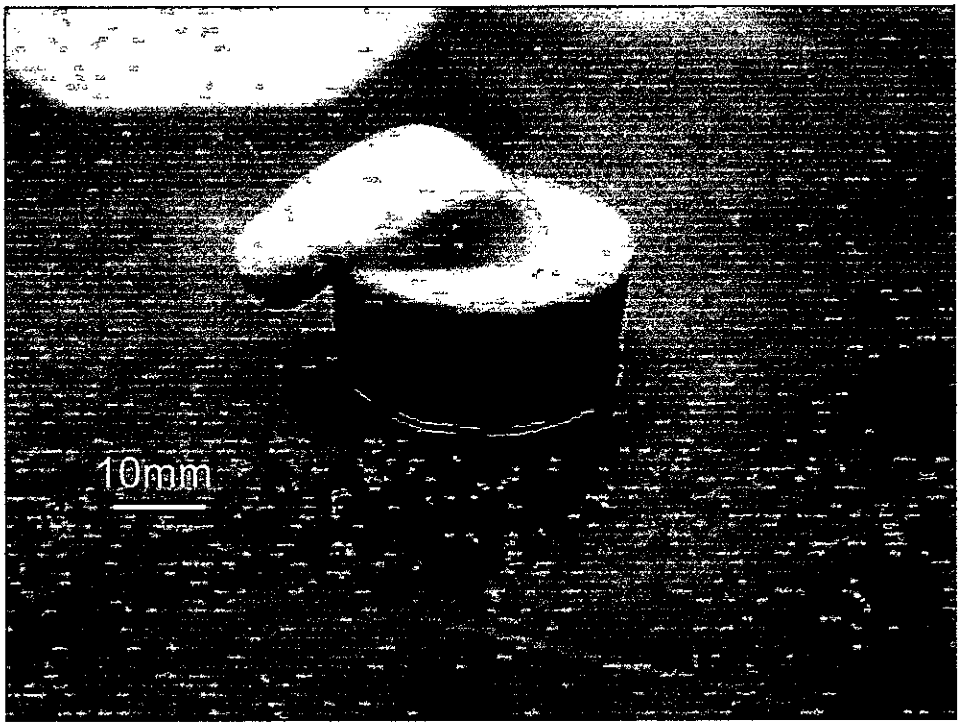

Figure 4-7. Overheating above 1325°C resulted in collapse of the tube but the joint remind intact.

the tube (Figure 4-7), although it may be noted that the tube-lid joint remained intact. Also, if the heating rate was too slow, we could not obtain a good seal since the Li_2CO_3 decomposed before bonding.

A second heating of the tube above 1300°C generally caused degradation. Figure 4-8 shows surface defects of a reheated tube, including bloating and cracking caused by decomposition of Li_2CO_3 at high temperature.

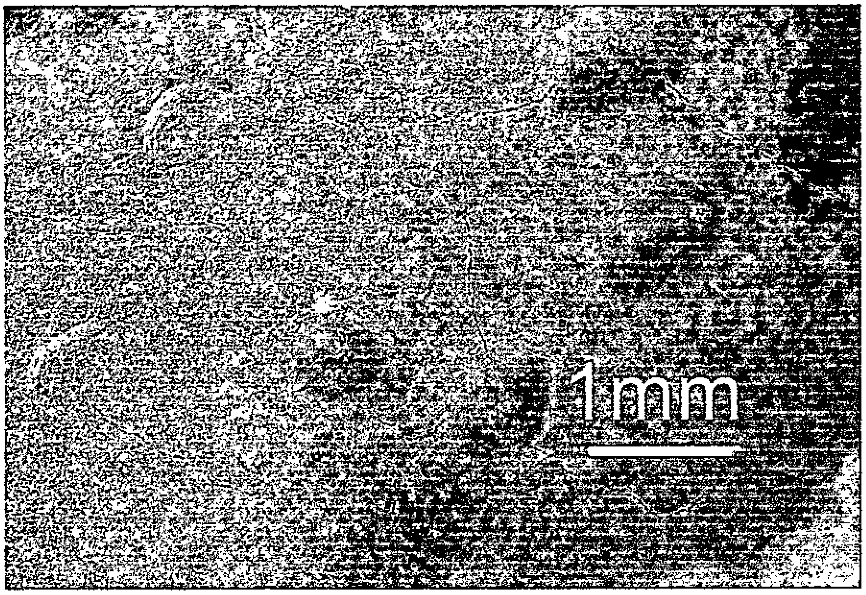

Figure 4-8. Bloating and cracking of tube surface after reheating tubes to 1300°C, caused by the decomposition of Li_2CO_3

4.1.3. Mechanism of the Joining and Sintering Process

Although the sintering processing employed in this study is different from that treated by the classical theory of liquid phase sintering, the fundamental considerations involved are similar.

From the Y_2O_3-rich portion of the phase diagram and crystallography data, we know that $LiYO_2$ is the only intermediate compound formed between Li_2O and Y_2O_3 (Figure 4-9). No phase equilibria are available for the Li_2O - $LiYO_2$ part of the diagram.

Based on DTA/TGA measurements of the powder used for slip casting, and by comparison with data from the Li_2O-Al_2O_3-CO_2 phase diagram, we may formulate a hypothesis on the reaction mechanism.

DTA of presintered tubes showed three peaks during heating from room temperature to 1500°C. In order to obtain clarification of the peaks, a control DTA experiment was performed, using a 1:1:0.2 mixture of $LiYO_2$, Y_2O_3 and Li_2CO_3.

The control sample was thermally cycled twice from room temperature to 1500°C. The DTA curve showed two endothermic peaks during the first heating (Figure 4-10), matching the analysis from the tube. No peaks appeared in the second run. The first peak corresponded to the melting of Li_2CO_3 at 733°C. A second event in the analysis began at 750°C and lasted until 950°C. It was accompanied by a large decrease in sample weight, as seen by TGA. This can be explained by the calcination of lithium carbonate (accompanied by loss of CO_2), followed by reaction of the liberated Li_2O with free Y_2O_3 to form $LiYO_2$. DTA shows that the latter exothermic reaction began near 920°C. The lack of peaks in the second run is attributed to the disappearance of Li_2CO_3 during the first DTA cycle.

The lid material has a large Y_2O_3 content. The tube is nominally $LiYO_2$ with 3 wt% Li_2CO_3 although we have observed that some of the $LiYO_2$ is converted to Li_2CO_3 or LiOH during preparation of the slip and presintering. The calcination temperature of Li_2CO_3 is very sensitive to the CO_2 pressure. Thus, at the usual pressure of $10^{-3.4}$ atm CO_2 in the atmosphere, decomposition begins shortly above the melting point (Figure 4-11). On the other hand, at a pressure of 0.5 atm, Li_2CO_3 remains a stable liquid above the usual ceramic processing temperatures used in this study. The slow heating of a DTA experiment represents the former condition; rapid firing as in the case of our sintering cycle parallels the latter,

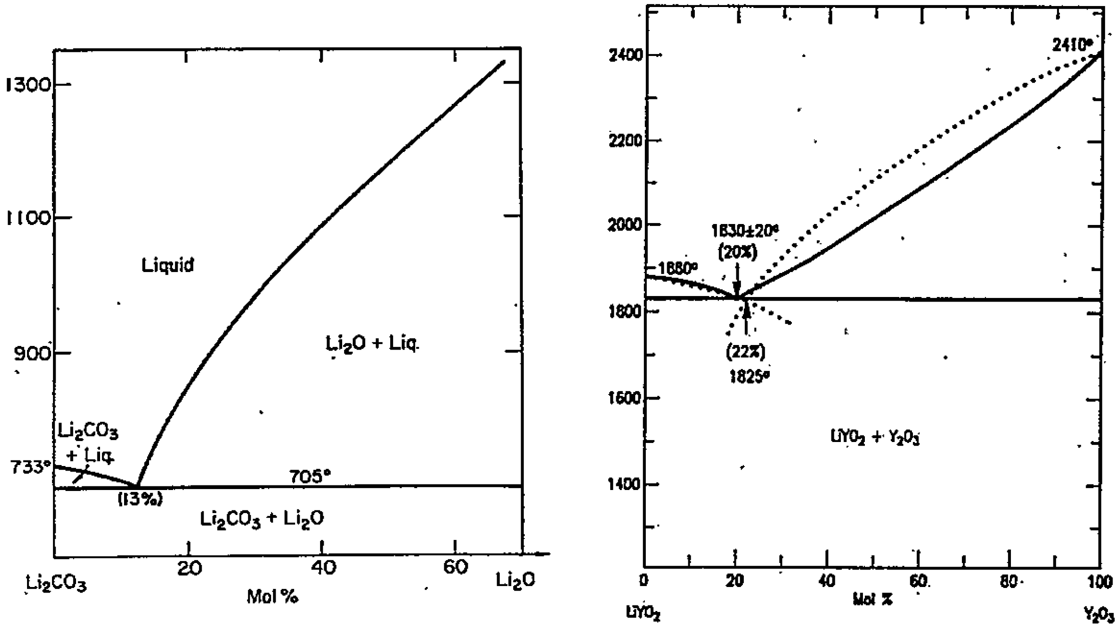

Figure 4-9. Phase diagram of Li_2CO_3-Li_2O and $LiYO_2$-Y_2O_3 system

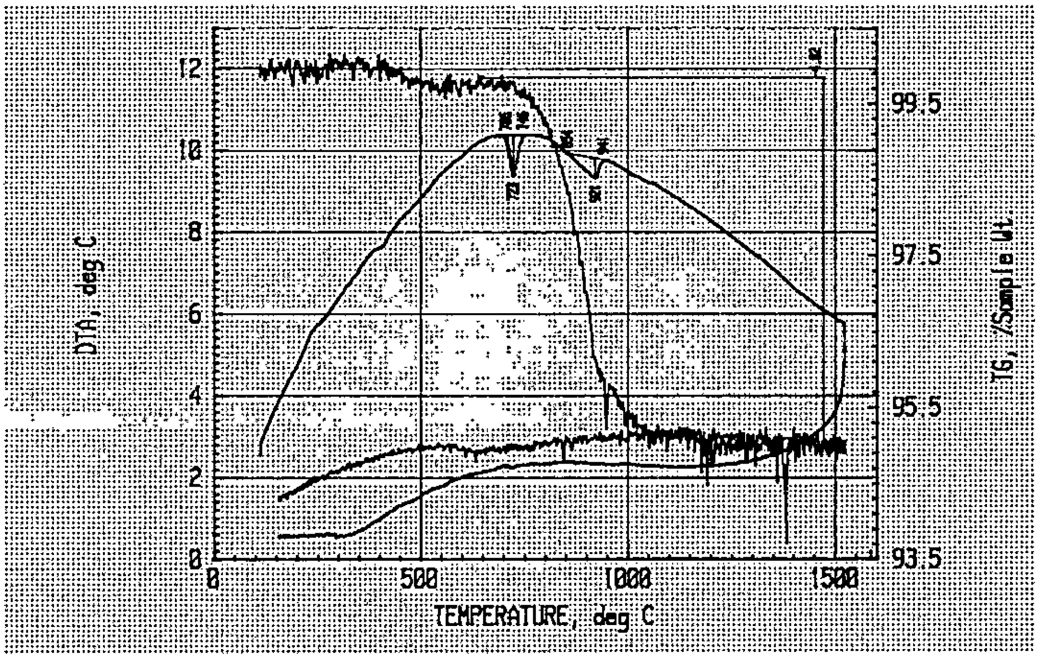

Figure 4-10. DTA and TG of mixing $LiYO_2$, Li_2CO_3 and Y_2O_3 shows two peaks.

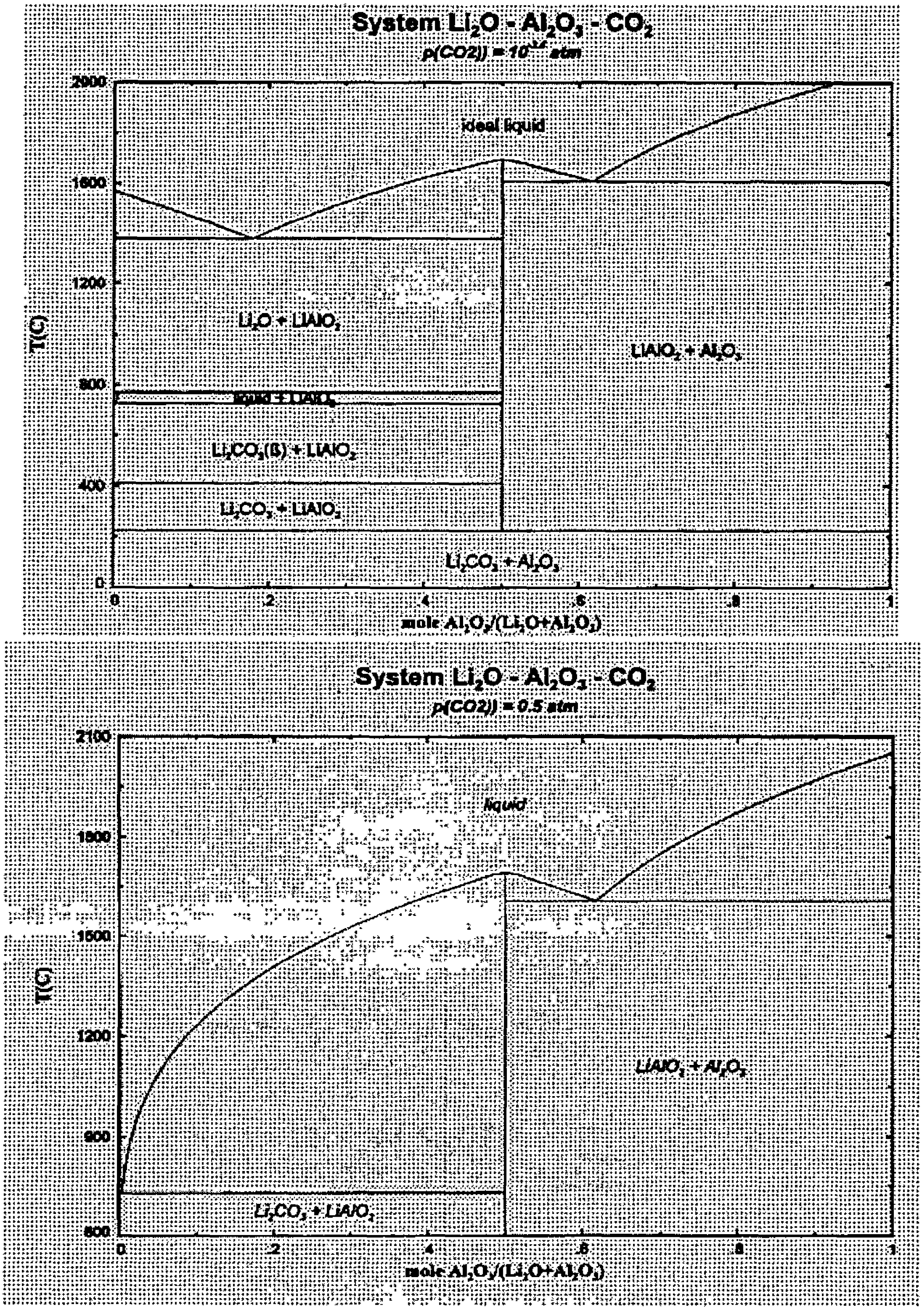

Figure 4-11. Li_2O-Al_2O_3-CO_2 phase diagram: upper at a CO_2 pressure of 400 ppm, lower Li_2CO_3 is stable over the temperature range of the diagram at a CO_2 pressure of 0.5 atm [Bal01].

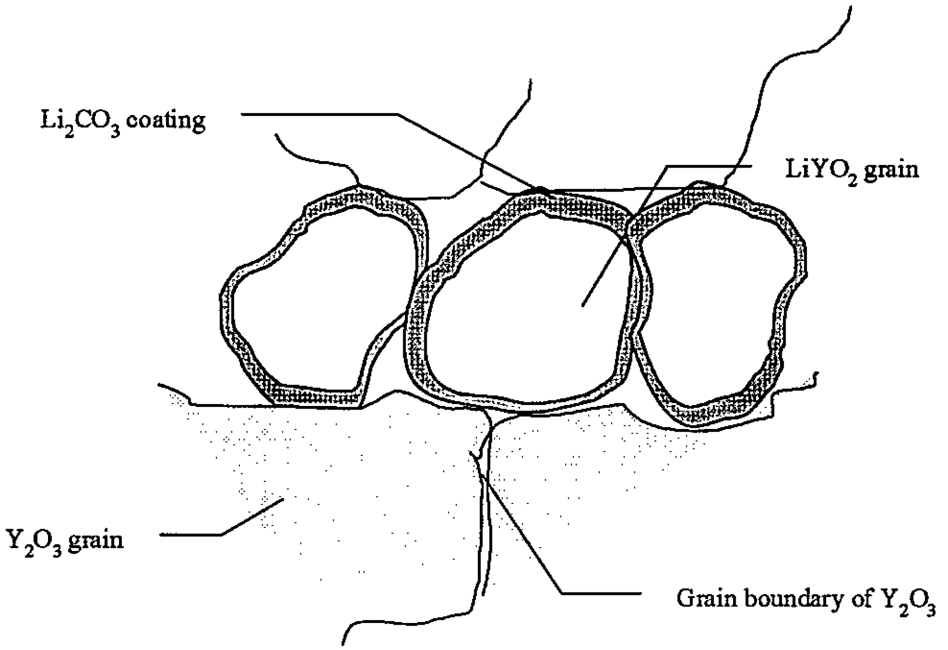

Figure 4-12. Sketch of interface of the tube and the lid before joint formation

i.e., a CO_2-rich atmosphere envelopes the sample during heating.

Based on process kinetics, the shrinkage which takes place is determined by the approach between particle centers and is

$$\frac{\Delta V}{V_0}=\frac{3\Delta L}{L_0}=\frac{9\gamma}{4\eta r}t \qquad \textbf{Eq. 4-1}$$

that is, the initial rate of shrinkage is directly proportional to the surface tension, γ and time, t, inversely proportional to the viscosity, η and inversely proportional to the particle size, r.

Consider the $LiYO_2$ particle coated with Li_2CO_3 initially in contact with either another $LiYO_2$ particle inside the tube or the Y_2O_3 particle at the interface between the tube and the lid (Figure 4-12).

A theoretical analysis of the influence of the liquid phase on the densification process can be made by considering a simple grain-liquid-pore model [Nan98] schematically shown in Figure 4-13. One of the most important manifestations of surface energy is that it gives rise to a pressure difference across the liquid-pore menisci. This pressure is exerted on every part of the solid liquid interface, and is given by equation

$$\sigma = \gamma_{lv}\left(\frac{1}{r_{pc}} - \frac{1}{r_1}\right) \qquad \text{Eq. 4-2}$$

where σ is the stress, γ_{LV} is the surface tension of the liquid-vapor interface (the pore), r_{pc} is the radius of the cylindrical pore, and r_1 is the radius of the contact region.

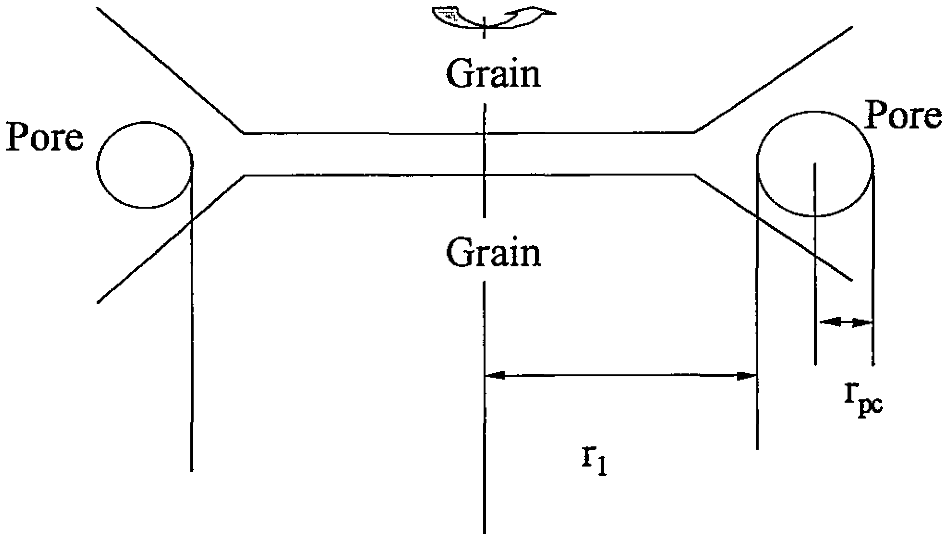

Figure 4-13. A model of the grain-pore-liquid system during densification

In the present sintering and joining procedure, the lid was already fully sintered Y_2O_3-12.5 wt.% MgO. If we compare the microstructure of the presintered tube with the lid we will find that the pores are smaller in the lid than in the tube. This means that a wetting liquid will preferentially flow into the lid by capillary attraction.

On the other hand, the chemical driving force for the reaction can be much larger than the driving force from surface energy [Ger85]. Swelling by interdiffusion prior to melt formation (Kirkendall porosity) may occur for $LiYO_2$ formed by reaction of Li_2CO_3 and Y_2O_3. This also leads to pore formation at prior Li_2CO_3 sites. During further heating, the liquid will be driven away from pore site due to capillarity. The pores can not be filled by

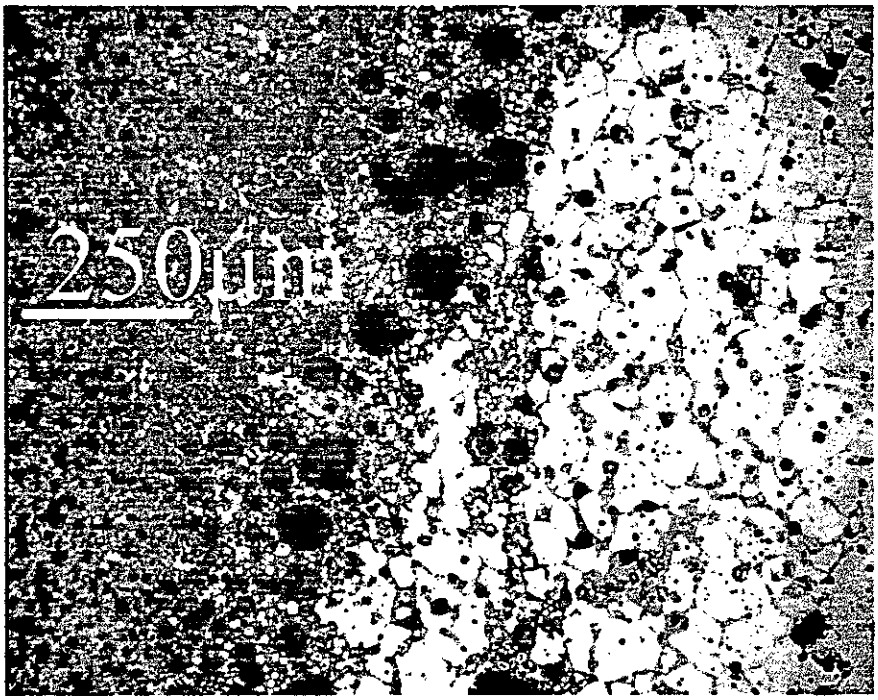

Figure 4-14. Micrograph of cross-section of joint shows a string of pores along the interface of the lid and the tube

rearrangement so in most cases, a string of pores along the boundary were observed (Figure 4-14).

The reaction of Li_2CO_3 with Y_2O_3 at the tube-lid interface triggered the further sintering of the tube from the bottom to the top.

Transient liquid phase sintering is highly sensitive to processing conditions. Any process variable change will influence the whole operation. It was very difficult to obtain uniformity among the finished tubes.

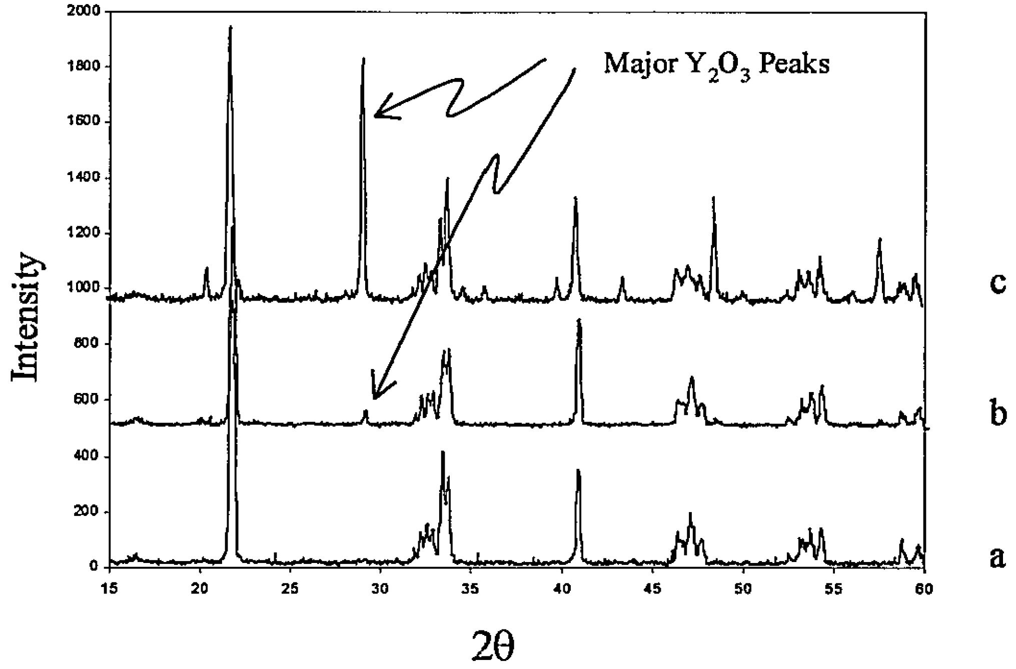

Figure 4-15. XRD of $LiYO_2$ powder, a) fresh powder, b) before slip casting, c) before presintering

4.1.4. Stability of $LiYO_2$

The sintering of $LiYO_2$ tubes as described above resulted in a product with very good stability. It maintained structural integrity in air for more than 2 years, as well as in contact with molten Li for several months. However, this does not imply phase purity of the $LiYO_2$ tube.

The thermodynamic properties of $LiYO_2$ are not available. XRD analysis showed the pure $LiYO_2$ pattern only for the fresh powder formed by reaction of Li_2CO_3 and Y_2O_3. After any further treatments, e.g., reheating the powder in air or recovering powder from dried ethanol slip or from presintered tubes, XRD analysis revealed the presence of Y_2O_3 formed by decomposition of $LiYO_2$ (Figure 4-15). No Li_2O, Li_2CO_3 or LiOH were detected by XRD, probably due to their amorphous nature.

However, DTA gave evidence for the existence of LiOH and Li_2CO_3 by way of endothermic peaks near 400 and 710°C, corresponding to the melting points of these compounds. Hence, we may conclude that $LiYO_2$ is not stable in air. Others have observed that $LiYO_2$ decomposed in air below 300°C [Roz76]. The thermodynamic data also show that $LiAlO_2$ is unstable at low temperatures, reacting with CO_2 in air to form Li_2CO_3.

Since the sintering process occurred very quickly, the final structure of the tube would be a non-equilibrated Li_2CO_3-$LiYO_2$ mixture. This material showed very good stability for months with molten Li to 800°C or to air without degrading or decomposing. It remains an interesting material for further study.

4.2. Measurement of the thermodynamic properties of the Li-Al system

4.2.1. Reference electrode

The reference electrode used to study the Li-Al system was Sn with approximately 1 at. % Li. The calibration curves of several reference electrodes versus pure Li against temperature is shown in Figure 4-16.

The calibration against pure Li versus T between 350 and 700°C can be represented

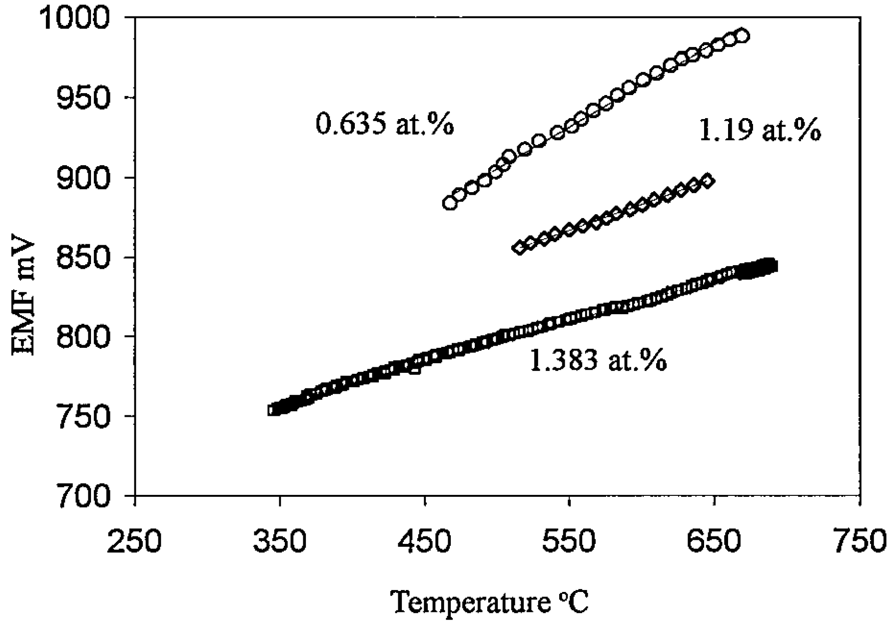

Figure 4-16. The reference electrode calibration with respect to pure molten lithium.

by the following equations :

Li at%	Expression	Correlation coefficient
0.635	EMF(mV) = 0.5198 T(°C) + 645.88	$R^2 = 0.9942$
1.19	EMF(mV) = 0.4244 T(°C) + 754.06	$R^2 = 0.9997$
1.383	EMF(mV) = 0.2550 T(°C) + 669.66	$R^2 = 0.9956$

4.2.2. EMF Data

Three WE cells were used in the investigation. The first cell was filled with a Li-Al alloy provided by Lockheed Missiles and Aerospace whose composition was known to be 14.5 at.% Li. The measurement started with this composition and temperature was cycled. Li was titrated into the cell to the next desired composition and the emf measurements were repeated. This cell worked for one month up to the maximum composition of 33.8% at. Li.

The starting composition of the second cell was pure Al. Li was titrated into the cell as before and 10 composition points was taken until the cell failed by cracking.

The third cell was started from 15.8 at.% Li by carefully weighing the desired amounts of Al and Li in the glovebox. The operation was as before but the Li was titrated out of the cell.

Figure 4-17 shows the variation of EMF with temperature of the Al-Li system for all three cells. As can be seen from Figure 4-17, the EMF of the liquid is a function of both temperature and composition.

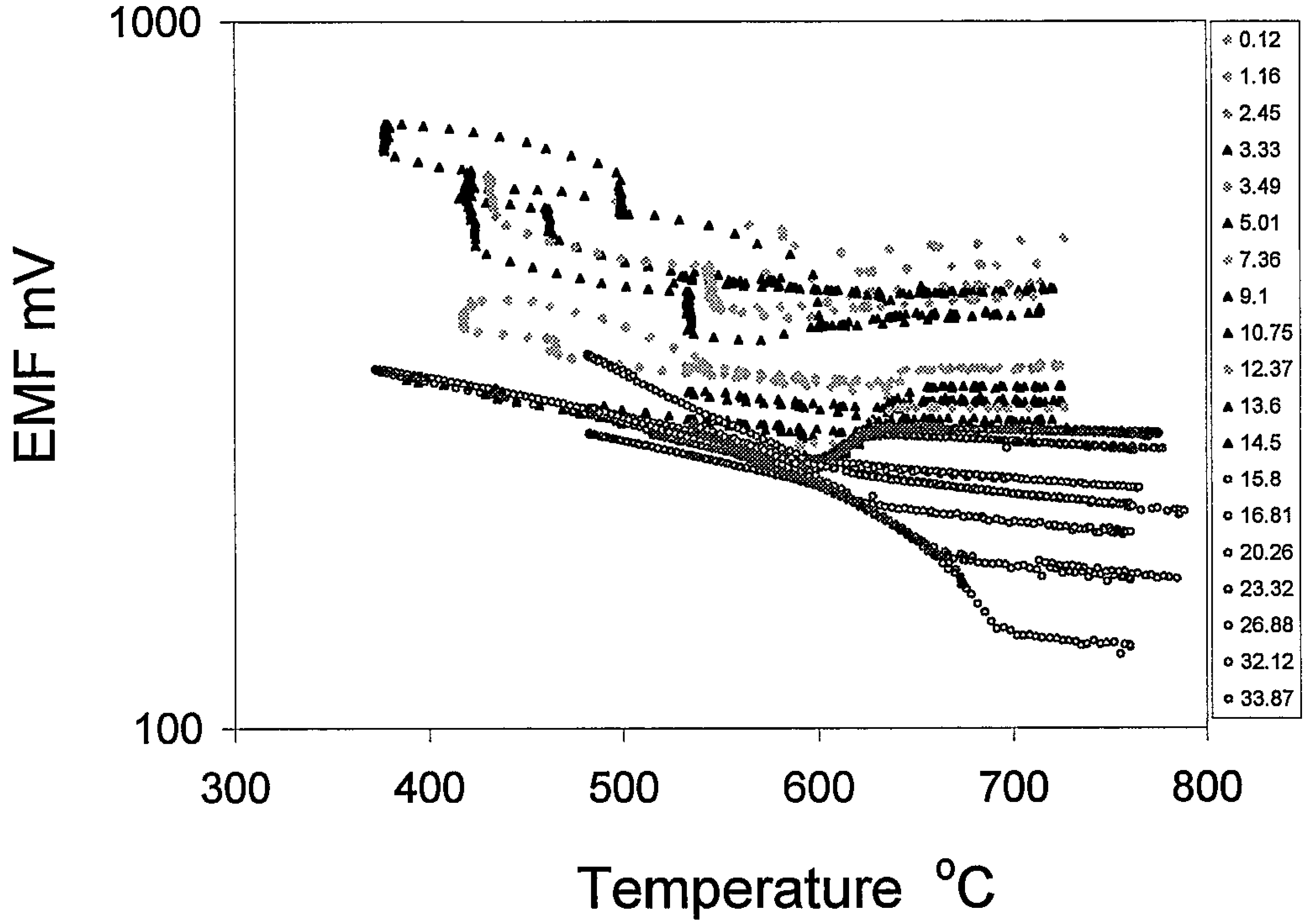

Figure 4-17. The EMF as a function of both temperature and composition. The liquidus and eutectic points can be directly observed from the curves of the EMF vs. temperature plot.

The emf was obtained not only for the liquid phase but also in the α phase and the α+β two phase region, which were not obtained by the emf technique before.

All the measured curves can be classified into 5 groups:

1. The measurements at compositions less than 5 at.% show only one transition , because the liquidus and solidus are too close to resolve.
2. The traces from 7 at.% to 12.37 at. % Li show two transition points. These two transitions denote the start and end of solidification (liquidus and solidus points).
3. For the lines between 12.37% and 23.33 at.% Li, we find a discontinuity in the slope of E vs. T as the temperature drops below the liquidus line into two phase region. This occurs at a unique point for all compositions, normally the eutectic point.
4. The line at 23.32 at.% shows only one transition and indicates the eutectic point of Li-Al system. The EMF below the eutectic represents a solid-solid equilibrium between the α phase and the β phase. We can find the eutectic point by interpolation of all the solid-liquid data.
5. When the composition of Li was larger than 23.32 at.% Li, the emf points between the two transitions trace out the hyper-eutectic liquidus line. The points below the eutectic temperature coincide with the α – β solid equilibrium mentioned previously.

Since the EMF is measured at thermodynamic equilibrium and is free from kinetic effects, the invariant points are determined with high precision. From the plot of EMF versus temperature in Figure 4-17, the good consistency is seen in the data. The higher Li concentration shows better reproducibility than at low Li compositions.

The measured phase diagram of Li-Al is shown in Figure 4-18. The eutectic point is 23.3 at.% Li at 600°C and the maximum solubility of Li in Al is 13.84 at.%. The $\alpha/\alpha+\beta$ phase boundary can be derived by calculation of the intersection point from EMF versus temperature curves. Table 4-1 gives the solidus and liquidus points measured. Least square fitting gave the following equation for relation of composition with temperature:

Liquidus: $T^{\circ}C = 0.0027x^3 - 0.2068x^2 + 0.8003x + 659.17$, $R^2 = 0.9944$, $x<23.3$ at.% Li

Liquidus: $T^{\circ}C = 411.59+8.039x$, $R^2 =0.9957$, $23.3<x<33.87$ at.% Li

Solidus: $T^{\circ}C = -0.4012x^2 + 1.2964x + 658.68$, $R^2 = 0.9931$, $x<13.84$ at.% Li

$\alpha/\alpha+\beta$ boundary $T^{\circ}C = -49.58+47.44x$, $R^2 =0.9806$, $x<13.84$ at.% Li

The EMF was measured as a function of temperature between 350~790°C. The data were least squares fitted to an equation of the form.

$$E = A + BT + CT \ln T \qquad \textbf{Eq. 4-1}$$

The third term of the expression takes into account the curvature of E vs T and represents the partial excess heat capacity. The data were separated into two parts: liquid solutions and solid solutions. The results are listed in Table 4-2. The partial values of the four thermodynamic functions, G, H, and S, are derived as follows:

Table 4-1. Measured liquidus and solidus

X (Li at.%)	Liquidus	Solidus	X (Li at.%)	Liquidus	Eutectic
0	660.0	660.0	13.64	637.7	602.7
0.12	660.6	659.4	14.50	636.5	600.0
1.16	658.7	657.5	15.80	630.3	600.6
2.45	659.4	658.7	16.81	626.5	599.0
3.49	658.1	658.1	20.26	611.1	599.7
5.01	658.1	654.9	23.32	601.4	600.7
7.36	653.0	650.5	26.88	624.3	601.2
9.10	653.0	635.9	32.12	669.4	603.3
10.75	649.8	624.4	33.87	685.4	599.2
12.37	643.5	612.4			

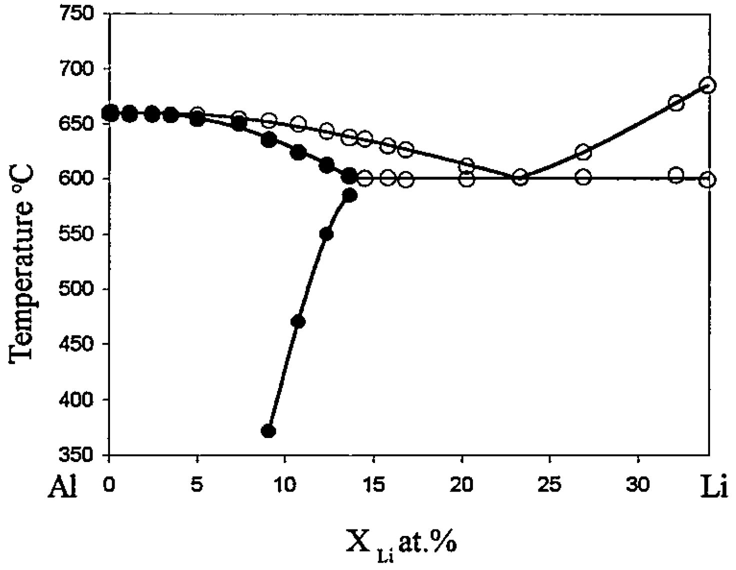

Figure 4-18. Phase diagram of Li-Al binary alloy from this study

$$\Delta G_{Li} = -FE = -F(A + BT + CT\ln T)$$ **Eq.4-2**

$$\Delta S_{Li} = F\frac{\partial E}{\partial T} = F(B + C + C\ln T)$$ **Eq.4-3**

$$\Delta H_{Li} = \Delta G_{Li} + T\Delta S_{Li} = F(-A + CT)$$ **Eq. 4-4**

4.2.3. Liquid Phase

The liquid region had more reproducible results, especially near eutectic compositions. From the Table 4-2, the isothermal EMF data was calculated at 660°C. The polynomial regression for EMF versus composition gave the equation:

$EMF=0.51128-0.0344X+0.00156X^2$ **R^2=0.982**

The relation of emf versus composition of Li is plotted in Figure 4-19, from which the activity of Al and Li were calculated. All these results are shown in Figure 4-20 and 4-21.

The total excess Gibbs energy of mixing was then directly calculated from the measured activity coefficients of Li and the results are shown in Figure 4-22.

Measurements of dE/dT were used to obtain the partial entropy. The variations with composition of S^E_{Li} are plotted in Figure 4-23. Partial excess entropies and enthalpies of Al were calculated by Gibbs-Duhem integration

The total entropy and enthalpy of mixing was plotted in Figure 4-24. The total entropy of mixing has a maximum at about 0.6 J/mol K at 10 at.% Li, and decreases thereafter.

Table 4-2. EMF vs. temperature for liquid phase data of the Li-Al system, EMF=A+B+CTlnT (T:K)

X_{Li} at.%	A	B	C
0.12	0.599096	-0.00252	0.00036
1.16	0.680711	-0.00256	0.000338
2.45	0.637481	-0.00258	0.000345
3.33	0.546728	-0.00257	0.000354
3.49	0.636259	-0.0026	0.000344
5.01	0.699558	-0.00268	0.000339
7.36	0.443032	-0.00127	0.000167
9.1	0.430489	-0.00112	0.000144
10.75	-1.58229	0.015359	-0.00195
12.37	0.366787	-0.00062	0.000078
12.89	-0.84784	0.009905	-0.00127
13.64	0.035526	0.002175	-0.00028
14.5	-1.28994	0.013168	-0.00168
15.8	-0.12959	0.003442	-0.00044
16.81	0.615597	-0.00227	0.000276
20.26	0.639574	-0.00257	0.000312
23.32	0.840739	-0.004	0.000487
26.88	0.899482	-0.00479	0.000591
32.12	0.900273	-0.00505	0.000625
33.87	1.599948	-0.01091	0.001367

Table 4-3. EMF vs. temperature for α solid solution and $\alpha+\beta$ two phase region of the Li-Al system, $EMF=A+B+CT\ln T$ (T:K)

X_{Li}	A	B	C
0.120	16.701	-0.141	0.018
1.160	60.318	-0.517	0.066
2.450	-12.574	0.110	-0.014
3.330	4.084	-0.031	0.004
3.490	-4.543	0.040	-0.005
5.010	15.036	-0.128	0.016
7.360	2.319	-0.017	0.002
9.100	1.500	-0.010	0.001
10.750	0.421	0.000	0.000
12.370	1.096	-0.004	0.000
12.890	1.373	-0.009	0.001
13.280	10.133	-0.089	0.011
14.500	0.671	-0.001	0.000
15.800	0.505	0.000	0.000
16.810	0.799	-0.003	0.000
20.260	0.493	0.002	0.000
23.320	3.647	-0.026	0.003
26.880	1.518	-0.009	0.001
32.120	-1.552	0.020	-0.003
33.870	0.451	0.000	0.000

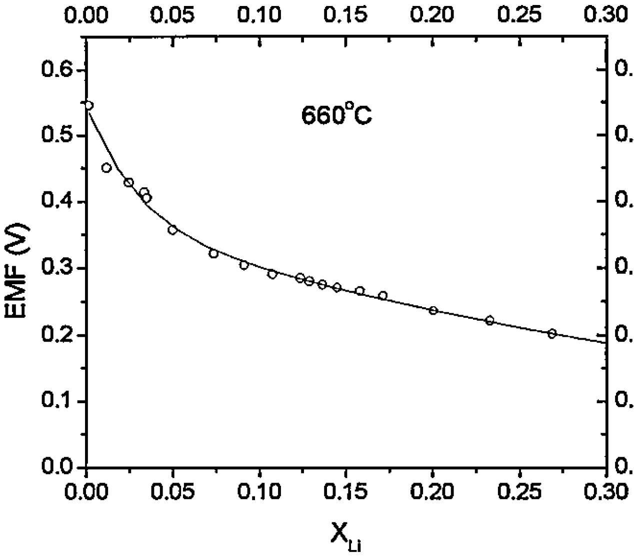

Figure 4-19. EMF vs. composition of Liquid at 660°C

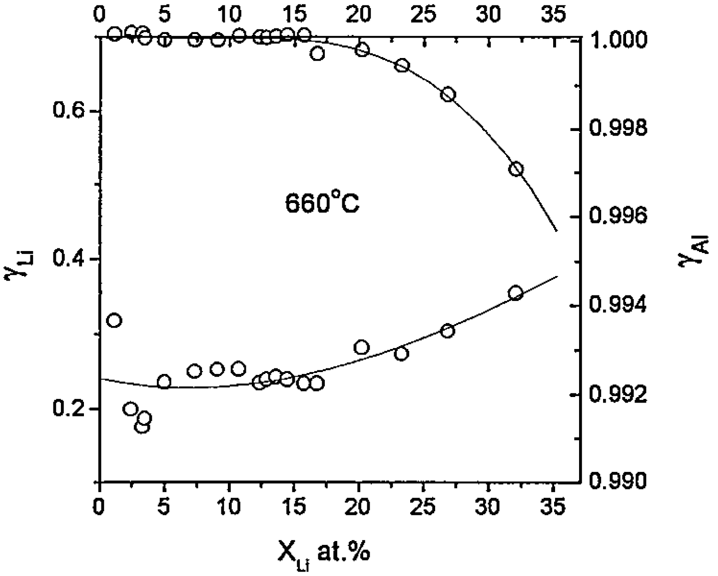

Figure 4-20. Activity coefficient of Li in Al at 660°C

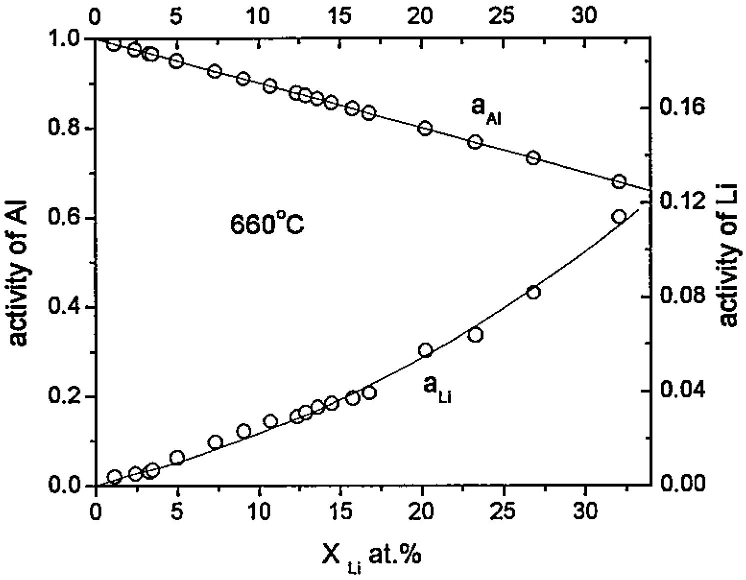

Figure 4-21. Activity of Al and Li at 660°C

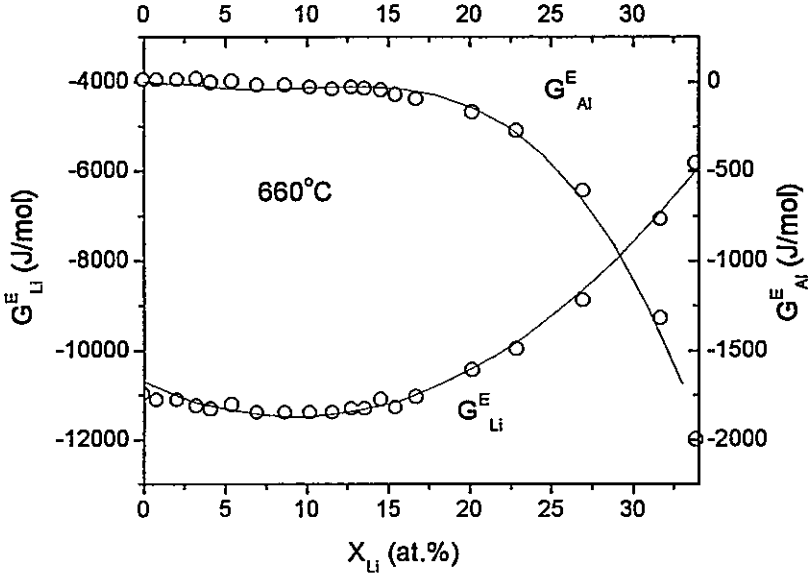

Figure 4-22. The partial excess Gibbs energy vs. composition at 660°C

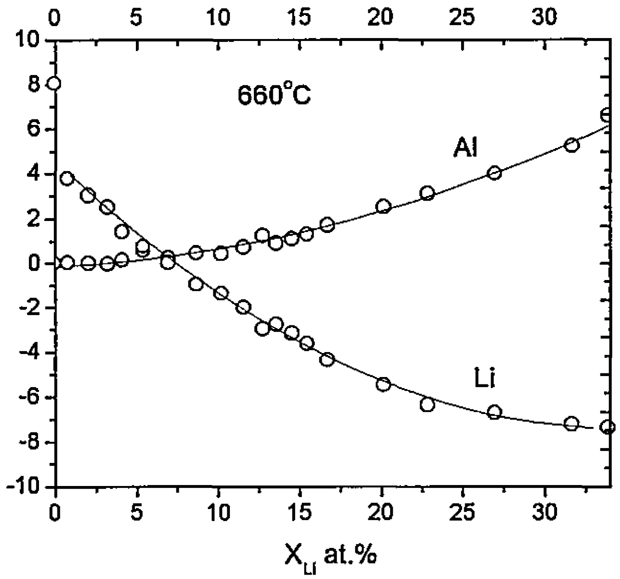

Figure 4-23. Variations of the partial entropy of Li and Al at 660°C

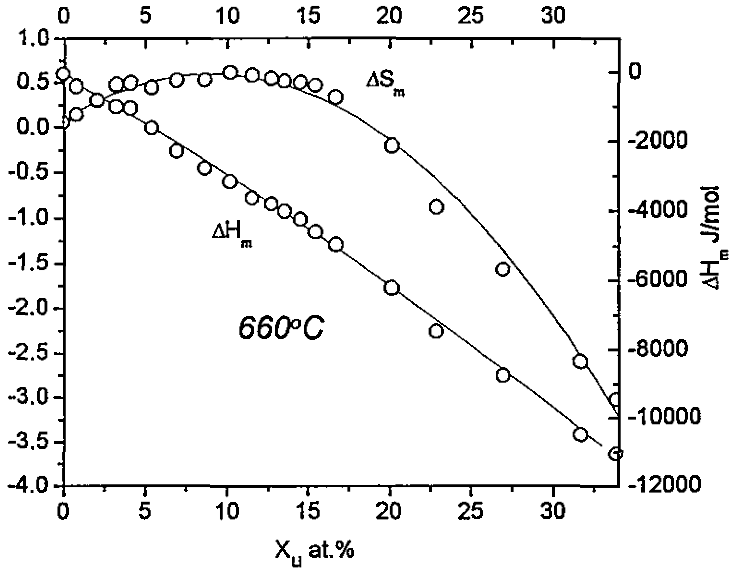

Figure 4-24. The total entropy and enthalpy of mixing vs. composition of Li at 660°C

The total Gibbs energy of mixing is shown in Figure 4-25. The excess Gibbs energy of mixing of the liquid was modeled as a regular solution, a subregular solution and as a 3-term expression including temperature (Figure 4-26).

$G_m^E = -13618 X_{Li} X_{Al}$ J/mol (regular solution)

$G_m^E = (-11574 - 10212 X_{Li}) X_{Al} X_{Li}$ J/mol (subregular solution)

$G_m^E = (-37088 - 10043 X_{Li} + 27T) X_{Al} X_{Li}$ J/mol (with temperature term)

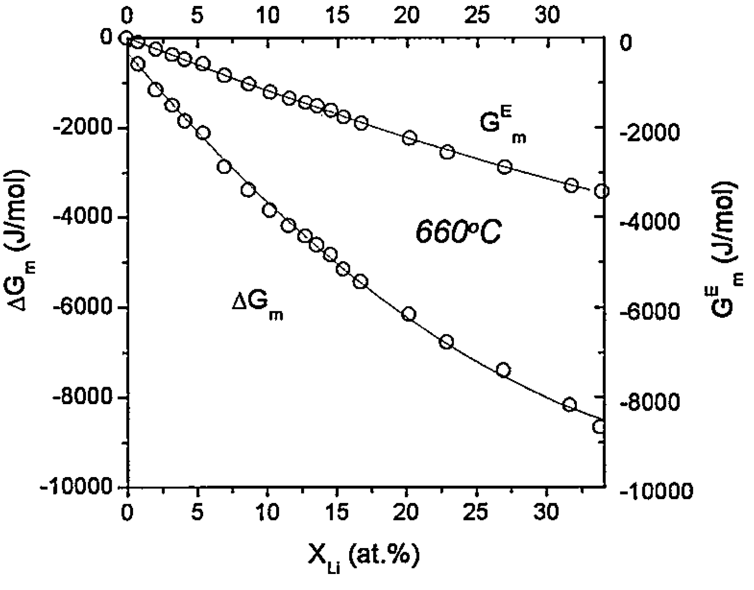

Figure 4-25. The total Gibbs energy of mixing and the total excess Gibbs energy of mixing vs. composition at 660°C

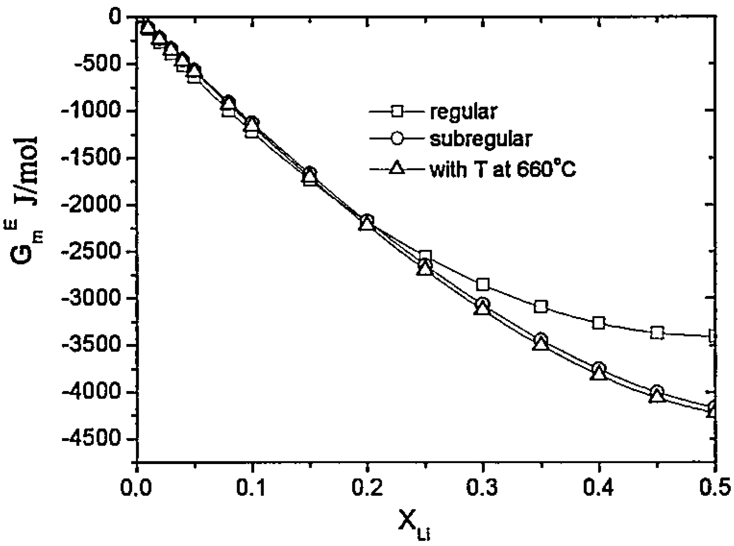

Figure 4-26. The excess Gibbs energy of mixing of the liquid was modeled as a regular solution, a subregular solution and as a 3-term expression including temperature.

4.2.4. Solid Phase and α+β Two-Phase Region

Although the data acquired from the α solid solution phase became more ambiguous when temperature was below 500°C, the data above 500°C in Figure 4-17 appear to be consistent. When we curve-fitted the data by the least square method and combined them with the data from the α+β two phase region, we may obtain the thermodynamic properties of the α phase and α+β two phase region.

For the α+β two phase region, there is still uncertainty about the α' phase. A number of investigations, both theoretical and experimental [Kha88, Nob98], have failed to arrive at a consistent result.

It is generally recognized that the α' phase precipitates when a homogeneous α solution is cooled into the metastable two phase field. This precipitate has the $L1_2$ structure [Nob71, Wil75]. The stoichiometry of the ordered phase is uncertain because of the difficulty of extracting the precipitate or analyzing the lithium content in situ.

By means of FACT [Bal01] we combined the present data and data from the literature [Che89] to model the phase equilibria between the liquid, α, α' and β phases (Figure 4-27). The Gibbs energy of the solid phases is shown in Figure 4-28 at different temperatures.

Since no thermodynamic data are available for the α' phase, it was modelled on the assumption of a 400°C peritectic temperature, which is an approximate value among the scatter in the literature. An explanation for the scatter among numerous studies using different techniques is illustrated by the tangent to the Gibbs energy. At 400°C, for example, the tangent line is almost coincident with the α Gibbs energy curve from 0 to 10% Li. Hence the relatively tiny driving force is unable to overcome the barrier for nucleation of the α' phase. As a result, nucleation becomes possible only at large concentration of Li. However, our phase diagram calculations show a very low solubility (~1%) of Li in the presence of the α' phase.

On this basis the following hypothesis is proposed for the Al-Li system. The α' phase is stable but hard to nucleate. It may be formed from the α phase by appropriate heat treatment. It is unlikely to nucleate from a stable α+β two phase composition, because of the low difference in Gibbs energy. The low temperature, implying slow kinetics, is a further barrier

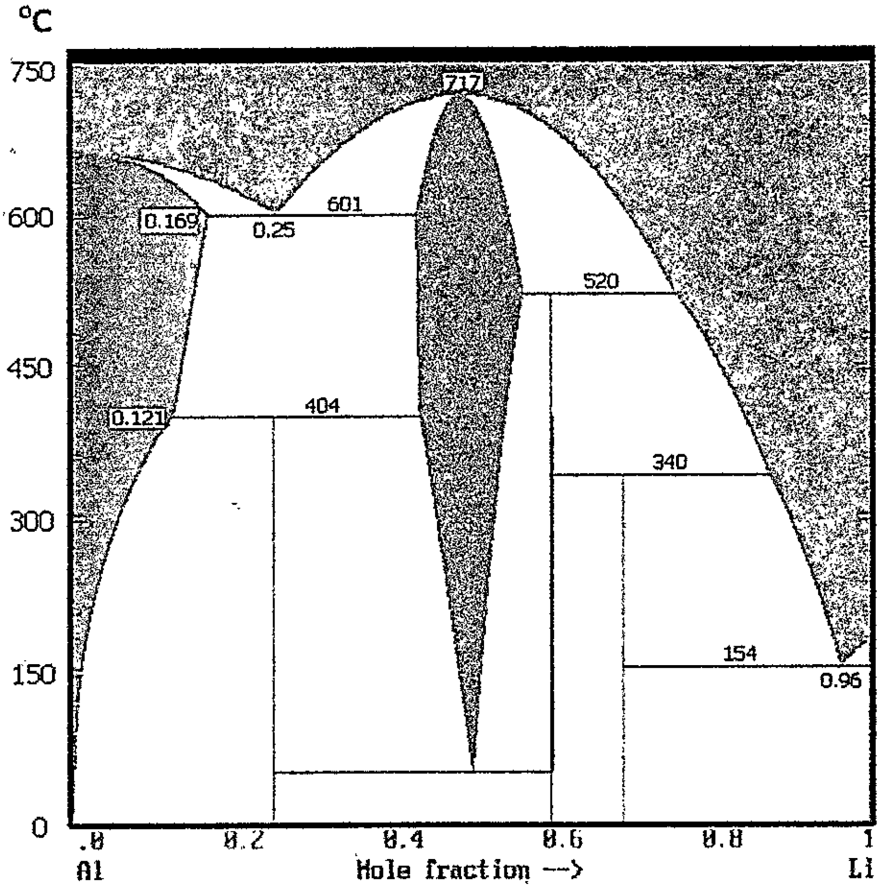

Figure 4-27. The phase diagram modeled by FACT [Bal01]

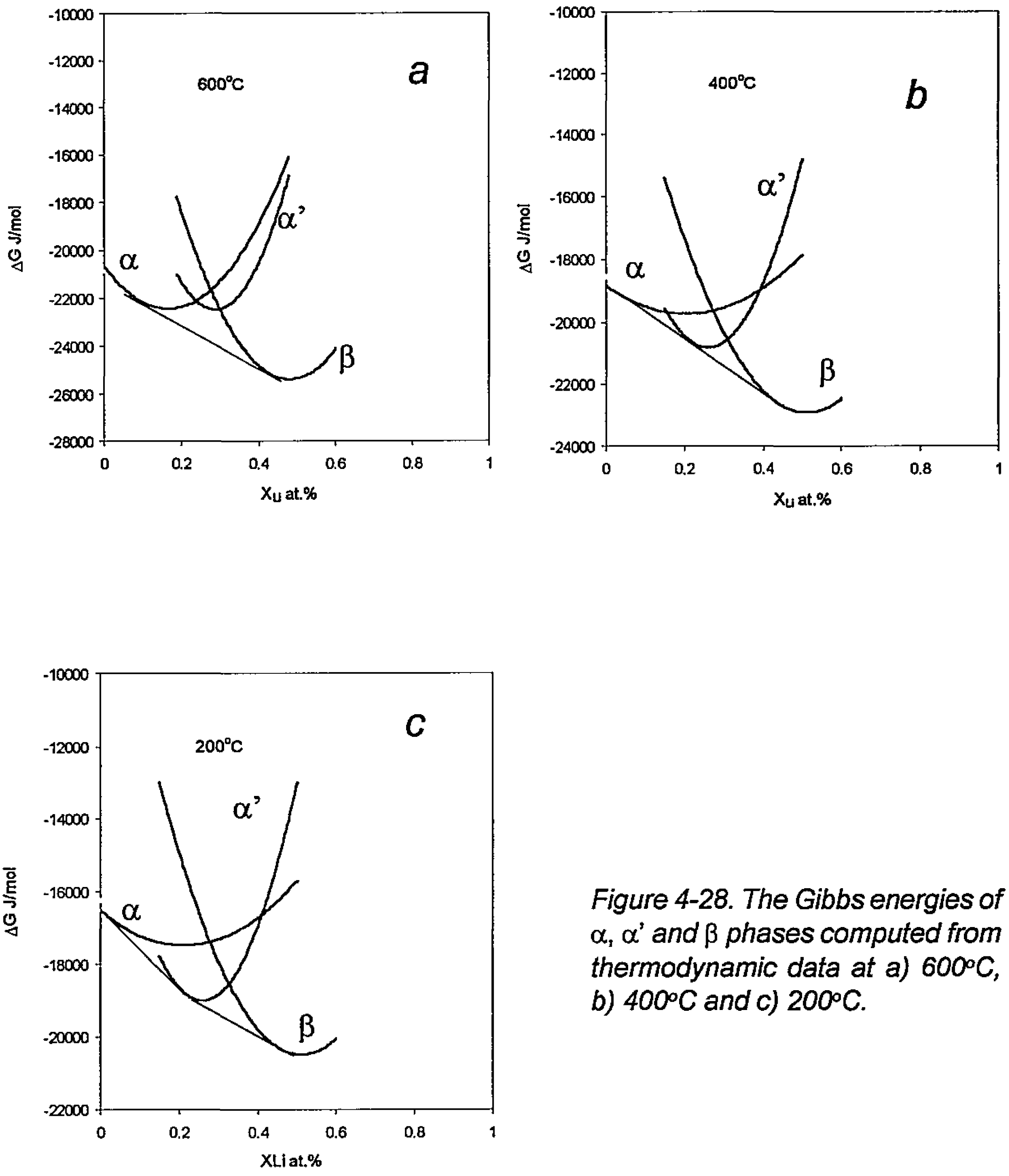

Figure 4-28. The Gibbs energies of α, α' and β phases computed from thermodynamic data at a) 600°C, b) 400°C and c) 200°C.

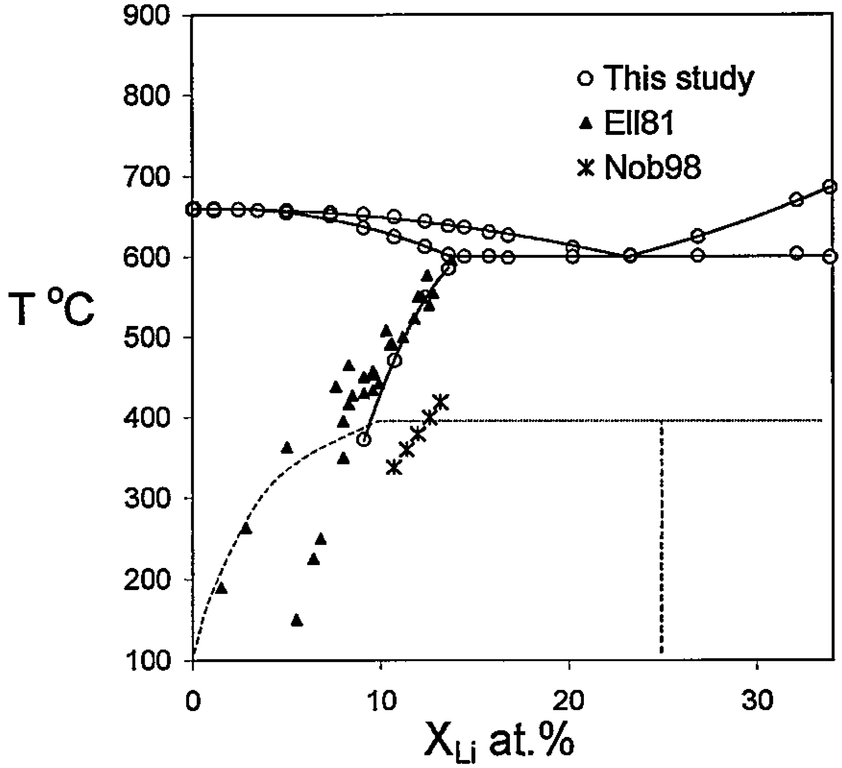

Figure 4-29. Comparison of phase diagram at Al rich portion

to nucleation of α'. Therefore, the aluminum-rich portion of the phase diagram consists of an α-Al solid solution, a β-LiAl compound, a stable α+β two phase region at high temperatures (400~600°C), and an equilibrium α'-Al_3Li phase or a metastable α+β two phase equilibrium at lower temperature when α' does not form. Previous phase diagram that omitted the α' phase or labelled it as a metastable phase are incorrect.

4.2.5. Comparison with the Literature

By comparing the results of this study and the literature (Figure 4-29 and 4-30), it can be seen that the liquid phase boundary, eutectic point, and the activities of liquid and α phases are in reasonable agreement. This demonstrates the accuracy of the apparatus and the usefulness of the new Li solid electrolyte.

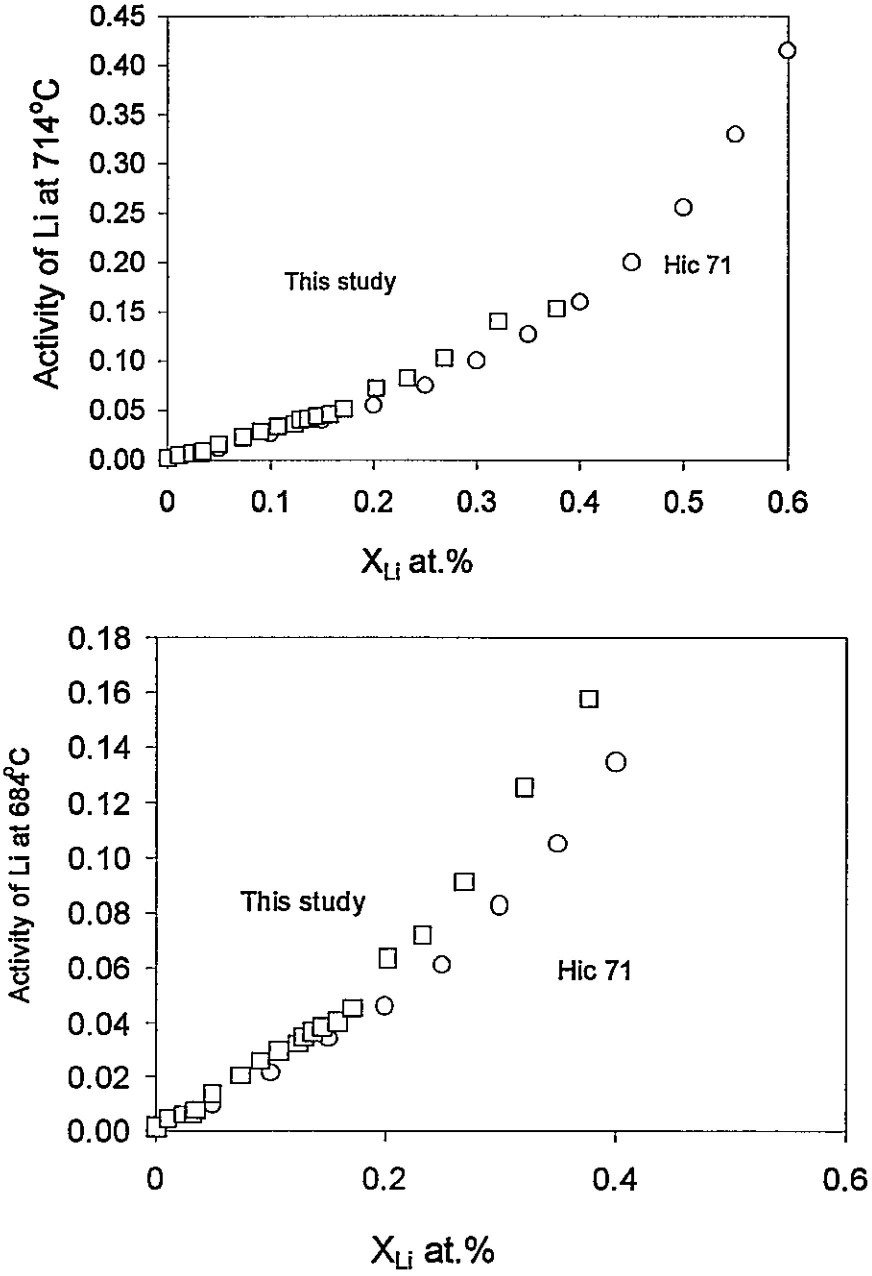

Figure 4-30. Comparison of activity in this study with that in the literature: upper 714°C, lower 684°C.

Chapter 5. CONCLUSIONS

This study achieved two goals:

First, the role of Li_2CO_3 in fabrication of the solid electrolyte cell was revealed. The tube and lid were joined by reaction bonding in which Li_2CO_3 served as the bonding agent and a sintering additive. The cell fabricated in this way worked steadily for several months in contact with liquid lithium.

Secondly, the thermodynamic properties of Li-Al alloys, including the liquid phase, the α-solution region, and the $\alpha+\beta$ two-phase region were investigated in the temperature range 370 to 790°C. The liquidus line could be directly observed from the curves on the EMF versus temperature plot. The solid-liquid phase boundary was consistent with data from the literature. The probe measurements showed high reproducibility from cell to cell. It can be concluded that $LiYO_2$ is a proper Li electrolyte, and that the reaction bonding technique is appropriate for constructing the emf cell.

A more detailed list of conclusions is given below:

1. The joining of the $LiYO_2$ tube to the Y_2O_3-MgO lid was aided by the reaction of Li_2CO_3 with Y_2O_3. The joining process was followed by a rapid sintering of the

tube, aided by the presence of liquid Li_2CO_3. The optimum amount of Li_2CO_3 was found as 3 wt.%.

2. The method depends on a rapid firing process to avoid decomposition of the carbonate and subsequent loss of the liquid phase. It may be possible to replace the rapid firing process by use of a controlled CO_2 atmosphere in order to maintain the Li_2CO_3 phase to high temperatures.

3. Overheating of the sample results in excessive liquid phase formation and collapse of the tube.

4. Y_2O_3-MgO lids showed excellent chemical resistance to molten lithium as well as good mechanical properties.

5. The stability of $LiYO_2$ was studied by XRD and DTA. The $LiYO_2$ will decompose during fabrication of the tube at temperatures below 300°C. Free Y_2O_3 can be detected during subsequent processing steps with $LiYO_2$.

6. Thermodynamic properties of Al-Li alloys were measured or derived in the range of 0~33.87 at.% Li. This included the liquid phase, α-solution region and $\alpha+\beta$ two phase region. The eutectic point in this study was found at 23.3 at.% Li at 600°C (873 K); the maximum solubility of Li in Al is 13.84 at.% at the eutectic temperature.

7. The α solidus measured here can supplement the measuring data from the literature and the measured $\alpha/\alpha+\beta$ boundary shows good agreement with the literature.

8. The rest of the thermodynamic data were calculated from the EMF at different temperatures or different compositions, including the partial entropy, partial enthalpy, and partial Gibbs energy.

9. The activity of Li in the liquid phase in this study is consistent with those in the literature.

REFERENCES

Ada96 G.Y. Adachi, N. Imanaka and H. Aono, Adv. Mat., 8 (1996) 127.

Ala84 J. Alamo and R. Roy, J. Am. Cer. Soc., 63 (1984) C78.

Alp77 U. Von Alpen, A. Rabenau and G.H. Talat, Appl. Phys. Lett., 30 (1977) 621.

Aon92 H. Aono, E. Sugimoto, Y. Sadaoka, N. Imanaka and G. Adachi, Bull. Chem. Soc. Jpn., 65, 8 (1992) 2200.

Aon93 H. Aono, E. Sugimoto, Y. Sadaoka, N. Imanaka and G. Adachi, Solid State Ionics, 62 (1993) 309.

Att90 A. Attewell, Chem. and Ind., 5 (1990) 131.

Ayg89 T.Y. Aygub and W. Boguaz, Solid State Ionics, 36 (1989) 247.

Bal01 C.W. Bale, A.D. Pelton and W.T. Thompson, FACTSage 5.0 (Ecole Polytechnique de Montreal / Royal Militeray College, Canada, 2001, http: // www.crct.polymtl.ca)

Bef95 W.K. Beffi and E.J. Plichta, U.S. Patent No. 5,458,995, 17 Oct. 1995.

Bha70 A.B. Bhatia and D.E. Thornton, Phs. Rev., 32, 3004,1970.

Bie97 R.M. Biefeld and R.T. Johnson Jr., J. of The Electrochemical Society, Vol126, No.1, pp1-6, Jan. 1979.

Bon78 I.A. Bondar and L.N. Koroleva, Russ. J. Inorg. Chem., 23, 900 (1978); Zh. Neorg. Khim., 23, 1636 (1978).

Bro96 T. Brousse, R. Marchand, R Fragnaud and D.M. Schleich, Presentation at the 190th Meeting of the Electrochemical Society, San Antonio, TX, USA, Oct. 8, 1996.

Bru80 P.G. Bruce and A.R. West, Mat. Res. Bull., 15 (1980) 117.

Bru82 P.G. Bruce, AR. West, J. Solid State Chem., 44 (1982) 354.

Bru84 P.G. Bruce, A.R. West, J. Solid State Chem., 53 (1984) 430.

Bru95 P.G. Bruce, "Solid state electrochemistry", Cambridge University Press, 1995

Cer77 Ceresara, S., Cocco, G., Fagherazzi, G., and Schiffini, L., "Determination of the d' Coherent Solvus in the Al-Li System by Small-Angle X-Ray Scattering", Philos. Mag., 35, 373-378(1997).

Cha96 J - B. Chavarria, P. Quintana, A. Huanosta, Solid State lonics, 83 (1996) 245.

Che89 SINN-Wen Chen, Chia, Chia-Hong Han, Jen-Chwen Lin and Y Austin Chang, Phase Equilibria of the Al-Li Binary System, Metallurgical Transaction A, Volume 20A. November 1989-2247

Cho89 BY.R. Chowdari, K. Radhakrishnan, K.A. Thomas and G.V. Subba Rao, Mat. Res. Bull. 24 (1989) 221.

Cob81 R.L. Coble, Reactive sintering, Proceedings of the 5th international Round Table Conference on Sintering, Sep 1981.

Cob82 R. L. Coble, "Reactive Sintering,", Sintering - Theory and Practice, D. Kolar, S. Pejovnik, and M. M. Ristic (eds.), Elsevier Scientific, Amsterdam, Netherlands, 1982, pp.145-151.

Cos62 L.P. Costa and R.P. Marshall, "The Solubility of Li in Al", Trans. AIME, 224, 970-974 (1962), (Equi Diagram; Experimental).

Dar67 L.S. Darken, "Thermodynamics of Binary Metallic Solutions", Trans. AIME, 239, 80-89, 1967.

Dis95 M.A.K.L. Dissanayake, R.P. Gunawardane, H.H. Sumathipala and AR. West, Solid State lonics, 76 (1995) 215.

Dub72 B.L. Dubey and A.R. West, Nat. Phys. Sci., 235 (1972) 155.

Dub73 B.L. Dubey and A.R. West, J. Inorg. Nuel. Chem., 35 (1973) 3713.

Eic81 G.Eichinger, Decomposition mechanisms of some lithium ionic conductors, solid state ionics, 2 (1981) 289-295.

Ell81 R.P. Elliott and F.A. Shunk, The Al-Li (Aluminum-Lithium) System, Bulletin of Alloy Phase Diagrams, Vol.2, No.3, 1981.

Esa87 T. Esaka, M. Greenblatt, J. Solid State Chem., 71 (1987) 164.

Esa89 T. Esaka, Y. Kohayashi, H. Obata, H. Iwahara, Solid State Ionics, 34 (1989) 287.

Far85 G.C. Farrington, B.S. Dunn and J.L. Briant, Solid State Ionics, 3-4 (1981) 405.

Fau98 M Faucher, P.Sciau, Jkiat, M. Alves and F. Bouree, Journal of Solid State Chemistry, 137 (1998) 242-248.

Flo87 M.H. Flower and P.J. Gregson, Mater. Sci. Technol., 3, 81,1987.

Gar90 A. Garcia, G. Torres-Trevino and A.R. West, Solid State Ionics 40-41 (1990) 13.

Ger85 R.M. German, "Liquid phase sintering", pp2, Plenum Press, New York, 1985.

Goo76 J.B. Goodenough, HY-R Hong and LA. Kafalas, Mat. Res. Bull., 11 (1976) 203.

Gri86 J. Grins and AR. West, J. Solid State Chem., 65 (1986) 261.

Gru35 G. Grube, L. Mohr and W. Breuning, "Electrical Conductivity and Phase Diagram of Binary Alloys Li-Al", Z.Electrochem., 41, 880-882 (1935) in Germen.

Hag68 L.O. Hagman, P. Kierkegard, Acta Chem. Scand. 22 (1968) 1822.

Hee77 B. Heed, A. Lunffin and K. Schroeder, Electrochim. Acta, 22 (1977) 705.

Hel80 E.E. Hellstrom and W. Van Gool, Constraints for the selection of lithium solid electrolytes, Revue de Chimie minerale, t.17, 1980, p. 263.

Hen94 G.L. Henriksen and D.R. Vissers, J. Power Sources, 51 (1994) 115.

Hic71 J.M. Hicter, A. Vermande, I. Ansara and P. Desre, "Thermodynamic Study of Liquid Al-Li Alloys", Rev. Int. Temper. Refr., 8, 197-200(1971) in French.

Hod76 I.M. Hodge, M.D. Ingram and AR. West, J. Am. Cer. Soc., 59 (1976) 7.

Hon76 HY-R Hong, Mat. Res. Bull., 11 (1976) 173.

Hon78 HY-R Hong, Mat. Res. Bull., 13 (1978) 117.

Hop59 R. Hoppe, Angew. Chem., 71 (1959) 457.

HP HP 34401A Multimeter, User's Guide, Hewlett Packard.

Hu76 Y.W. Hu, J. D. Raistrick and R.A. Huggins, Mat. Res. Bull., 11 (1976) 1227.

Hug77 R.A. Huggins, Electrochim. Acta, 22 (1977) 773.

Ina93 Y. Inaguma, C. Liquan, M. Itoh, T. Makamura, T. Uchida, H. Ikuta and M. Wakihara, Solid State Comm., 86 (1993) 689.

Ina94 Y. Inaguma, L. Chen, M. Rob and T. Nakamura, Solid State Ionics, 70-71 (1994) 196.

Iry89 J.T.S. Iryine, A.R. West, in T. Takahashi (Ed.), High Conductivity Solid Ionic Conductors, World Scientific Pub. Co., Singapore, 1989.

Iva88 A.K. Ivanov-Shits, S.E. Sigaryov, Solid State Ionics, 27 (1988) 89.

Jac83 K. Jackowska, A.R. West, J. Mat. Sci., 18 (1983) 2380.

Jac85 K. Jackowska, A.R. West, J. App. Electrochem. 15 (1985) 459.

Joh76 R.T.Johnson, Jr., R.M. Biefeld, M.L.Knotek, and B.Morosin, J. of The Electrochemical Society 123, 680 (1976).

Jon59 W.R.D. Jones and P.P. Das, "The Solid Solibility of Li in Al", J. Inst. Met., 87, 338-340 (1959).

Kan88 R. Kanno, Y. Takeda and O. Yamamoto, Solid State Ionics, 28-30 (1988) 1276.

Kan89 R. Kanno, Y. Takeda, M. Mori and O. Yamarnoto, Chem. Lett., 9-10 (1989) 223.

Kaw94 H. Kawai and J. Kuwano, J. Electrochem. Soc., 141 (1994) L78.

Kel67 W. Klemm and D. Kunze, Chem. Soc. (london) Spec., Publ. No.22 (1967), p.3; B.W.Mott, ibid., p.92; C.E. Messer, ibid., p.183.

Kha88 A.G. Khachaturyan, T.F. Lindsey and J.W. Morris Jr., Metallurgical Trans. A, 19A, 249 (1988).

Kho81 A. Khorassani, G. Uquierdo and A.R. West, Mat. Res. Bull., 16 (1981) 1561.

Kho82 A. Khorassani and A.R. West, Solid State Ionics, 7 (1982) 1.

Kho84 A. Khorassani and AR. West, J. Solid State Chem. 53 (1984) 369.

Kin75 W.D. Kingery, H.K.Bowen and D.R.Uhlmann,"Introduction to ceramics", John Wiley & Sons, Inc,1975.

Kir51 J.G. Kirkwood and F.P. Buff, "The Statistical Mechanical Theory of Solutions. 1", J. Chem. Phys. 19, 774-77.,1951.

Kub67 O. Kubaschewski, 1967, Metallurgical Thermochemistry, Pergamon press, Oxford, England, Chapter 2 et al.

Kuw80 J. Kuwano and AR. West, Mat. Res. Bull., 15 (1980) 1661.

Lap83 T. Lapp, S. Skarrup and A. Hooper, Solid State Ionics, 11 (1983) 97.

Lau92 R.J. Lauf and J.H. DeVan, "Evaluation of Ceramic Insulators for Lithium Electrochemical Reduction Cells", J. Electrochem. Soc., Vol 139, No. 8, Aug. 1992.

Lee91 CK. Lee and AR. West, J. Mat. Chem., 1 (1991) 149.

Lee93 CK. Lee, A.R. West, J. Mat. Chem., 3 (1993) 191.

Lev63 E.D. Levine and E.J. Rapperport, "A Study of the Al-Li System Between Al and Al-Li", Trans. AIME, 227,1204-1208 (1963), (Equi Diagram; Experimental).

Lew85 M.D. Lewis, N. Kimura and M. Greenblatt, J. Solid State Chem. 58 (1985) 401.

Lia73 C.C. Liang, J. Electrochem. Soc., 120 (1973) 1289.

Lun83 A. Lunden, A. Bengtzelius, R. Kaber, L. Nilsson, K. Schroeder and R. Tdrneberg, Solid State Ionies, 9-10 (1983) 89.

Lun86 A. Lunden, in BY.R. Chowdari and S. Radhakrishna (Eds.), Batteries, Sensors and Heat Storage Materials for Solid State Batteries, World Scientific Pub. Co., Singapore, 1986.

Lun94 A. Lunden, K. Schroeder and H. Ljungmark, Solid State Ionics, 28-30 (1994) 262.

Lut91 H.D. Lutz, A. Pfitzrter and C. Wickel, Solid State lonics, 48 (1991) 131.

Lut93 H.D. Lutz, Z. Zhang and A. Pfitzner, Solid State lonics, 62 (1993) 1.

Mar73 V.A. Maroni, E.J. Cairns and F.A. Cafasso, U.S. Gov't. report no. ANL-8001 (1973).

Mas95 C. Masquelier, M. Tabuchi, T. Takeuchi, W Soizumi, H. Kageyama and O. Nakamura, Solid State Ionics, 79 (1995)98.

Mca82 A.J. McAlister, " The Al-Li (Aluminum-Lithium) System, Bull. of Alloy Phase Diagrams, Vol. 3, No.2, (1982).

Miz92 Junichiro Mizusaki and Hiroaki Tagawa, Lithium carbonate as a solid electrolyte, Solid State Ionics, 53-56 (1992) 791-797.

Mor96 M. Morales and A.R. West, Solid State lonies, 91 (1996) 33.

Mul26 A.Muller, "The Al-Li Phase Diagram", Z. Metallkd., 18, 231-232 (1926) in Germen.

Myl76 K.M. Myles, F.C. Mrazek, J.A. Smaga and J.L. Settle, " Materials Development in the Li-Al/Fe Sulfide Battery Program at Argonne National Laboratory", Proc. Symp. and Workshop on Adv. Baattery Res. and Design, U.S. ERDA Report ANL-76-8, B50-B73, March (1976).

Nag93 G. Nagasubramanian, I.A. Attia and G. Halpert, Solid State lonics, 67 (1993) 51.

Nag94 M. Nagai and T. Nishino, Solid State lonics, 70-71 (1994) 96.

Nan98 N. Nandakumar, "THE LIQUID PHASE INFLUENCE ON MICROSTRUCTURE EVOLUTION IN THE SILICON NITRIDE-BASE/SAS SYSTEM", Master Thesis, Univisity of Houston, 1998.

Neu96 B.J. Neudecker and W. Weppner, J. Electrochem. Soc., 143 (1996) 2198.

Nic90 M.G. Nicholas, Joining of Ceramics, Chapman and hall, 1990.

Nob71 B. Noble and G. E.Thompson, Metal Sci. J., 5, 114, 1971.

Nob98 B. NOBLE and S. E. BRAY, Acta mater., Vol. 46, No. 17, pp. 6163±6171, (1998).

Oba81 H. Obayashi, A. Gotolt and R. Nagai, Mat. Res. Bull., 16 (1981) 581.

Oba81A H. Obayashi, R. Nagai, A. Gotoh, S. Mochizuki and T. Kudo, Mat. Res. Bull., 16 (1981) 587.

Ohn83 Hideo Ohno, Satoshi Konishi, Kenji Noda et. al, J. Nuclear Materials, 118, pp242-247, 1983.

Pet87 A. Petric, PhD Thesis, "development of Cation Substituted Beta Alumina Solid Electrolytes And EMF Measurements of the Thermodynamic Properties of Ionic Alloys", University of Montreal.

Pet88 A. Petric, A.D. Pelton and M-L. Saboungi, J. Phys. F: Met. Phys., 18, 1473 (1988).

Pim88 M.A. Pimenta, P. Echegut, F. Gervais and P. Abelhard, Solid State Ionies, 28-30 (1988) 224.

Qua83 C. Li-Quan, W. Lion-Zhong, C. Guang-Can, W. Gang and L. Zi-Rong, Solid State Ionics, 9-10 (1983) 149.

Qui89 P. Quintana and A.R. West, J. Solid State Chem., 81 (1989) 257.

Qui89A P. Quintana, F. Velasco and AR. West, Solid State Ionics, 34 (1989) 149.

Rab76 A. Rabenau and H. Schultz, J. Less Common Metals, 50 (1976) 155.

Rai76 I.D. Raistrick, C. Ho And R.A. Huggins, Mater. Res. Bull., 11, 953 (1976).

Rea79 J.R. Rea and D.L. Foster, Mat. Res. Bull., 14 (1979) 841.

Rit96 A.G. Ritchie, Phil. Trans, R. Soc. Lond., A 354 (1996) 1643.

Riv78 M. Rivier and A.D. Pelton, "A New Slip-Casting Technique for the Laboratory Fabrication of b-Alumina and Other Ceramics", Ceramic Bulletin, Vol. 57, No.2 (1978).

Rob92 A.D. Robertson and AR. West, Solid State Ionics, 58 (1992) 351.

Rob93 A.D. Robertson, PhD Thesis, University of Aberdeen, 1993.

Rob94 A.D. Robertson and AR. West, J. Mat. Chem., 4 (1994) 457.

Rob97 A.D. Robertsona, A.R. West and A.G. Ritchie, "Review of crystalline lithium-ion conductors suitable for high temperature battery applications", Solid State Ionics, 104 (1997) pp.1-11.

Rod85 A.R. Rodger, J. Kuwano and A.R. West, Solid State lonies, 15 (1985) 185.

Roz76 I. A. Rozdin, H. T. Saripov, S. S. Plotkin, N. V. Brotnikov, T. B. Polueva, and K. I. Petrov, Izv. Akad. Nauk SSSR Neorg. Mater., 12, 863 (1976).

Sab84 M.-L. Saboungi and T.P.Corbin, "Dilute Solutions of Sodium in Molten Bismuth and Tin: EMF Measurements and Interpretation", J. Phys F: Met. Phys., 14 13-21, 1984.

Sai90 Y. Saito, T. Asai, K. Ado, H. Kageyama and O. Nakamura, Solid State lonics, 40-41 (1990) 34.

Sai91 Y. Saito, K. Ado, T. Asai, H. Kageyama and O. Nakamura, Solid State lonics, 47 (1991) 149.

Sam82 G.V. Samsonov, The Oxide Handbook, Second Ed., (IFI Plenum Data Company, New York, 1982).

Sat96 M. Sato, Y. Kono, H. Ueda, K. Uematsu and K. Toda, Solid State lonics, 83 (1996) 249.

Sch72 H. Schmalzried and A.D.Pelton, "Two Aspects of Solid-State Thermodynamics at Elevated Temperetures: Point Defects and Solid State Galvanic Cells" Ann. Rev. Mater. Sci., 2, 143-80, 1972.

Sch86 B. Schoch, E. Hartmann and W Weppner, Solid State lonics, 18-19 (1986) 529.

Sha37 F.I. Shamray and P.Ya. Saldau, "Equilibrium Diagram of the System Al-Li", Izv. Akad. Nauk SSSR, Otdel. Khim., 631-640 (1937). in Russian.

Sha77 D. Shannon, B.E. Taylor, A.D. English and T. Berzins, Electrochim. Acta, 22 (1977) 783.

Sin76 R.N. Singh, J. Am. Ceram. Soc., 59, 112 (1976).

Smi76 J.F. Smith, Journal of Nuclear Materials, 59 (1976) 158-174.

Smi91 R.I. Smith and AR. West, J. Solid State Chem., 93 (1991) 436.

Smi91A R.I. Smith and AR. West, J. Mat. Chem., 1 (1991) 91.

Ste71 V. stewner and R.oppe, Z. Anorg. Allg. Chem., 380 (1971) 250.

Sta72 L. Staffanson, Acta Chem. Second., 26 (1972) 2150.

Sum95 H.H. Sumathipala, M.A.K.L. Dissanayake and A.R. West, J. Electrochem. Soc., 142 (1995) 2138.

Tak66 T. Takahashi and O. Yamamoto, Electrochimica Acta, 11 (1966) 779.

Tay77 B.E. Taylor, A.D. English and T. Berzins, Mat. Res. Bull., 12 (1977) 171.

Tdr96 R. Tdrneberg and A. Lun&n, Solid State lonics, 90 (1996) 209.

Tou90 M. Touboul, N. Sephor and M. Quarton, Solid State Ionics, 38 (1990) 225.

Uva92 N.F. Uvarov, Y.R. Isupov , V. Sharma and A.K. Shukla, Solid State lonics, 51 (1992) 41.

Uva94 N.F. Uvarov, B.B. Bokhanov, V.Y. Isupov and E.F. Hairetdinov, Solid State lonics, 74 (1994) 15.

Uva96 N.F. Uvarov, E.F. Hairetdinov and EV. Robelev, Solid State lonics, 86-88 (1996) 577.

Vel80 E. Veleckies, "Thermodynamic investigation of the Li-Al and Li-Pb systems by the Hydrogen Titration Method", J. Less-Common Met., 73, 49-60 (1980).

Vol69 H. Vollenke and A. Wittmain, Zeit. Krist., 128 (1969) 66.

Wag56 C. Wagner, International Committee of Electrochemical Thermodynamics and Kinetics, proc. 7th meeting (1955), Butterworths, London (1956).

Wag89 L.B. Wagner Jr., in T. Takahashi (Ed.), High Conductivity Solid Ionic Conductors, World Scientific Pub. Co., Singapore, 1989.

Wai67 A.Waintal and M. Gondrand, Mater. Res. Bull., 2, 9 (1967) 889.

Wak88 M. Wakaihara, T. Uchida and T. Gohara, Solid State lonies, 31 (1988) 17.

Wan98 Y. Wang , J. Sakamoto , C.K. Huang , S. Surampudi , S.G. Greenbaum, "Lithium-7 NMR investigation of electrochemical reaction of lithium with SnO", Solid State Ionics, 110 (1998) 167–172.

Wen79 C.J. Wen, B.A. Boukamp, R.A. Huggins and W. Weppner, "Thermodynamic and Mass Transport Properties of LiAl", J. Electrochem. Soc., 126, 2258-2266 (1979).

Wen80 C.J. Wen, W. Weppner, B.A. Boukamp and R.A. Huggins, "Electrochemical Investigation of Solubility and Chemical Diffusion of Li in Al", Met Trans., 11B, 131-137 (1980).

Wes70 A.R. West and F.P. Glasser, J. Mat. Sci., 5 (1970) 557.

Wes73 A.R. West, J. App. Electrochem., 3 (1973) 327.

Wes89 A.R. West, Ber. Bunsenges Phys. Chem., 93 (1989) 1235.

Whi71 M.S.Whittingham and R.A. Huggins, J. Phys. Chem., 54 (1971)

Wil75 D.B. Williams and J.W. Edington, "The precipitation of d' (Al3Li) in dilute Al-Li Alloys", Met. Sci., 9, 529-532 (1975).

Wil89 D.B. Williams, in Aluminum-Lithium Alloys V, ed. T.H. Saunders Jr and E. A. Starke Jr. AIME, Warrendale, PA, 1989.

Yam00 Luis Yamarte, Master Thesis, McMaster University, 2000.

Yam87 H. Yamane, S. Kikkawa, M. Koizumi, Solid State Ionics, 25 (1987) 183.

Yam96 J. Yamaki, H. Ohtsuka and T. Shodai, Solid State Ionics, 86-88 (1996) 1279.

Yao71 N.P. Yao, L.A. Heredy and R.C. Saunders, "EMF Measurements of Electrochemically Prepared Li-Al Alloy", J. Electrochem. Soc., 118, 1039-1042 (1971).

Yat74 S.P. Yatsenko and E.A. Saltykova, "Thermodynamic Properties of Liquid Li-Al Alloys", Russ.J. Phys. Chem., 48, 1402-1403 (1974).

Zha93 X.Zhang, D. Jefferson and R.Lambert, Journal of Catalysis, 141 (1993) 583-594.

Zou93 Y. Zou and A. Petric, Mat. Res. Bull., 28 (1993) 1169.

Zou93A Y. Zou and A. Petric, J. Electrochem. Soc., 140 (1993) 1388.

Zou94 Y. Zou and A. Petric, J. Phys. Chem. Solids, 55,6 (1994) 493-499.